Imperial College London

Department of Mechanical Engineering

Ultrasonic grain noise and defect monitoring in large grained materials

Yuan Liu

September 2018

A thesis submitted for the degree of

Doctor of Philosophy

Declaration

I herewith certify that all material in this dissertation which is not my own work has been properly acknowledged.

Yuan Liu

Copyright Declaration

The copyright of this thesis rests with the author and is made available under a Creative Commons Attribution Non-Commercial No Derivatives licence. Researchers are free to copy, distribute or transmit the thesis on the condition that they attribute it, that they do not use it for commercial purposes and that they do not alter, transform or build upon it. For any reuse or redistribution, researchers must make clear to others the licence terms of this work.

Abstract

In the next generation of power stations, high temperatures (up to 700 °C) will be used to improve efficiency. As creep deformation is of great concern at such high temperatures, materials with large grains are desirable due to their high creep strength. However, this brings a challenge in ultrasonic monitoring of the plants, because when the grain size is comparable with the wavelength, scattering caused by the acoustic impedance contrast on the grain boundaries can strongly attenuate the signals from defects and significantly increase the noise, which often results in low signal to noise ratios (SNRs) and makes the defect detection difficult.

In this thesis, the potential of two techniques to overcome the low SNR problem, baseline subtraction with repeat scanning and optimising the transducer and placement for monitoring with permanently installed sensors, is investigated. In order to find the optimal permanently installed monitoring system, it is desirable to understand the noise behaviour in highly scattering regimes, which cannot be fully described with existing theoretical models. Therefore, 3D FE modelling, which can achieve it, is proposed as an alternative approach for noise prediction.

In Chapter 2, the feasibility and reliability of comparing repeat tests using baseline subtraction to reduce grain noise is studied. The feasibility of setting the transducer with the same angle and stand-off relative to the testpiece, registering the C-scans to locate the same position and using compensation methods to compensate for the temperature and transducer frequency response changes in repeat scans is investigated experimentally. Results show that modest improvement in SNR can be obtained when the temperature and transducer frequency response changes are relatively small, and the dominant factors restricting the improvement are the temperature and transducer frequency response

changes.

In Chapter 3, 3D FE modelling is proposed to study the backscattering noise behaviour. Firstly, the 3D FE approach is validated by comparing the FE predicted longitudinal-to-longitudinal backscattering amplitude from a single grain with the theoretical solution given by the established theories. Then noise levels are predicted by the FE approach and compared with the theoretical predictions, which are obtained following a similar way to that used to develop the Independent Scatterer Model. From the comparison, it can be seen that the theoretical model can give a rough estimation of the grain noise level very efficiently. Therefore, considering the high computational costs of FE simulations, the theoretical model should be used to give a first estimate of grain noise level, and the FE approach can be used to provide a more accurate prediction where required.

In Chapter 4, a procedure of how to find the optimal transducer parameters and placement in a permanently installed monitoring system is presented. A combined analytical-and-numerical method is adopted to generate a SNR map and the influence of various parameters of the transducer, excitation and material on SNR is discussed. Then representative examples are presented to show how to solve the optimisation problem under different possible criteria.

Acknowledgements

I would like to express my sincere gratitude to my supervisor Professor Peter Cawley for his patient guidance, support and encouragement throughout the course of my research. I would also like to thank Professor Peter Nagy for his valuable suggestions, assistance and early morning skype meetings.

My heartfelt thanks go to Dr. Anton Van Pamel, who helped me a lot during my study, especially when I just started my research work, teaching me how to do immersion tests, introducing me to the scattering theory and always ready to offer helpful suggestions. I also appreciate the help of Dr. Chang Liu on the methodology and programming of data processing, especially for his help in finishing Section 2.4.2 in this thesis.

Furthermore, my thanks also go to all the members of the Non-Destructive Evaluation group, especially Professor Michael Lowe, Dr. Fred Cegla, Dr. Peter Huthwaite, for their dedication to the group, and Dr. Bo Lan, Dr. Stewart Haslinger, Dr. Fan Shi, Dr. Xiaoyu Xi, Dr. Konstantinos Zarogoulidis, Dr. Chao Zhang, Dr. Fangxin Zou, Sebastian Heinlein, Sebastian Eckel, Andreas Zimmermann, Xiaotang Gu and Ming Huang for their friendship. The friendly and collaborative working environment of the group made every day of my PhD study really enjoyable.

I appreciate the Chinese Scholarship Council for funding my PhD study, Engineering and Physical Sciences Research Council for funding this project and AMEC Foster Wheeler for providing the sample used in the experiments presented in Chapter 2.

Last but not least, I would like to thank my parents and husband for their unyielding support and encouragement.

Contents

1 Introduction **1**

1.1 Motivation 1

1.2 Grain boundary scattering of ultrasound waves 2

1.3 Aims and objectives 4

1.4 Thesis outline 7

2 Feasibility and reliability of grain noise suppression in monitoring of highly scattering materials **9**

2.1 Introduction 9

2.2 Experimental setup 11

2.3 Repeatability test 13

2.3.1 Transducer angle 13

2.3.2 Transducer stand-off 17

2.3.3 Test position 18

2.4 Compensation 21

2.4.1 Temperature compensation 21

2.4.2 Compensation for transducer frequency response change 27

2.4.3 Overall influence of different factors 36

2.5 Summary of the chapter 37

3 A finite element model for ultrasonic backscattering of polycrystalline materials **39**

3.1 Introduction 39

3.2 Measurement and validation of backscattering amplitude 40
3.2.1 Spherical inclusion 43
3.2.2 Irregular shaped inclusion 45
3.2.3 RMS backscattering amplitude of single random shaped inclusions . 46
3.3 Prediction of grain noise measured with plane wave excitation and point receivers 49
3.4 Prediction of grain noise measured with a finite transducer 59
3.5 Summary of the chapter 65

4 Optimal permanently installed monitoring system for polycrystalline materials 68

4.1 Introduction 68
4.2 SNR map generation 70
4.2.1 Signal reflection prediction 70
4.2.2 Particle velocity field and Gaussian beam fitting 72
4.2.3 Scattering induced attenuation 73
4.2.4 Grain noise calculation and SNR map generation 75
4.3 Influence factors of SNR 76
4.3.1 Effects of excitation parameters 77
4.3.2 Effects of grain size 77
4.3.3 Effect of defect size 79
4.3.4 Effects of anisotropy factor 80
4.3.5 Effects of transducer parameters 82
4.3.6 Summary 84
4.4 Case studies 85
4.4.1 Example 1 88
4.4.2 Example 2 90

4.5 Summary of the chapter 92

5 Conclusions **94**

5.1 Thesis review 94

5.2 Suggestions for future work 97

List of Tables

2.1 Transducers used; all were unfocused 13

2.2 The improvement achieved by calibrating and/or compensating for various factors in baseline subtraction 36

3.1 Elastic constants and anisotropy factors of the cubic materials discussed in this section 56

4.1 Model and mesh sizes used for defect reflection prediction at different frequencies 71

4.2 Model and mesh sizes used for velocity field prediction at different frequencies 73

4.3 Elastic constants for the fictitious cubic materials 81

4.4 Summary of how $d_{\text{min\_D}}$, $d_{\text{max\_D}}$ and θ change with various factors 85

List of Figures

2.1 Definition of degrees of freedom in the tests. 10

2.2 Schematic drawing (not to scale) of potential errors due to transducer setup in repeat inspections (a) different transducer angle (b) different transducer stand-off (c) different test point. 10

2.3 Experimental setup of the immersion tests conducted in this chapter. . . . 12

2.4 Typical A-scan signals obtained with Transducer 1 (a) frontwall (b) whole signal with clipped frontwall. Both signals are shifted to make the frontwall peak at time zero. 13

2.5 Schematic diagram of transducer alignment method. 14

2.6 Noise to frontwall amplitude ratio versus distance from sample surface before and after baseline subtraction. The data consists of eight A-scans where the first represents the baseline and the seven successive traces are used for subtraction. Each data point shows the mean (line) and standard deviation (bar) of the RMS for a 14 mm window centred about its indicated $x-$axis value. The range of depths considered here corresponds to the grain noise which lies in-between the frontwall and backwall signals. Electrical noise residual is around 94 dB below the frontwall signal. 15

2.7 Mean noise reduction over sample depth after baseline subtraction as a function of transducer stand-off difference. Error bars show the standard deviation of ten repeats at each stand-off. 18

2.8 Overlapped C-scan images (backwall echo amplitude) from repeat tests (a) before and (b) after alignment. 19

2.9 Noise to frontwall amplitude ratio versus distance from sample surface before and after baseline subtraction. The data consists of ten A-scans from the first C-scan representing the baselines and the other ten traces from the second C-scan used for subtraction. Each data point shows the mean (line) and standard deviation (bar) of the RMS for a 14 mm window centred about its indicated $x-$axis value. The range of depths considered here corresponds to the grain noise which lies in-between the frontwall and backwall signals. Electrical noise residual is around 84 dB below the frontwall signal. 20

2.10 Noise to frontwall amplitude ratio versus distance from sample surface before subtraction and after subtraction with and without temperature compensation. Each data point shows the RMS for a 14 mm window centred about its indicated $x-$axis value. The range of depths considered here corresponds to the grain noise which lies in-between the frontwall and backwall signals. The temperatures of the baseline and current signals are 23 °C and 33 °C respectively. Electrical noise residual is around 98 dB below the frontwall signal. 25

2.11 Mean noise reduction after subtraction with and without temperature compensation at different temperatures. The temperature of the baseline signal is 23 °C. 26

2.12 Typical A-scans showing the frontwall reflection. Plots (a-d) and (e-h) represent the time and frequency domain signals collected with different excitations, whose peak frequencies are respectively 6.5, 6.75, 7.0 and 7.25 MHz. Blue and red represent signals obtained from two different transducers. 30

2.13 Typical A-scans showing the grain noise signals in between frontwall and backwall reflections. Plots (a-d) and (e-h) represent the time and frequency domain signals collected with different excitation, whose peak frequencies are respectively 6.5, 6.75, 7.0 and 7.25 MHz. Blue and red represent signals obtained from two different transducers. 31

2.14 Correlation coefficients before (a-c) and after (d-f) frequency compensation at 41×16 locations with an area of 20×7.5 mm^2 on the sample. Compensation is conducted using signals with peak frequency of 7.00 MHz as the baselines. (a, d), (b, e) and (c, f) correspond to the results using signals with peak frequencies of, respectively, 6.50, 6.75 and 7.25 MHz. 32

2.15 Mean noise reduction across the scan area from compensation and subtraction compared to the original baseline inspection. (a) Current and baseline signals were measured from the same transducer. (b) Current and baseline signals were measured from different transducers. Horizontal and vertical axes indicate the peak frequencies of the excitation used in, respectively, current and baseline signals. 34

3.1 "Single-grain" model ($10\times10\times35$ mm^3): an inclusion located at the central axis along the excitation direction in an isotropic host material is subject to a plane wave excitation. A point receiver used to capture the first backscattered longitudinal reflection from the inclusion is located on the central axis. 42

3.2 Comparison of FE and theoretical backscattering amplitudes of a spherical inclusion with (a) an isotropic material and (b) a cubic material with a Zener anisotropy factor ($A_z = 2C_{44}/(C_{11} - C_{12})$ [1]) of 1.4. One hundred random orientations for the cubic material are considered. The RMS of the 100 FE results are plotted as red dots in (b) and the error bars show their standard deviation. 44

3.3 The irregular shaped inclusion modelled with uniform hexahedral elements with an edge length of 0.05 mm. 45

3.4 Comparison of FE and theoretical backscattering amplitudes of an irregular inclusion with (a) an isotropic material and (b) a cubic material with a Zener anisotropy factor of 1.4. One hundred random orientations for the cubic material are considered. The RMS of the 100 FE results are plotted as red dots in (b) and the error bars show their standard deviation. Two centre frequencies, 2 MHz and 4 MHz, are used in the FE simulations for the inclusion with cubic symmetry. 47

3.5 Comparison of FE and theoretical RMS backscattering amplitudes of single random shaped grains with a cubic material whose Zener anisotropy factor is 1.4. Five hundred random grains with random orientations for the cubic material are considered as the inclusion at the central axis in the "single-grain" model. The RMS of the 500 FE results are plotted as red dots and the error bars show their standard deviation. Two centre frequencies, 3 MHz and 6 MHz, are used in the FE simulations. 48

3.6 A schematic of a 2D section of the 3D theoretical model used for grain noise prediction with the plane wave configuration 49

3.7 Multi-grain model ($13 \times 13 \times 50$ mm^3) with plane wave excitation. Point transmitters/receivers are uniformly distributed on the transmitting and receiving plane. 54

3.8 Spatial RMS of signals received by all the point receivers. The centre frequency of the excitation is 3 MHz. Three anisotropy factors, 1.4, 2.2 and 3.0, are discussed here. The frontwalls and backwalls are clipped where needed to highlight the grain noise. 55

3.9 Comparison of FE, theoretical noise RMS and sevenfold theoretical noise RMS. The points on the dashed lines are the RMS noise (as shown in Figure 3.8) within a rectangular time window between 5 μs to 8 μs at different centre frequencies. 56

3.10 A schematic showing how a shear wave contributes to a signal received at a point receiver. 57

3.11 Noise RMS vs edge length of the square coherent averaging area (expressed in shear wavelengths and denoted by m). Each point on the blue curve is obtained in a similar way as that used to plot Figure 3.9, except that the spatial RMS is taken over the signals obtained by coherently averaging the signals on areas with dimensions of $m \times m$ wavelength square across the receiving plane. The red line is proportional to $1/m$. 58

3.12 "Multi-grain" model ($13\times13\times20$ mm^3). A 5 mm radius focused transducer is outlined by the white circle. Focusing is achieved through adding time delays to the excitation and reception of individual nodes. A Hann-window is applied on the excitation amplitude over the plane of the transducer to remove surface waves. 62

3.13 Comparison of FE and theoretical grain noise with anisotropy factors of (a) 1.4, (b) 2.2 and (c) 3.0. Attenuation of noise is not taken into account in the theoretical theory. 63

3.14 Comparison of theoretical grain noise with and without coherent attenuation and FE results. The anisotropy factors are (a) 1.4, (b) 2.2 and (c) 3.0 respectively. 64

4.1 A schematic of a 3D isotropic model with an on-axis flat-bottom hole used for defect reflection prediction 71
4.2 A schematic of an ABAQUS 2D axisymmetric model with uniformly distributed point receivers used to predict velocity field 73
4.3 A schematic of the 3D grained model used for attenuation prediction . . . 74
4.4 Typical FOM against half of grain size curves, plotted using Equation 4.2 at frequencies 1 MHz, 2 MHz and 5 MHz. ρ = 8000 kg/m^3, C_{11} = 246.8 GPa, C_{12} = 144.0 GPa, C_{44} = 102.9 GPa. 78
4.5 A schematic of a SNR map. θ represents the divergence angle of a −6 dB decrease in the echo field of the SNR. $d_{\text{min\_D}}$ and $d_{\text{max\_D}}$ are the minimum and maximum depths of a cylinder with the same diameter as the transducer, in which $\Delta\text{SNR}_\text{x}$ ≤6 dB and SNR≥10 dB. It is also required that the cylinder is beyond the dead zone. 79
4.6 SNR maps (in dB) with defect diameters of (a) 1, (b) 2 and (c) 5 mm. θ represents the divergence angle of a −6 dB decrease in the SNR echo field. $d_{\text{min\_D}}$ and $d_{\text{max\_D}}$ are the minimum and maximum depths of a cylinder with the same diameter as the transducer, in which $\Delta\text{SNR}_\text{x}$ ≤6 dB (in between the green lines) and SNR≥10 dB (inside the black curve). 81
4.7 SNR maps (in dB) with anisotropy factors of (a) 1.2, (b) 2.0 and (c) 2.8. θ represents the divergence angle of a −6 dB decrease in the SNR echo field. $d_{\text{min\_D}}$ and $d_{\text{max\_D}}$ are the minimum and maximum depths of a cylinder with the same diameter as the transducer, in which $\Delta\text{SNR}_\text{x}$ ≤6 dB (in between the green lines) and SNR≥10 dB (inside the black curve). 82
4.8 FOM versus anisotropy factor at frequencies 1, 2, 5 and 10 MHz obtained using Equation 4.2. Each point shows the FOM calculated with the elastic constants which are obtained with the corresponding anisotropy factor. . . 83

4.9 SNR maps (in dB) with transducer frequencies of (a) 1.4, (b) 1.8 and (c) 2.2 MHz with a constant $\frac{D}{\lambda}$. The attenuation term is applied in the signal computation but not in the noise calculation. θ represents the divergence angle of a −6 dB decrease in the SNR echo field. $d_{\text{min\_D}}$ and $d_{\text{max\_D}}$ are the minimum and maximum depths of a cylinder with the same diameter as the transducer, in which $\Delta\text{SNR}_{\text{x}} \leq 6$ dB (in between the green lines) and SNR≥10 dB (inside the black curve). 84

4.10 SNR maps (in dB) with transducer frequencies of (a) 1.4, (b) 1.8 and (c) 2.2 MHz with a constant $\frac{D}{\lambda}$. No attenuation term considered in the calculation. θ represents the divergence angle of a −6 dB decrease in the SNR echo field. $d_{\text{min\_D}}$ and $d_{\text{max\_D}}$ are the minimum and maximum depths of a cylinder with the same diameter as the transducer, in which $\Delta\text{SNR}_{\text{x}} \leq 6$ dB (in between the green lines) and SNR≥10 dB (inside the black curve). . 85

4.11 SNR maps (in dB) with transducer diameters of (a) 3.4, (b) 6.7 and (c) 10 mm. With a constant frequency of 1.8 MHz, the transducer diameter to wavelength ratios are 1, 1.5 and 2 respectively. θ represents the divergence angle of a −6 dB decrease in the SNR echo field. $d_{\text{min\_D}}$ and $d_{\text{max\_D}}$ are the minimum and maximum depths of a cylinder with the same diameter as the transducer, in which $\Delta\text{SNR}_{\text{x}} \leq 6$ dB (in between the green lines) and SNR≥10 dB (inside the black curve). 86

4.12 Schematics of SNR maps under Criteria (a) 1 and (b) 2. $\boldsymbol{D}$ and $\boldsymbol{D}_c$ show the diameters of the transducer and inspection cylinder respectively. d_{min} and d_{max} are the minimum and maximum depths of interest. $d_{\text{max\_D}}$ is the maximum depth that can be covered by an inspection cylinder with a diameter of $\boldsymbol{D}$, in which $\Delta\text{SNR}_{\text{x}} \leq 6$ dB (in between the green lines) and SNR≥10 dB (inside the black curve). 88

4.13 Maximum depths of the inspection cylinders at different $f - D$ combinations. D and $D_{\min}$ are the transducer diameter and its minimum requirement. D_c here shows the maximum inspection cylinder diameter determined by the requirements. The inequalities show the reasons for the blank areas. The $y-$axis scale increases downwards. 90
4.14 Weld monitoring geometry; T/R means transmitter/receiver. 90
4.15 Fractional surface areas covered with transducers ($\frac{D^2}{{D_c}^2}$) at different $f - D$ combinations. D and D_c show the diameters of the transducer and inspection cylinder respectively. $d_{\max}$ is the maximum depth of interest. $d_{\max\_D}$ is the maximum depth that can be covered by an inspection cylinder with a diameter of D. $D_{\min}$ is the minimum requirement of the transducer diameter. The inequalities show the reasons for the blank areas. The $y-$axis scale increases downwards. 91

Chapter 1 Introduction

1.1 Motivation

In the next generation of power stations, high temperatures (up to 700 °C) will be used to improve efficiency [2]. For components working at such high temperatures, creep deformation is of great concern, as it can weaken structures and finally cause creep failure. Grain boundary sliding is one of the mechanisms that contribute to creep in metals [3, 4], so the creep rate is related to the grain boundary area [5]. Therefore, large grained materials are desirable to be used in power plants as they can provide high creep strength.

During the service life of the power plants, under the high temperatures, creep and fatigue are two main damage mechanisms [6, 7]. Defects introduced by the two mechanisms could cause catastrophic failure if they grow beyond a critical size. Therefore, to guarantee the normal operation and prolong the service life of the plants, their structural health needs to be monitored using Non-Destructive Evaluation (NDE). Visual inspection [8], liquid penetrant testing [9] and magnetic particle inspection [10], are commonly used NDE methods to detect surface breaking defects. For defects under the surface, more advanced NDE techniques are required, such as radiography [11, 12] and ultrasound testing [13, 14]. Radiography uses electromagnetic waves with a short wavelength and high energy for defect detection, which can pose a hazard to human health, so it requires costly measures to clear areas when it is applied in-situ [15]. In addition, it is insensitive to defects whose plane is normal to the radiation direction and the potential increase of the component thickness needs increased penetration which may require radiation at infeasible levels [16]. Therefore, ultrasound, which uses mechanical waves for inspection, is more desirable for the structural health monitoring of the plants [16].

1.2 Grain boundary scattering of ultrasound waves

Ultrasound locates and characterises defects in a material by the scattering of waves from the defects, which is shown as echoes in the received signals. Similarly, the ultrasound waves can also be scattered from the grain/colony boundaries in polycrystalline materials, due to the acoustic impedance contrast caused by different alignments of principal axes of the grains/colonies [17]. The grain boundary scattering causes two phenomena: attenuation of the coherent waves and microstructural noise. Good understanding of the two phenomena is important for NDE inspection and material characterisation of polycrystalline materials.

Studies on the first phenomenon, the scattering induced attenuation, have been carried out since the three attenuation regimes – Rayleigh [18], geometric [19, 20] and stochastic regimes [21] – were established. These experimental discoveries found that the attenuation is related to the grain size of a material. Early research based on two major assumptions – spherical grains and single scattering – obtained the theoretical form of this relationship for cubic materials [22], hexagonal materials [23] and orthorhombic materials [24, 25]. Efforts were made to get more general solutions by amending the assumptions [26–28], but the reliance on the two assumptions did not entirely end until the Unified Theory [29] was proposed. The Unified Theory relies on a second-order Keller approximation [30] and a geometric autocorrelation function is used for the grain distribution description. This theory shows a good validation against experimental results [31, 32] and remains widely accepted now. In recent years, the attenuation of polycrystalline materials is still an active topic. Various approaches, e.g. [33], and extensions to more complicated microstructures [34–37] have been investigated. In addition to the theoretical models, the finite element (FE) method has been proposed as an approach for the study of attenuation [38, 39]. With a highly efficient GPU based solver POGO [40], 3D FE models multiple wavelengths long in each dimension have been used to predict ultrasonic wave propagation in polycrystalline

materials [41, 42], where the validity of FE in predicting attenuation in different regimes has been validated.

Backscattered ultrasonic grain noise, another phenomenon caused by the scattering, has also attracted much interest in the past decades. The Independent Scatterer Model (ISM), which predicts absolute noise levels, was developed and validated with experiments [43, 44]. This model accounts for system effects by adopting Thompson and Gray's model [45] and for the material by a characteristic material parameter, termed the figure of merit (FOM). The FOM is identical to the square root of the backscattering coefficient used in [46–48], which relates the backscattered ultrasonic noise to the microstructure and has been experimentally validated [49]. More recently, another theoretical model of single scattering response in polycrystalline materials for longitudinal-to-longitudinal (L-L) scattering was presented [50], being able to capture the overall behaviour observed in [43]. The model was then extended to include ultrasonic wave propagation through a fluid-solid interface and experimentally validated [51]. Following a similar formalism, models describing longitudinal-to-transverse scattering [52] and transverse-to-transverse scattering [53] have been developed. Based on these models, research has been carried out to study materials with more complicated microstructures [54–56].

Most of the noise models established in these studies are based on a single scattering assumption, which assumes the reflection from one grain is not affected by other grains. This assumption limits the validity of the models to weakly scattering regimes, because the interaction between grains is not negligible if the scattering is high [57]. To estimate the range of the validity, based on a multiple scattering framework [50], a noise model which accounts for double scattering has been developed and the contribution of double scattering has been discussed in [58], the results of which allow the uncertainty of the single scattering approximation to be determined and show the potential of solving highly scattering problems. However, significant difficulties remain to develop a theoretical ultrasonic backscattering model which includes the full multiple scattering events. Apart

from the theoretical methods, FE modelling is an alternative approach to study the noise behaviour. Unlike the theoretical models, the FE modelling is capable of solving the full-physics scattering problem including multiple scattering, which makes it a promising tool to give an accurate prediction of grain noise in both weakly and highly scattering regimes. Until recently, computational costs have limited FE simulations to 2D [59, 60]. Even though it has shown that some representative features of the 3D ultrasonic scattering can be captured by the 2D model, 3D simulation remains necessary to investigate the grain noise behaviour due to the inherent 3D nature of the physical phenomenon.

The establishment of the theoretical relationship between the microstructure and attenuation coefficient/grain noise enables the microstructural properties of the material to be evaluated using the attenuation and noise, which is also an attractive topic in recent years. Grain size has been evaluated using ultrasonic attenuation measurements [61, 62], corrected ultrasonic attenuation model which accounts for diffraction [63] and for diffraction and interface losses [64], multi-scale attenuation coefficient [65] and ultrasonic backscattering data [62, 66]. In addition to grain size, attenuation analysis has also been used to characterise porosity levels in ceramic products [67] and microstructure evolution during thermomechanical processing [68]. However, unlike material characterisation, which benefits from the valuable information provided by the scattering, ultrasound health monitoring of large grained materials is made difficult by the scattering, which will be discussed below.

1.3 Aims and objectives

When a large grained material is to be inspected, as the grain size is comparable with the wavelength, typically of the millimetre scale, grain boundary scattering becomes significant. In this case, the attenuation can strongly reduce the amplitude of reflections received from defects and the scattering can significantly increase the noise level, so that

the resulting signal to noise ratio (SNR) is often too low for the test to be viable, which makes the ultrasonic monitoring of plants made of large grained materials challenging.

As the grain noise is temporally coherent and dependent on the excitation intensity, neither repeating a measurement and averaging the received signals nor increasing the excitation intensity can effectively enhance the SNR. Therefore, more advanced techniques are needed to overcome the low SNR problem. Two main approaches have been proposed to achieve that: one is using signal processing methods, such as split spectrum processing [69–71] and wavelet transform methods [72–74], to improve the SNR of the received signal, and another one is adopting an appropriate inspection technique to get a raw signal with a good SNR, such as the multizone technique [75–77], which uses multiple transducers focusing at different depths to scan a sample to improve SNR throughout the sample. However, the signal processing techniques which aim at improving the SNR in a raw signal show limited improvement [78], and the multizone technique cannot be used if the sensors are permanently installed on the structure to be monitored, so there are still limitations.

In this thesis, we will investigate the potential of other two techniques to overcome the low SNR problem. One is a signal processing procedure based on baseline subtraction, which has been widely researched in guided wave monitoring [79–81]. This technique suppresses the grain noise by subtracting the received signal from a reference signal. The reference signal is usually obtained at the beginning of the monitoring when it is assumed that there is no defect so only structural information, including the grain noise, is contained in the signal. The residual after subtraction then contains less grain noise and gives a higher SNR than the original signal. Optimising the transducers used in the monitoring system is another potential approach to improve the SNR, as the SNR is dependent on the frequency and diameter of the transducer due to the different dependence of the defect reflection and noise on them.

Generally, there are two means to conduct structural health monitoring, repeat scanning

and permanently installed monitoring. The potential approaches described above can both be used to enhance the SNR with each monitoring approach. However, there are some differences between the two approaches which need to be considered when we determine a strategy for the SNR improvement.

1. When the baseline subtraction is adopted: 1) repeat scanning requires the scans to be precisely registered so that the signals from the same point can be compared, so methods for lining up the two scans need to be found; 2) permanently installed monitoring requires the transducer to survive operation temperatures (up to 700 °C) without changing signal, or changing in a way that can be compensated by an appropriate signal processing technique, while repeat scanning can be conducted at shutdowns so is free of this problem.

2. When determining an optimal transducer in a permanently installed monitoring system, the cost of the monitoring system needs to be considered, while in repeat scanning, it is not a big concern as many fewer transducers are needed. In order to control the cost, the requirement of SNR needs to be sacrificed. Therefore, instead of the maximum SNR, the maximum inspection area/depth from a single transducer position is often set as a target of the optimisation problem where a minimum acceptable SNR in the monitored volume is often set as a requirement.

In this thesis, we will first investigate the feasibility of using the baseline subtraction method to suppress the grain noise in repeat scanning in Chapter 2 and then in Chapter 4 propose a procedure to optimise the transducer used in a permanently installed monitoring system where we assume that the transducer can survive the high temperature. As reviewed in the last section, there is still a lack of an accurate description of the noise behaviour for 3D highly scattering problems. However, in order to solve the optimisation problem of the permanently installed monitoring system, it is desirable that we can predict the grain noise for both weakly and highly scattering problems. Therefore, a 3D FE

approach which can achieve it will be proposed in Chapter 3.

1.4 Thesis outline

This thesis will follow the outline listed below.

In Chapter 2, the feasibility and reliability of comparing repeat tests using baseline subtraction to suppress grain noise is studied. The feasibility of setting the transducer with the same stand-off and angle relative to the testpiece and registering the C-scans to compare the same location within the different scans is investigated. An existing temperature compensation method is adopted to compensate for the temperature change between tests and a frequency compensation method is developed to compensate for the transducer frequency response change. Their effectiveness was tested experimentally. Dr. Chang Liu contributed significantly to section 2.4.2. His work is identified in the chapter and is included as it contributes to the overall conclusions and was part of the publication [82].

Chapter 3 presents an alternative approach, the 3D FE method, to study the ultrasonic backscattering of polycrystalline materials. The validation of the 3D FE approach is conducted by comparing the FE predicted longitudinal-to-longitudinal backscattering amplitude with the theoretical solution given by the established theories. Then, the RMS noise levels of two transmit-receive configurations, one with a plane wave excitation and incoherent average of the received signals and another one with a pulse-echo configuration with a finite transducer, are compared with the theoretical solutions developed in a similar way to the derivation of the ISM in [83]. During the comparison, the contribution of shear waves and multiple scattering, and the effect of the coherent attenuation on the grain noise are discussed.

Chapter 4 proposes a procedure of finding the optimal transducer parameters and placement in a permanently installed monitoring system. A combined analytical-and-numerical

method is introduced to generate a SNR map. The influence of various factors, including excitation type and duration, grain size and anisotropy factor, defect size, transducer frequency and diameter on SNR is investigated. Then, two representative example optimisation problems, under two possible criteria respectively, are discussed to show how to implement the procedure. The conclusions and contributions of the thesis are summarised in Chapter 5.

Since each of the three main chapters considers rather different subjects, the relevant literature is reviewed in the chapter rather than at the beginning of the thesis.

Chapter 2 Feasibility and reliability of grain noise suppression in monitoring of highly scattering materials

2.1 Introduction

As mentioned in Chapter 1, ultrasound inspection of large grained materials is made difficult by the scattering from grain or colony boundaries, as it can strongly attenuate reflections from defects and generate significant noise, resulting in low SNRs. Therefore, how to enhance the SNR in the testing of highly scattering materials has attracted considerable interest. Signal processing techniques provide an approach to enhance the SNR in received signals. Most of the techniques, for example, the split spectrum processing [69–71] and wavelet transform de-noising methods [72–74], aim to suppress the grain noise in raw signals but show limited improvement [78]. If we assume that the ultrasonic properties of the grains are unaffected by ageing [84], grain noise is coherent and an opportunity then exists to use a structural health monitoring (SHM) approach in which a baseline reading is subtracted from the current reading, thus removing the grain noise and producing a residual signal which reveals the presence of defects. This idea has been researched extensively in guided wave health monitoring [79–81]; this chapter assesses the feasibility of applying the idea to the bulk wave ultrasonic testing of materials that generate substantial grain noise.

Figure 2.1 defines the degrees of freedom in the tests. θ_{x} and θ_{y} are the transducer angles in $y-z$ and $x-z$ planes; z represents the stand-off of the transducer; x and y show

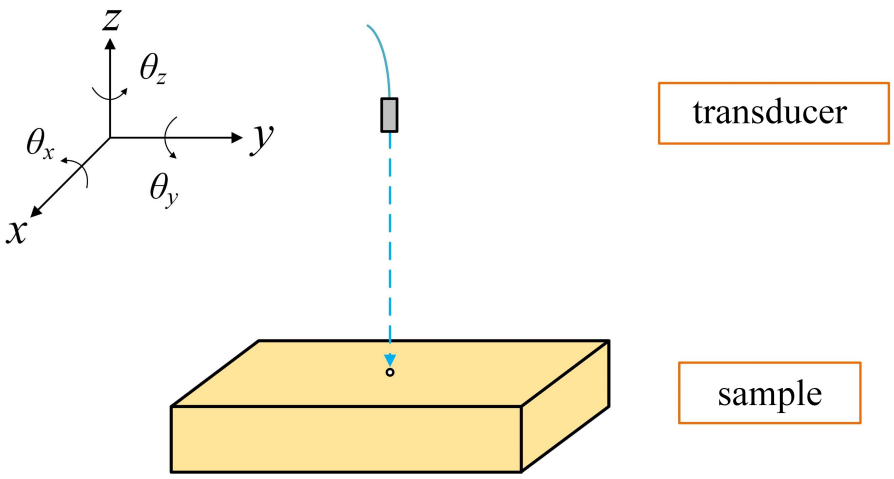


Figure 2.1: Definition of degrees of freedom in the tests.

the test position in $x-y$ plane. Here θ_z showing rotation of the transducer in $x-y$ plane is not taken into consideration, because the transducer is axisymmetric. Figure 2.2 shows the situations if the relative positions of the transducer and sample are different in two tests, which will cause differences in grain noise and so reduce the effectiveness of baseline subtraction.

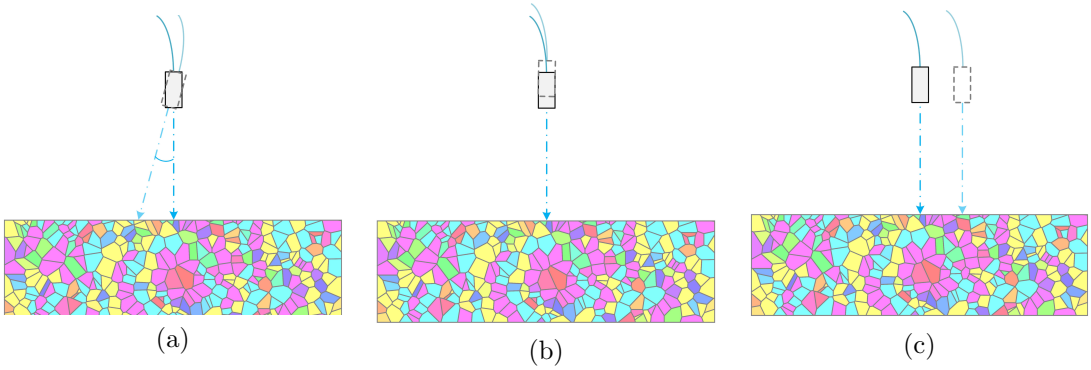


Figure 2.2: Schematic drawing (not to scale) of potential errors due to transducer setup in repeat inspections (a) different transducer angle (b) different transducer stand-off (c) different test point.

In addition to the positional errors, another challenge is that the repeat scans may be carried out at different temperatures and with different transducers of similar but non-identical specifications. A temperature change results in a difference in wave speed, and a transducer frequency response change alters the excitation waveform. Both of these

changes influence the received signals. Thus, without compensating for these effects, raw subtraction of two signals obtained in different situations can be ineffective in enhancing the SNR or even make it worse. In this chapter, a shift and scale-transform-based stretch [85] combined method is used for temperature compensation and a frequency compensation method based on frontwall reflection spectra is developed to compensate for the transducer frequency response change.

In this chapter, the feasibility and reliability of grain noise suppression in monitoring highly scattering materials using repeat scanning is studied and the success in compensating for the different test setup and environmental issues is compared. The following Section 2.2 introduces the experimental setup. Section 2.3 shows the reliability of locating the same position and hence generating the same grain noise in repeat scans. An existing temperature compensation method and a developed compensation method for transducer frequency response change are presented in Section 2.4. Finally, conclusions are given in Section 2.5.

2.2 Experimental setup

The experimental setup of the immersion tests conducted in this chapter is introduced here, and is shown in Figure 2.3. A sample of 304 stainless steel with a thickness of 40 mm was used in all the tests. It was cut from a material testing specimen supplied by a collaborating company. The sample was placed on three support feet, as commonly used in C-scan water tanks, and the transducer orientation about the x and y axes (θ_{x} and θ_{y} in Figure 2.1) was adjusted using calibrated controls on the transducer holder.

An Olympus 5077PR square wave pulser/receiver was used to send and receive the signals. In single point tests the signal was captured by a LeCroy WaveRunner 44Xi oscilloscope that has an averaging facility. The C-scans were carried out using a scanning system with an Agilent DP1400 acquisition card. The properties of the transducers used

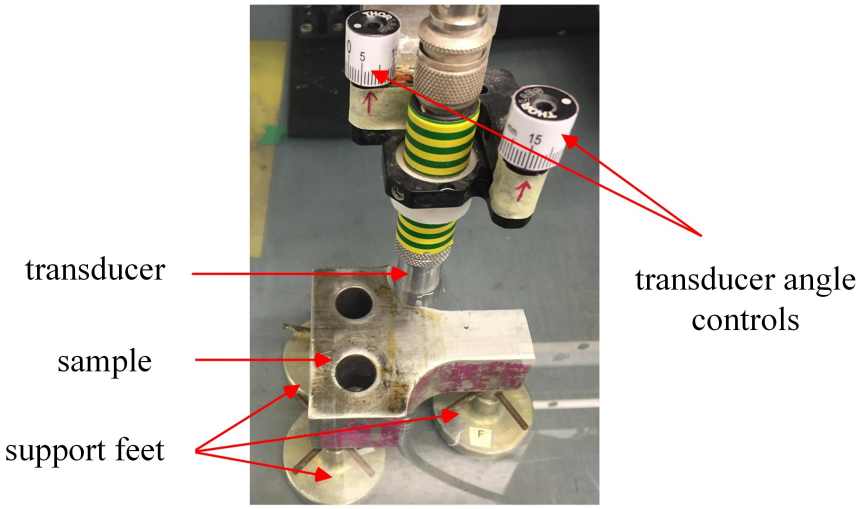


Figure 2.3: Experimental setup of the immersion tests conducted in this chapter.

in this study are shown in Table 2.1. The results of Sections 2.2 and 2.3 were obtained with Transducer 1; Transducers 2 and 3 were used in Section 2.4. It should be noted here that the purpose of this chapter is to discuss the feasibility of using baseline subtraction for grain noise removal so sufficient grain noise needs to be generated in the experiments. It was found that this sample exhibits appropriate grain noise when excited by a 7.5 MHz transducer, so this centre frequency was used in all the experiments. It is not suggested that this is the optimum frequency for inspection of this component; the experimental setup was chosen simply to generate significant grain noise so that the feasibility of its removal via baseline subtraction could be investigated. Typical A-scan results are shown in Figure 2.4, where to show the wave propagation time in the sample clearly, both signals are shifted to make the frontwall peak at time zero. As the intensity of the backscattered energy was significantly less than that of the frontwall reflection, the Analog-to-Digital Converter (ADC) range used for collecting the grain noise was around 48 dB below that for frontwall capture and hence the frontwall signals are clipped in Figure 2.4b.

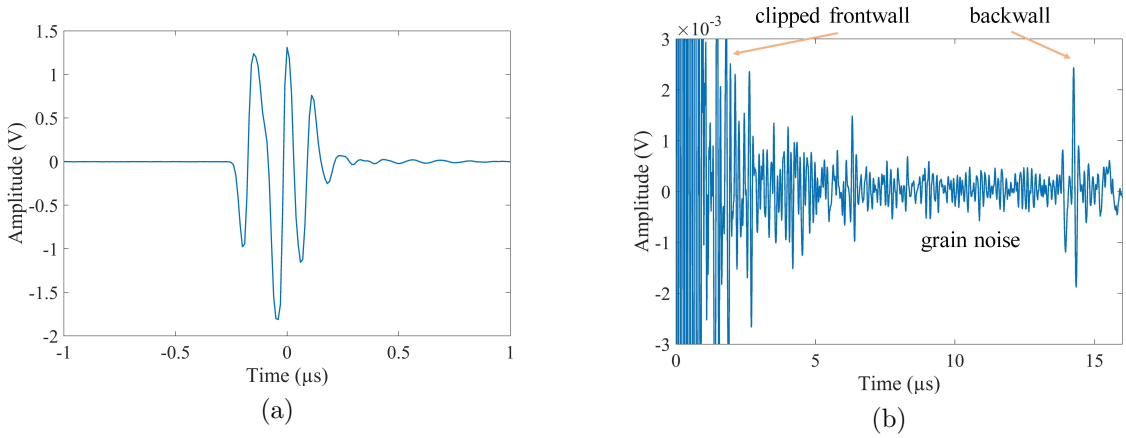


Figure 2.4: Typical A-scan signals obtained with Transducer 1 (a) frontwall (b) whole signal with clipped frontwall. Both signals are shifted to make the frontwall peak at time zero.

Table 2.1: Transducers used; all were unfocused

Transducers	Manufacturer	Centre Frequency (MHz)	Diameter (in)
1	IMASONIC	7.5	0.24
2	GE	7.5	0.50
3	GE	7.5	0.50

2.3 Repeatability test

As shown in Figure 2.2, there are several potential errors due to the transducer setup in repeat inspections that would cause the incident wave to interact with different grains and so generate different grain noise. In order to suppress grain noise with baseline subtraction, the same relative position of the transducer and sample in repeat tests must be found. In this section, the feasibility and reliability of finding this same relative position in repeat inspections is studied.

2.3.1 Transducer angle

It can be clearly seen that in Figure 2.2a, an ultrasound wave at different incident angles interacts with different grains, hence generating different grain noise. Thus, accurately

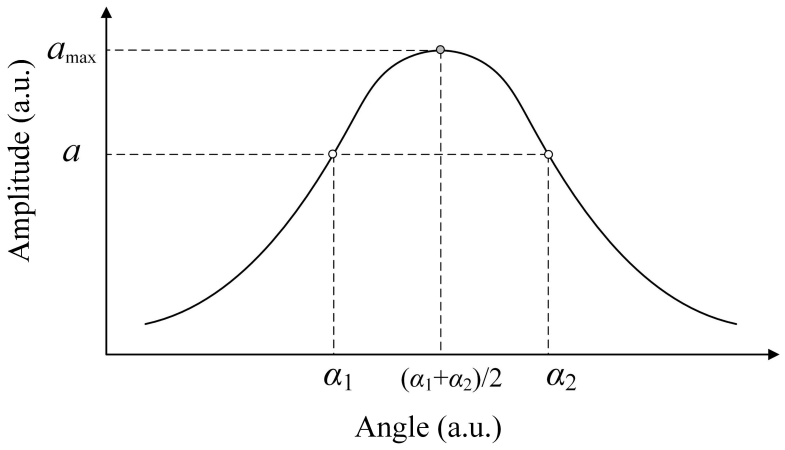


Figure 2.5: Schematic diagram of transducer alignment method.

adjusting the transducer to be perpendicular to the sample in each setup is necessary. Maximum signal calibration, referred to as the standard method here, is commonly used to find the normal incident angle. This method adjusts the transducer by finding the maximum amplitude of the frontwall echo. In theory, the frontwall amplitude reaches the maximum when the transducer is normal to the sample. However, around the peak, the rate of change of amplitude with angle is too small for an inspector to manually adjust the angle to a satisfactory precision.

An alternative method is shown schematically in Figure 2.5. Firstly, the transducer is adjusted to be roughly perpendicular to the sample using the standard method. Then the transducer is rotated about the x axis (θ_x in Figure 2.1) until a significant amplitude reduction is seen and the amplitude and angle setting are recorded; the transducer is then rotated in the opposite direction until the same amplitude is obtained on the other side of the peak. The optimum angle is then the mean of the two recorded angles. The same procedure is then followed with the θ_y adjustment and the process can be iterated if necessary.

The two calibration methods were then used to adjust the transducer angle and quantify the influence of an angle error on baseline subtraction. For each method, eight A-scans were recorded having reset the angle between each reading; the first reading was then used

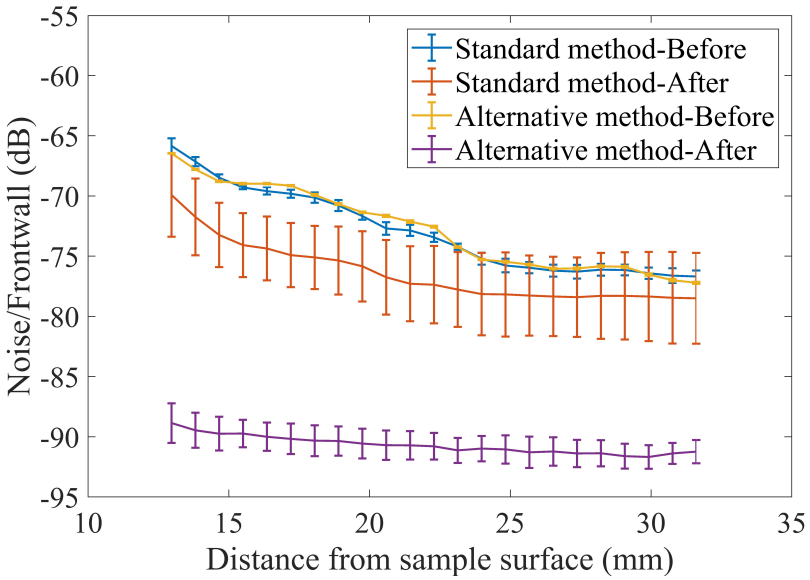


Figure 2.6: Noise to frontwall amplitude ratio versus distance from sample surface before and after baseline subtraction. The data consists of eight A-scans where the first represents the baseline and the seven successive traces are used for subtraction. Each data point shows the mean (line) and standard deviation (bar) of the RMS for a 14 mm window centred about its indicated $x-$axis value. The range of depths considered here corresponds to the grain noise which lies in-between the frontwall and backwall signals. Electrical noise residual is around 94 dB below the frontwall signal.

as the baseline and the subsequent readings were subtracted from it; the test was repeated at three randomly selected positions to verify the robustness of the method to different grain geometry. The results at one position are shown in Figure 2.6; the blue and yellow curves show the mean grain noise level of the seven subsequent A-scans as a function of depth; the points show the root mean square (RMS) over a 14 mm range centred on the marked depth for the standard method and the alternative method respectively. As the RMS values are calculated over a 14 mm range, the central depth used for calculation is from 13 mm to 32 mm (the total depth is 40 mm) to remove the influence of the frontwall and backwall on the RMS grain noise calculation. It can be seen that there is little difference between these curves. In contrast, the red and purple curves show the mean residual level after baseline subtraction for the standard method and the alternative method respectively, together with error bars corresponding to the standard deviation of the noise level obtained from seven baseline subtracted residuals. It can be seen that the residual obtained with the alternative method, which is around 18 dB lower than the noise level in a single signal, is an average of about 14 dB better than that with the standard method and the variability is substantially lower. The level of improvement with both methods decreases with depth; this may be because when beams at different incident angles travel deeper into the sample, the spatial separation between them increases so the probability of them interacting with different grains increases. Similar results were obtained at the other two test positions. It is shown that the alternative method is more reliable for the transducer angle adjustment and it provides high repeatability and accuracy in transducer angle setting, thereby making it possible to use baseline subtraction to suppress grain noise in repeat scanning. As a cautionary note, due to a single operator performing both methods for the present investigation, the variability of operator skill is not taken into account. Although this plays a role in determining performance for both methods, we have assumed the investigator to be representative of the average skill for both methods.

2.3.2 Transducer stand-off

A transducer stand-off change, shown in Figure 2.2b, is very likely to happen in repeat inspections. The change in the distance between the transducer and sample introduces a shift in received signals. In addition, due to beam spreading, the pressure distribution on the sample surface also changes with distance. This results in different grains interacting with the beam and so different grain noise being generated. Therefore, we need to accurately adjust the transducer stand-off to generate the same grain noise in each setup to make it possible to remove the grain noise by baseline subtraction.

Assuming a constant speed, there is a one-to-one correspondence between distance and time. Therefore, the frontwall arrival time is often used to adjust the transducer stand-off. However, in repeat tests, the temperature can be different, which causes a difference in wave speed and so changes the relationship between the distance and time. In this case, if a transducer is adjusted using the arrival time of a frontwall signal collected at a different temperature, a stand-off error will be introduced. For example, suppose a reference frontwall arrival time obtained at 19 °C when the stand-off is 65 mm. If this reference time is used to adjust the transducer stand-off when the temperature changes to 22 °C, a stand-off difference of around 0.4 mm will be introduced.

In order to see how much this difference influences baseline subtraction, the stand-off was changed with a motor from 65 mm to 65.5 mm to simulate the effect of a small temperature change on the transducer stand-off adjustment. At each stand-off, tests were repeated ten times. The first reading of the ten at 65 mm stand-off was used as the baseline and subsequent readings were subtracted from it. Figure 2.7 shows the average improvement between raw grain noise level and residual after baseline subtraction over the thickness of the sample at different stand-offs. It is clear that small variations in stand-off have only a minor effect on the residual after subtraction and the standard deviation.

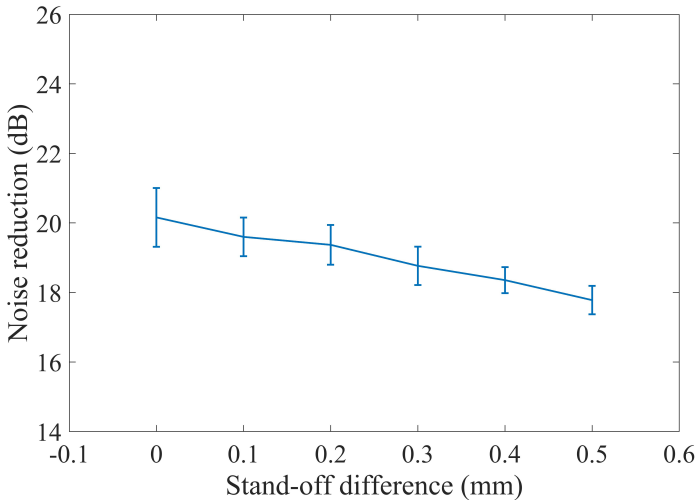
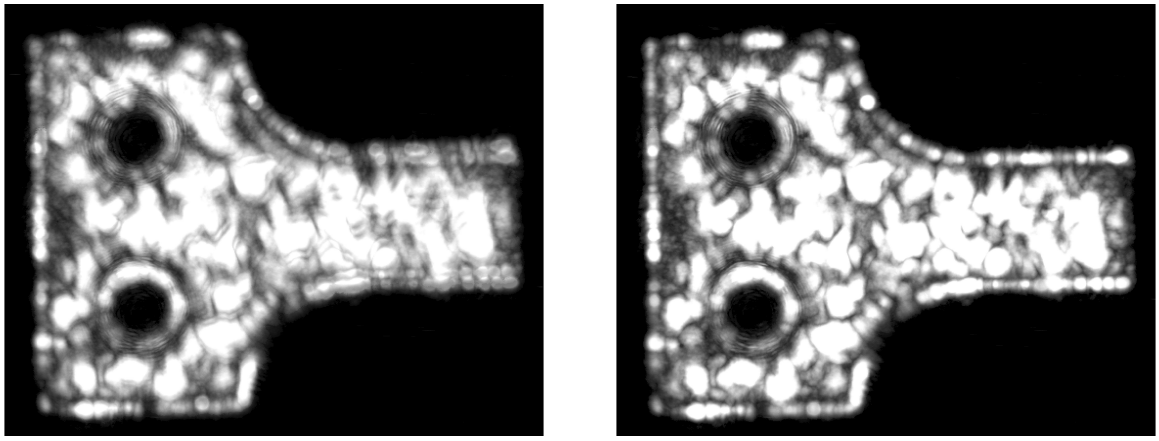


Figure 2.7: Mean noise reduction over sample depth after baseline subtraction as a function of transducer stand-off difference. Error bars show the standard deviation of ten repeats at each stand-off.

2.3.3 Test position

It is obvious that if tests are carried out at different positions on the sample, the ultrasound wave will interact with different grains (as shown in Figure 2.2c) and then different grain noise will be generated. If the grain noise in the baseline is different from that in the current signal, baseline subtraction will be ineffective in grain noise suppression. Therefore, in order to suppress grain noise, the subtraction needs to be conducted at the same positions. Locating a specific position by conducting single A-scans is difficult. However, it becomes possible to locate a position by aligning different C-scans. The alignment of two C-scan images is done by using one of them as the target and translating and rotating the other one with the relative translations in x and y directions and the rotation angle being determined from the maximum correlation coefficient.

C-scans of the backwall echo amplitude across the whole sample were carried out four times, and before each scan, the rig was recalibrated by removing and readjusting the transducer and sample. Figure 2.8 shows overlapped images of the first and second C-scans before and after alignment. It can be seen that before registration, the position and



(a) (b)

Figure 2.8: Overlapped C-scan images (backwall echo amplitude) from repeat tests (a) before and (b) after alignment.

orientation of the sample in the two images are different; after registration, the scans are well aligned. A-scans at ten randomly distributed positions on the sample were extracted from the registered C-scans. The A-scans of the first C-scan were used as the baselines and the A-scans from the subsequent C-scans were subtracted from them. The RMS grain noise to frontwall amplitude ratio over the thickness of the sample before and after baseline subtraction was calculated for each of the 10 points. The average of the grain noise level at the ten points in the second C-scan is shown in Figure 2.9, together with the mean residual after subtraction from the corresponding signals in the first C-scan. It can be seen that after subtraction, the residual is an average of around 15 dB lower than the grain noise and there is no obvious change in the variability. Similar results were obtained with signals from the third and fourth C-scans.

It can be seen from Figure 2.8 that the sample boundary is a very clear structural feature, and features like this are likely to dominate the registration process. However, in some circumstance scans may be recorded over regions where there is no clear boundary. In order to test whether the registration procedure is still effective in this case, another C-scan of a small area containing no boundary of the sample was conducted. This C-scan was aligned with the first C-scan of the whole sample using the registration method. It

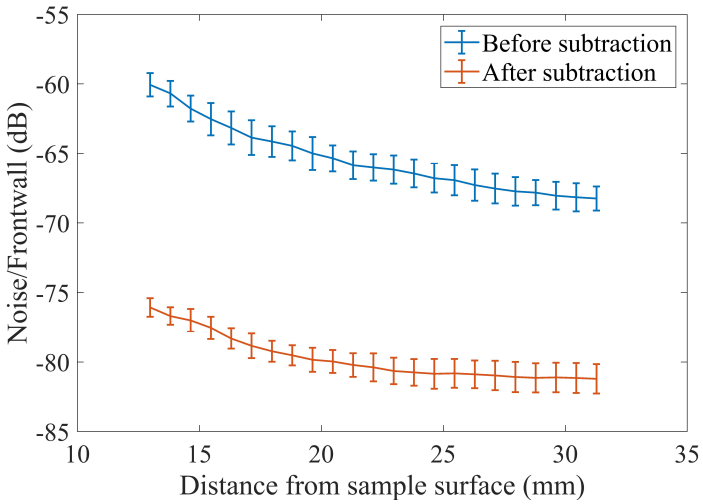


Figure 2.9: Noise to frontwall amplitude ratio versus distance from sample surface before and after baseline subtraction. The data consists of ten A-scans from the first C-scan representing the baselines and the other ten traces from the second C-scan used for subtraction. Each data point shows the mean (line) and standard deviation (bar) of the RMS for a 14 mm window centred about its indicated $x-$axis value. The range of depths considered here corresponds to the grain noise which lies in-between the frontwall and backwall signals. Electrical noise residual is around 84 dB below the frontwall signal.

was found that the registration process correctly located the scan of the small region onto the larger scan, showing that for highly scattering materials, grain features are sufficiently rich for satisfactory C-scan registration. After registration, A-scans at six randomly distributed positions on the sample were extracted from the C-scans. By subtracting the A-scans of the smaller area C-scan from the corresponding signals of the whole sample C-scan, an average noise reduction of around 15 dB was obtained. The results therefore show that the image alignment method enables C-scans to be registered accurately enough to give residual noise levels after subtraction similar to those obtained in repeat tests at the same point.

2.4 Compensation

As mentioned above, setup errors can cause the ultrasound wave to interact with different grains and so generate different grain noise. However, even if the setup is identical, the grain noise can still be different, since it can also be affected by other factors, such as temperature variations and transducer frequency response changes, both of which are very likely to happen in repeat scans. Temperature variations can change the wave speed, and transducer frequency response changes can affect the waveform, thereby modifying the ultrasonic response, which makes raw subtraction ineffective. Therefore, compensation for these changes needs to be conducted before using baseline subtraction. In this section, compensation methods for the temperature and transducer frequency response changes are presented, along with experimental results to test their effectiveness.

2.4.1 Temperature compensation

2.4.1.1 Influence of temperature on baseline subtraction

Temperature changes can significantly influence wave propagation. Before introducing compensation methods, the influence of temperature change on baseline subtraction is

briefly presented here [86].

Two tonebursts (Hann-windowed here, but the analysis is not limited to this case.) I_0 and I_1, with a temperature difference δT which causes an arrival time difference δt, are used as the baseline and current signals.

$$I_0 = u_0 \mathrm{hw}(t) \sin(\omega t) \tag{2.1}$$

$$I_1 = u_0 \mathrm{hw}(t + \delta t) \sin\left(\omega(t + \delta t)\right) \tag{2.2}$$

where u_0 is the amplitude, and in this case, $\mathrm{hw}(t)$ is the Hann-window function, t is time and ω is the angular frequency.

For RF subtraction, the main concern is the phase shift caused by the temperature change, which is not affected by the window, thus the difference between $\mathrm{hw}(t)$ and $\mathrm{hw}(t + \delta t)$ is neglected. Hence, the result of subtracting I_0 from I_1 can be written as

$$I_1 - I_0 \approx u_0 \mathrm{hw}(t)(\sin\left(\omega(t + \delta t)\right) - \sin\left(\omega t\right)) \tag{2.3}$$

Assuming δt is small enough, the small angle approximation can be applied

$$I_1 - I_0 \approx 2\pi f u_0 \mathrm{hw}(t) \delta t \tag{2.4}$$

where f is frequency.

According to [81], the time shift due to the temperature change δT can be expressed as

$$\delta t = \frac{d}{v}(\alpha - \frac{k}{v})\delta T \tag{2.5}$$

where d is the propagation distance, v is the phase velocity, α is the thermal expansion coefficient and $k = \delta v / \delta T$.

Therefore,

$$I_1 - I_0 \approx 2\pi f u_0 \mathrm{hw}(t)\frac{d}{v}(\alpha - \frac{k}{v})\delta T \tag{2.6}$$

From Equation 2.6, it can be seen that the residual from direct subtraction increases with the temperature change, which means that the grain noise will not be suppressed effectively by direct subtraction if δT is significant.

2.4.1.2 Temperature compensation methods

The Optimal Baseline Subtraction (or the Baseline Selection) [81, 87] has been proposed as an effective method to overcome this problem. This method establishes a database of baseline signals obtained from the undamaged structure under the different environmental conditions under which subsequent tests might be conducted. The baseline signal which is most similar to the current signal is then selected in subsequent inspections; this is generally the signal acquired at the closest temperature to that of the current test. The selection is generally done by subtracting all the baseline signals in the database from the signal collected during the inspection and choosing the one giving the minimum residual after subtraction. However, it is impractical to have a database covering all environmental conditions at a small enough temperature step.

The Optimal Stretch method is another common technique [88, 89], which uses a signal processing method to compensate for the temperature difference. As shown in Equation 2.5, the temperature change introduces a time shift, which can be corrected by stretching the signal in either the time [88] or frequency [89] domain. The advantage of the Optimal Stretch method is that it only needs one baseline signal; however the drawback of the method is that the stretching distorts the waveforms as well as changing the arrival time and this, coupled with other factors such as multiple overlapping echoes, limits the temperature difference that can be compensated [86]. A combination of Optimal Baseline Subtraction and Optimal Stretch has been shown to be an effective way of reducing the

number of baselines needed in the optimal baseline method while not requiring excessive stretch.

The Optimal Baseline Subtraction and the Optimal Stretch techniques have been successfully applied in guided wave monitoring where the wave propagates in only one medium. However, in immersion ultrasonic testing the wave propagates in both the testpiece and the coupling medium that have very different temperature coefficients. They must therefore be considered separately.

In this chapter, the Optimal Stretch technique is used to compensate for temperature changes in the sample. Since the effects of temperature on wave propagation in water and metal need to be considered separately, a two-step temperature compensation method is used. The first step is to align the frontwalls of the baseline and current signals in order to eliminate the temperature influences on the wave propagation in water; the alignment is done by cross correlating the frontwall signals. Then, a scale-transform-based stretch method [85] is used to compensate for the wave speed change in the metal.

2.4.1.3 Experimental results

In order to test the effectiveness of the temperature compensation method, it was used to compensate for the difference in signals collected at different temperatures. This temperature difference was achieved by changing the temperature of the water used in the immersion tests. The water was heated up to around 33 °C and then naturally cooled down to room temperature (around 23 °C); a Pico PT-104 Platinum Resistance Data Logger was used to record the water temperature data. A-scans were recorded with Transducer 2 at the same position every 80 seconds; this gave 331 readings between 33 °C and room temperature.

The noise level across the thickness of the sample at 33 °C is shown in Figure 2.10, together with the residual after subtraction from the signal at 23 °C with and without temperature compensation. It can be seen that after subtraction without temperature

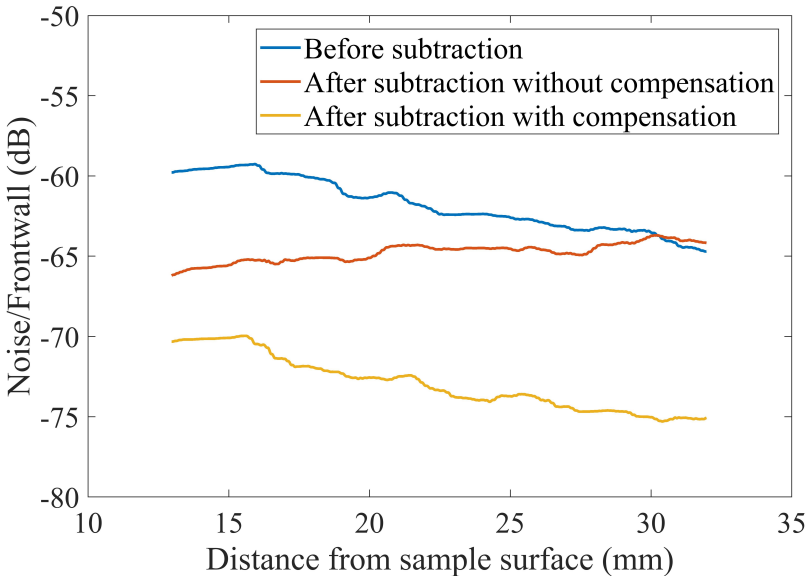


Figure 2.10: Noise to frontwall amplitude ratio versus distance from sample surface before subtraction and after subtraction with and without temperature compensation. Each data point shows the RMS for a 14 mm window centred about its indicated $x-$axis value. The range of depths considered here corresponds to the grain noise which lies in-between the frontwall and backwall signals. The temperatures of the baseline and current signals are 23 °C and 33 °C respectively. Electrical noise residual is around 98 dB below the frontwall signal.

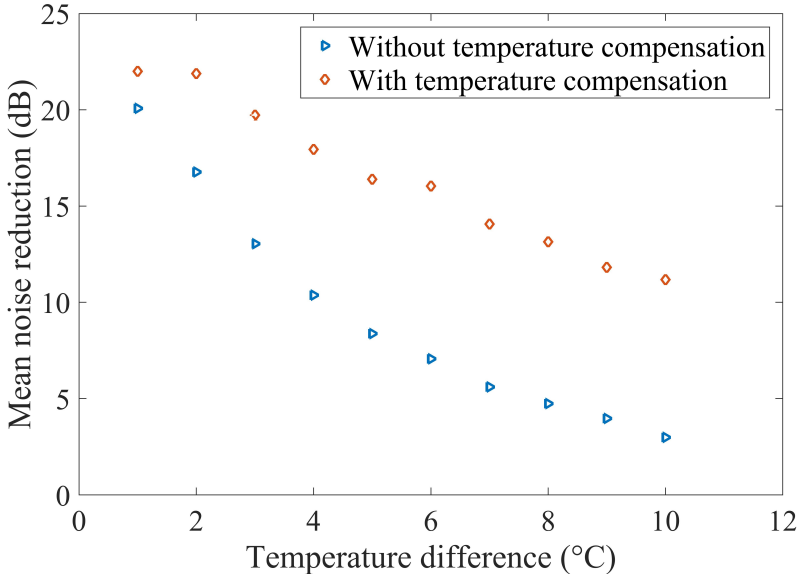


Figure 2.11: Mean noise reduction after subtraction with and without temperature compensation at different temperatures. The temperature of the baseline signal is 23 °C.

compensation, the residual increases with increasing depth; at above around 30 mm, it is even higher than the original noise level. This is because the temperature change causes a wave speed change and the phase shift produced increases with distance travelled. After temperature compensation, the residual is reduced by about 11 dB compared to the original grain noise, approximately independent of depth. This shows that temperature compensation is very effective and compared to the raw subtraction without temperature compensation, the noise reduction increases with increasing depth.

The effect of temperature difference between the baseline and current signals was then investigated. Figure 2.11 shows the average noise reduction over the depth of the sample as a function of temperature difference between the current signal and the baseline at 23 °C. The reduction in the residual noise level decreases with increasing temperature difference both with and without compensation, but the drop is significantly less rapid when compensation is applied. When the temperature difference is 1 °C, the improvement with compensation is only 2 dB; this is because the noise reduction of about 20 dB

is already at a similar level to that shown in Figure 2.7 for subtraction with minimal temperature difference. At higher temperature differences the improvement rises to about 8 dB. It is shown that it is feasible to obtain a noise reduction of around 11 dB via temperature compensation and subtraction, where a temperature difference up to 10 °C can be tolerated.

2.4.2 Compensation for transducer frequency response change

In repeat inspections at long time intervals, it is likely that different transducers with similar specifications would be used in successive tests, and even if the same transducers are used, their frequency response could change due to ageing. As a result, the later received signals will not have the same grain noise even though the same grains are inspected, and baseline subtraction will not perfectly remove grain noise to reveal small reflections from defects. Therefore, we need to compensate for the potential differences in transducer response. In this section, we demonstrate a frequency compensation scheme that uses the frontwall reflection to calibrate for changes in transducer frequency response, and to reduce the difference in the received grain noise so that it can be removed by baseline subtraction. This method also accounts for any change in the excitation and reception electronics. It is possible that other changes may occur due to transducer ageing, e.g., the effective transducer area could change and so alter the field pattern. However, we believe that frequency response changes are likely to be the major effect.

2.4.2.1 Methodology

In an immersion inspection configuration, the ultrasonic wave excited by the transducer first propagates through a liquid medium before arriving at the interface of the testpiece. Depending on the impedance difference, a portion of the signal is reflected from the front surface and the rest of the signal being transmitted into the material. The reflected and transmitted signals have the same frequency content, and are equally affected by the

change in the transducer response. Assuming linearity, the frontwall signal $F(\omega)$ reflected from the interface and received by the transducer can be written as

$$F(\omega) = X(\omega)h_{\mathrm{T}}(\omega)h_1(\omega)h_{\mathrm{T}}(\omega) \tag{2.7}$$

where $X(\omega)$ is the excitation signal and $h_{\mathrm{T}}(\omega)$ and $h_1(\omega)$ are the transfer functions of the transducer and the transmitting and receiving path of $F(\omega)$. The reflection signal $Y(\omega)$ received by the transducer from inside of the testpiece can be written as

$$Y(\omega) = X(\omega)h_{\mathrm{T}}(\omega)h_2(\omega)h_{\mathrm{T}}(\omega) \tag{2.8}$$

where $h_2(\omega)$ is the transfer function of the transmitting and receiving path of $Y(\omega)$.

From Equation 2.8, it can be seen that if $h_{\mathrm{T}}(\omega)$ changes to $h'_{\mathrm{T}}(\omega)$, due to transducer ageing or the use of a different transducer, the new received signal $Y'(\omega)$ would be different from the original $Y(\omega)$, limiting the utility of direct subtraction in the time domain.

To reliably compare the received signals from different inspections, this difference has to be compensated, so that $Y(\omega)$ is similar to $Y'(\omega)$ if no defect exists along the propagation path. If all other factors (inspection location, incident angle, etc) are the same, the transfer functions $h_1(\omega)$ and $h_2(\omega)$ remain the same for the particular paths in different inspections. Then by comparing Equation 2.7 and 2.8, it can be found that $Y(\omega)/Y'(\omega) = F(\omega)/F'(\omega)$, which indicates that the frontwall reflection signal can be used to calibrate the change in the transducer response and adjust the received signal in the frequency domain for both amplitude and phase differences. Considering $F(\omega)$ and $F'(\omega)$ are the Fourier transform of the baseline and current frontwalls and $Y'(\omega)$ is that of the current signal, we can obtain the Fourier transform of the compensated current signal

$$\bar{Y}(\omega) = \frac{F(\omega)}{F'(\omega)}Y'(\omega) \tag{2.9}$$

To avoid extremes in the compensation term (F/F'), we filtered the frequency response F with a threshold 15 dB below the peak of the response, i.e. we set the values below the threshold to be zero. The threshold to use in practice should be determined by the SNR of the frontwall signal. The inverse Fourier transform of $\bar{Y}(\omega)$ then resembles the compensated current signal $\bar{y}(t)$, whereas any difference between the baseline and compensated current signals may suggest the existence of a potential defect.

2.4.2.2 Experimental setup

We test the scheme for three types of change:

1. change in the excitation frequency spectrum;
2. change of transducer;
3. a combination of the two.

Two nominally identical 7.5 MHz transducers (Transducers 2 and 3) were used to scan our specimen (shown in Figure 2.3) at 41×16 locations covering a 20×7.5 mm^2 area. We repeated the C-scan with each transducer four times, each time exciting the transducer with a square wave having a different pulse-width, effectively changing the frequency spectrum of the excitation. When the transducer was changed for the second set of four C-scans, the stand-off and angle adjustment techniques and the C-scan registration procedure described in Section 2.3 were used.

Figure 2.12 shows typical frontwall reflection signals obtained at one location. Figure 2.12a-d show time traces of the frontwall reflection, and Figure 2.12e-h show the corresponding frequency responses. We use the peak frequencies to refer to the excitations in the following text, but note that the entire frequency spectrum changes besides the small shift in the peak frequency; the peak frequencies of the excitation in Figure 2.12a-d

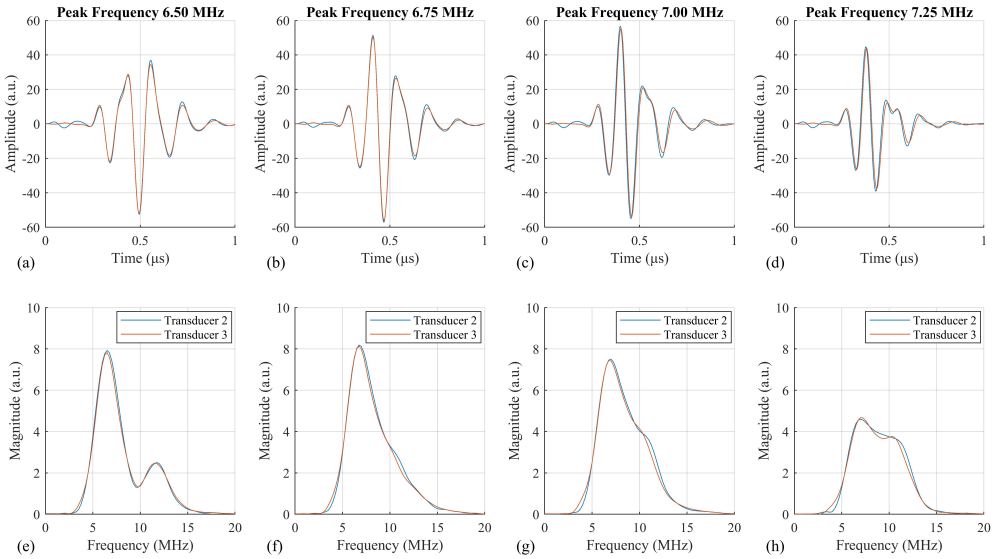


Figure 2.12: Typical A-scans showing the frontwall reflection. Plots (a-d) and (e-h) represent the time and frequency domain signals collected with different excitations, whose peak frequencies are respectively 6.5, 6.75, 7.0 and 7.25 MHz. Blue and red represent signals obtained from two different transducers.

are, respectively, 6.50, 6.75, 7.00 and 7.25 MHz. The frequency responses of Figure 2.12f and 2.12g are relatively simple because the excitation is well matched to the transducer resonance, whereas the 6.5 MHz and 7.25 MHz excitations give the distorted frequency responses of Figure 2.12e and 2.12h respectively.

It is clear from Figure 2.12 that the signals from two transducers differ slightly. However, as the wave propagates through the grains, the scattered grain noise signals become substantially different, as shown in Figure 2.13. Note that the frontwall (at time zero) and backwall (at 14 μs) reflection signals in Figure 2.13 are clipped because the signals are amplified to give better resolution of the grain noise signals in between.

Direct subtraction between any pair of the signals of Figure 2.13 will not perfectly remove the grain noise, thereby reducing the ability to detect small defects in the material. The frequency compensation scheme aims to correct this. By comparing different pairs of signals, we simulate different practical scenarios:

1. comparing two signals from different plots with the same color simulates repeat

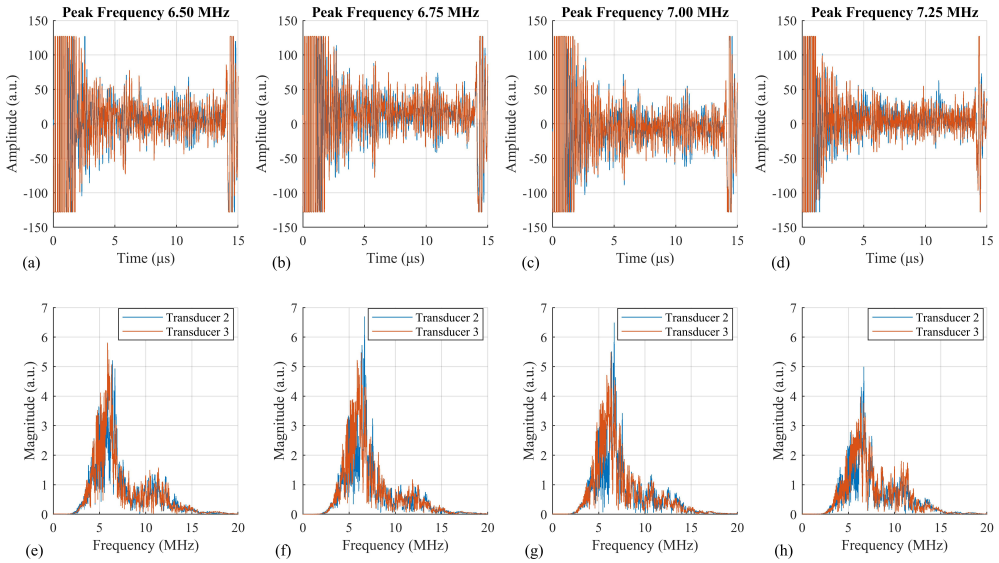


Figure 2.13: Typical A-scans showing the grain noise signals in between frontwall and backwall reflections. Plots (a-d) and (e-h) represent the time and frequency domain signals collected with different excitation, whose peak frequencies are respectively 6.5, 6.75, 7.0 and 7.25 MHz. Blue and red represent signals obtained from two different transducers.

inspections with the same transducer but with different excitation electronics or after transducer ageing;

2. comparing the two signals with different colors in any plot in Figure 2.13 simulates repeat inspection with different transducers but identical excitations;

3. comparing two signals from different plots with different colors simulates repeat inspection with different transducers and different excitations.

2.4.2.3 Experimental results before and after compensation

We process all pairs from the eight different signals from two transducers and four excitations, and show the results before and after the frequency compensation. We first show the absolute correlation coefficients that indicate the similarity between two signals on a 0 to 1 scale, where a unity correlation coefficient suggests the two signals have identical shapes. Figure 2.14 shows the correlation coefficients between the baseline signal with

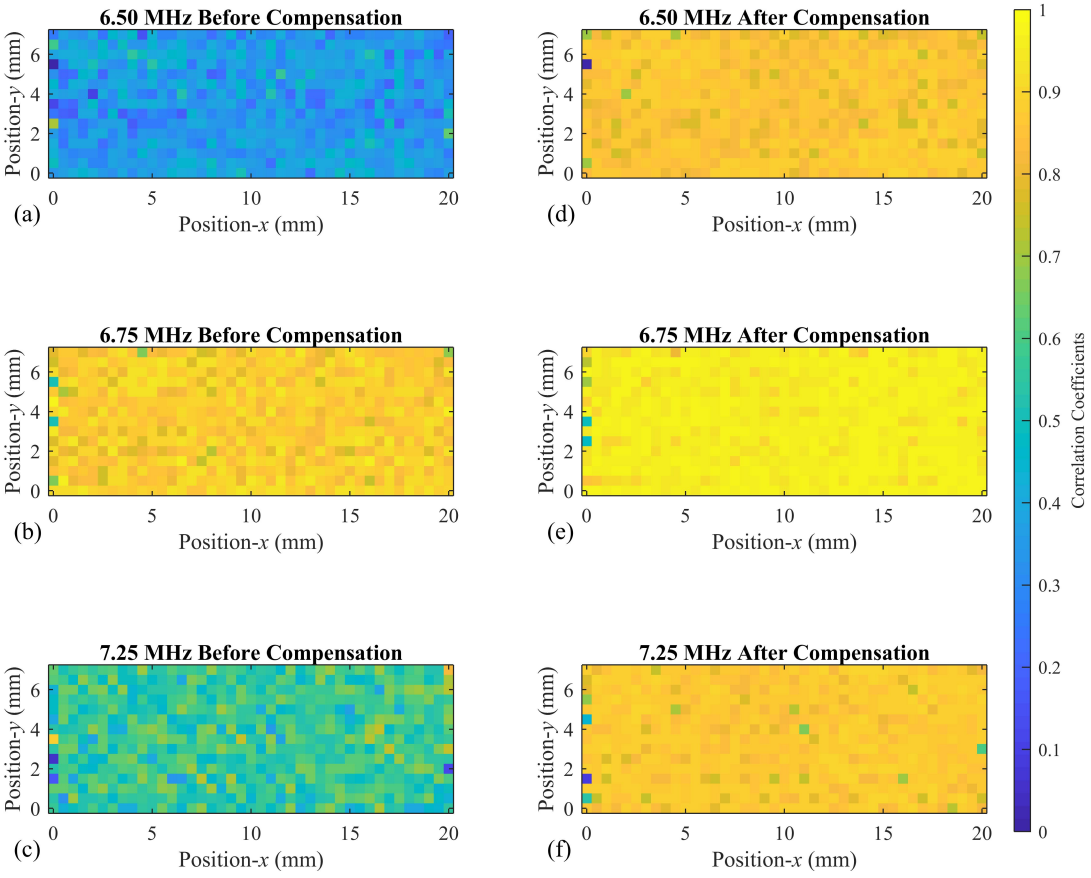


Figure 2.14: Correlation coefficients before (a-c) and after (d-f) frequency compensation at 41×16 locations with an area of 20×7.5 mm^2 on the sample. Compensation is conducted using signals with peak frequency of 7.00 MHz as the baselines. (a, d), (b, e) and (c, f) correspond to the results using signals with peak frequencies of, respectively, 6.50, 6.75 and 7.25 MHz.

peak frequency of 7.0 MHz and a current signal with other peak frequencies on all 41×16 locations on the sample covering an area of 20×7.5 mm^2. The signals were all collected with one transducer but with different excitation frequency spectra, corresponding to scenario 1 above.

Figure 2.14a-2.14c show correlation coefficients between baseline and current signals without compensation. Light-yellow pixels indicate correlation coefficients close to unity, which means the baseline and current signals are alike, and dark-blue pixels indicates the two signals are dissimilar. It can be seen that a small difference in frequency spectrum can significantly change the grain noise signals. For example, when comparing signals using 7.00 MHz excitation and signals using 6.50 MHz excitation, the mean correlation coefficient across the points is as low as 0.2.

Figure 2.14d-2.14f show the correlation coefficients after the signals are compensated using the procedure of Section 2.4.2.1, the baseline being the signals with 7.00 MHz excitation. There is a clear improvement in correlation coefficients, suggesting that baseline subtraction will be more effective.

Figure 2.15 shows the mean noise reduction across the scan area obtained by processing the signals with frequency compensation and baseline subtraction, compared to the noise level in the original baseline inspection. A x dB noise reduction means that by compensating and subtracting the signal, we can suppress the grain noise by x dB. Figure 2.15a shows the results where signals were taken with different excitations, where the horizontal and vertical axes correspond to the excitation peak frequencies for, respectively, the current and baseline signals used in the subtraction. As an example, the second row from the top in Figure 2.15a corresponds to the test scenario in Figure 2.14, where we compare current signals obtained with an excitation peak frequency of 7.00 MHz with baseline signals taken at other excitation peak frequencies. Figure 2.15b shows the corresponding results when the signals were taken with two different transducers.

The diagonal line from top right to bottom left in Figure 2.15a when the baseline

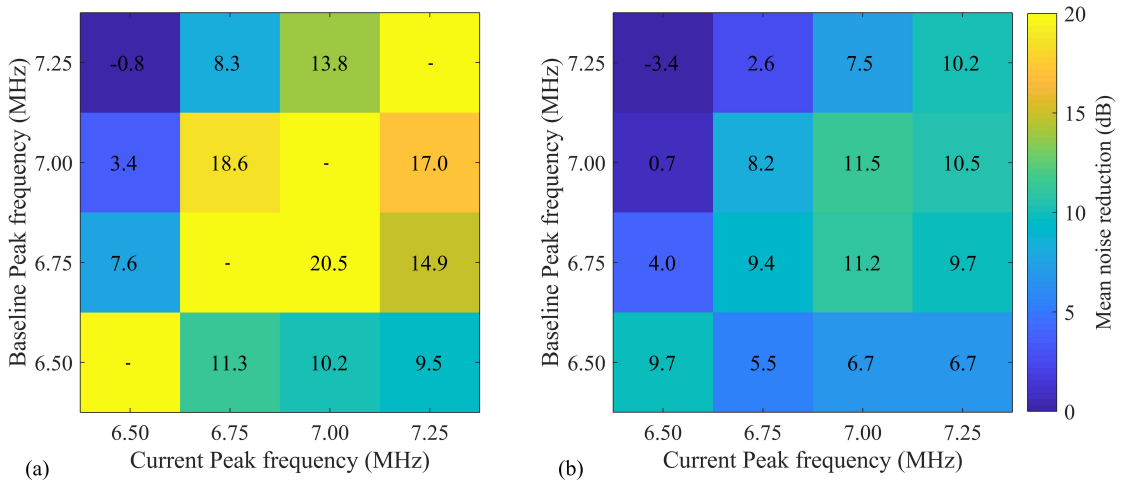


Figure 2.15: Mean noise reduction across the scan area from compensation and subtraction compared to the original baseline inspection. (a) Current and baseline signals were measured from the same transducer. (b) Current and baseline signals were measured from different transducers. Horizontal and vertical axes indicate the peak frequencies of the excitation used in, respectively, current and baseline signals.

and current excitations signals are the same is left blank because here the signals are identical. The off-diagonal values correspond to the cases where excitations are different and need to be compensated. Note that the image is asymmetric, the values in the bottom triangle being larger than their counterparts in the upper triangle. This is because the excitation was controlled by the pulse width of a square wave, so a higher peak frequency corresponds to a wider bandwidth; compensating for frequency response differences is easier when going from a wide band signal to a narrower band signal than vice versa. When compensating from wider band to narrower band for the same transducer, an improvement of 14-20 dB was obtained when the spectrum of the signal is relatively simple as in Figure 2.12f and 2.12g; the gain was much smaller when the distorted spectrum of Figure 2.12e was used.

The diagonal line from top right to bottom left in Figure 2.15b represents the case where the baseline and current signals were taken with different transducers but with nominally the same excitations. In this case, a gain of about 10 dB was obtained from the compensation and subtraction compared to the baseline inspection. The off-diagonal values suggest that when the response spectrum has a simple form and the frequency difference between current and baseline excitations is small (where the peak frequency response changes as much as 250 kHz), a gain of over 10 dB can still be obtained from the compensation procedure; when difference between the spectra increases, the noise reduction drops quickly. It should be noted that the repeat scans with different transducers involve resetting the transducer. Therefore, the results show the combined noise reduction of the frequency response compensation and the stand-off adjustment, angle calibration and image registration procedure illustrated in Section 2.3. This is what would be involved in a real case of two inspections before and after a period in service.

Table 2.2: The improvement achieved by calibrating and/or compensating for various factors in baseline subtraction

Calibrated/Compensated Factors (differences between current and baseline signals)		Improvement level
Re-setup	Angle	18 dB
	Stand-off	17 dB
	Angle, Stand-off and Lateral positions	15 dB
Temperature (10 °C test temperature change between baseline and current signals.)		11 dB
Transducer frequency response change (with the same transducer; relatively simple frequency spectrum; a peak frequency difference of ±250 kHz from a baseline value of 7 MHz)		14-20 dB
Transducer frequency response change (with different transducers, thus including all above factors due to transducer re-setup; relatively simple frequency spectrum; a peak frequency difference of ±250 kHz from a baseline value of 7 MHz)		10 dB

2.4.3 Overall influence of different factors

The influence of various experimental and environmental parameters after calibration and/or compensation are compared in Table 2.2. It shows that if the transducer and sample are reset up with no environmental changes, using appropriate calibration methods, an improvement of 15 dB can be obtained with baseline subtraction. However modest changes in test temperature and transducer frequency response are less successfully compensated, dropping the overall improvement to 10 dB. Also the tests were done in a lab environment with no changes to the sample surface due to oxidation or corrosion that would significantly affect the ultrasonic signals. It has also been assumed that no changes to grain structure affecting the ultrasonic signal occur with exposure to service environments as indicated in [84]; if this assumption is not valid in a particular application then baseline subtraction could not be used.

2.5 Summary of the chapter

In this chapter, the feasibility and reliability of comparing repeat tests using baseline subtraction to suppress grain noise has been studied. The feasibility of setting the transducer with the same stand-off and angle relative to the testpiece in repeat immersion tests has been investigated and the influence of errors due to the transducer settings has been illustrated. An image alignment method has been used to register the C-scans and so to compare the same location within the different scans; the effect of errors in the registration has been investigated. The results show that the residual grain noise can be reduced by around 15 dB via baseline subtraction, which offers a much higher defect detection sensitivity.

Since repeat tests may be carried out at different temperatures and with different transducers of similar but non-identical specifications, compensation methods for temperature variations and transducer frequency response changes have been presented and their effectiveness has been tested experimentally. After subtracting a temperature compensated baseline from a current signal collected with a temperature difference of 10 °C, an improvement of around 11 dB was obtained. A gain of around 10 dB was achieved with the proposed frequency compensation method when compensating a small frequency shift on different transducers. Overall, it is feasible to obtain a noise reduction of around 10 dB using baseline subtraction in monitoring highly scattering materials when temperature variations are below 10 °C and the transducer peak frequency response changes by as much as ±250 kHz from a baseline value of around 7 MHz; the dominant factors restricting the improvement gained from baseline subtraction are the temperature and transducer frequency response changes. However, this relatively modest improvement is obtained at significant cost in test complexity and data storage requirements. Also, this improvement was obtained in lab conditions with no sample surface or grain structure changes.

This work has been published in [82]. Section 2.4.2 was written by Dr. Chang Liu and

with his kind permission, it is put here for completeness since it was part of the paper and contributes to the overall conclusions. The experimental data used in Section 2.4.2 were collected by the author and the data processing of frequency compensation was done by Dr. Chang Liu.

Chapter 3 A finite element model for ultrasonic backscattering of polycrystalline materials

3.1 Introduction

It has been shown in Chapter 2 that the low SNR caused by the grain boundary scattering can be improved by suppressing the grain noise using the baseline subtraction method. With this method, the SNR is not determined by the initial noise, but the residual noise after subtraction. Therefore, the main efforts are made to improve the similarity of the grain noise between the baseline and current signals, rather than understand the initial grain noise level. However, under some circumstances, e.g. there is a big change in the temperature, transducer frequency response, sample surface or grain structure, it is difficult to get a high similarity to make baseline subtraction effective, even along with the compensation methods. In this case, it is desirable to find other strategies to achieve a good SNR in a raw signal, which requires a good understanding of the noise behaviour.

As reviewed in Section 1.2, the validities of the theories which have been established to describe the grain noise behaviour are often limited to weakly scattering regimes and until recently, computational costs have limited FE simulations to 2D [59, 60]. Since it has been shown in [41, 42] that the 3D FE approach can successfully predict attenuation, this chapter investigates whether it can be used quantitatively for backscattering noise prediction. Initially, a FE model which considers the scattering response from grains on an individual basis is developed and the measured backscattering amplitudes are compared to

the theoretical predictions of the established theories. Then a FE model with the entire aggregate of grains is considered with two transmit-receive configurations, one with a plane wave excitation and incoherent average of the received signals and another one with a finite transducer and coherent average of the received signals. The RMS noise levels of both configurations are compared with the theoretical solutions developed following the derivation of the ISM in [83]. The contribution of shear waves and multiple scattering, and the effect of the coherent attenuation on the grain noise are discussed.

3.2 Measurement and validation of backscattering amplitude

Before using the 3D FE approach to study the grain noise, which is a result of the scattering from an aggregate of grains, it is important to show that this approach can accurately predict the scattering response from a single grain. The theoretical models to describe the L-L scattering of a plane wave by an inclusion in an isotropic host material have been well established; for example, the exact solution for an isotropic spherical inclusion has been given in [90], and a more general solution applicable to a small weakly-scattering inclusion, shown in [91], has been developed based on the Born approximation. This enables the FE approach to be validated by comparing the FE predicted L-L backscattering amplitude of a single grain, which can be regarded as a small inclusion, with the theoretical prediction.

To measure the L-L backscattering amplitude, a "single-grain" FE model, shown in Figure 3.1 is developed. This model has dimensions of $10 \times 10 \times 35$ mm^3 and contains 85×10^6 degrees of freedom. It is meshed with uniform hexahedral elements and the inclusion, located on the central axis, is modelled by the aggregate of elements whose material properties are different from those of the medium. The medium made from an isotropic material, of which the Young's modulus, Poisson's ratio and density are 214 GPa,

0.3 and 8000 kg/m^3 respectively, will be used in all the cases discussed in this section. Symmetry boundary conditions are used on the model surfaces parallel to the $z-$axis, which mirror the model on the boundaries so effectively generate an infinitely wide model with repeating grain structures. All the nodes on one of the model surfaces in the $x-y$ plane which is indicated by the blue arrows in Figure 3.1, are used as transmitters, with which a plane wave propagating in the $z-$direction is effectively generated. The centre frequency of the excitation considered in this section is in the range of 2 MHz to 6 MHz. As the longitudinal velocity of the host material is 6000 m/s, compromising between accuracy and efficiency [92], the element edge length is set as 0.05 mm, so there are at least 20 elements per wavelength. A point receiver located on the central axis is used to capture the first backscattered longitudinal reflection from the inclusion.

When calculating the backscattering amplitude, apart from the amplitude of the reflection from the inclusion, the amplitude of the incident wave illuminating the inclusion is also needed. In addition, limited by the model dimensions, the raw reflection captured by the receiver may be polluted by the boundary reflections. Therefore, another FE model, which is referred to as the reference model, is developed with the same properties and dimensions but without the inclusion. Two point receivers, one at the same location as the centre of the inclusion in the "single-grain" model and the other at the same location as that of the receiver in the "single-grain" model, are used to capture the incident wave arriving at the position of the inclusion and a reference signal which can be used to remove the boundary reflections from the raw signal obtained with the "single-grain" model, thereby revealing a clear reflection from the inclusion.

We begin with a simple case, an isotropic spherical inclusion, and then consider more complicated cases, such as an inclusion with anisotropic material properties or an irregular shape. It is assumed that in all cases, there is no variation in density from the inclusion to the medium, in which case the L-L scattering amplitude in the Born approximation can be written as [47]:

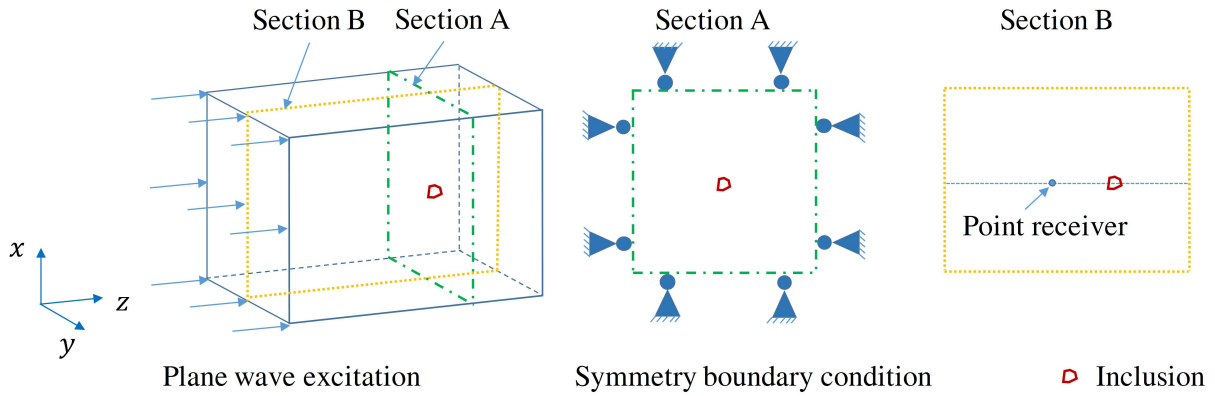


Figure 3.1: "Single-grain" model ($10 \times 10 \times 35$ mm^3): an inclusion located at the central axis along the excitation direction in an isotropic host material is subject to a plane wave excitation. A point receiver used to capture the first backscattered longitudinal reflection from the inclusion is located on the central axis.

$$A = -\frac{\triangle C_{ijkl}}{4\pi\rho v^2} \int \gamma(\mathbf{y}) u^0_{i,j} u^0_{k,l} \, \mathrm{d}V \tag{3.1}$$

where $\triangle C_{ijkl}$ denotes the difference between the elastic constants of the inclusion and the medium; i, j, k, l indicate the directions of the $1-2-3$ coordinate system; ρ is the density; v is the longitudinal wave speed of the host material; V is the volume of the inclusion; $\gamma(\mathbf{y})$ is defined to be unity if $\mathbf{y}$ is inside of the inclusion and zero otherwise; $\mathbf{u}^0$ is the incident displacement field; repeated subscripts indicate summation, while subscripts following the commas indicate derivatives.

If the excitation signal is assumed to be a unit harmonic plane wave propagating in the $z-$direction, which can be expressed as $\mathbf{u}^0 = [0, 0, \mathrm{e}^{\mathrm{j}kz}]$ in the $x - y - z$ coordinate system (corresponding to the $1-2-3$ system), Equation 3.1 can be written as:

$$A = \frac{k^2 \triangle C_{3333}}{4\pi\rho v^2} \int \gamma(\mathbf{y}) \mathrm{e}^{2\mathrm{j}kz} \, \mathrm{d}V \tag{3.2}$$

where $\triangle C_{3333}$, which will be written as $\triangle C_{33}$ in the following text, denotes the difference between the 3333 elastic constant of the inclusion and the medium.

3.2.1 Spherical inclusion

In this section, the backscattering amplitude from an isotropic spherical inclusion under a 4 MHz plane wave excitation is predicted. The radius of the inclusion is 0.31 mm, i.e. 0.2λ. The Young's modulus, Poisson's ratio and density of the inclusion are 223 GPa, 0.3, 8000 kg/m^3 respectively. The relatively small impedance difference (2 %) between the inclusion and the medium is to ensure the validity of the Born approximation, and therefore the accuracy of the theoretical prediction based on that.

By dividing the frequency response of the reflection from the inclusion by that of the incident wave arriving at the inclusion and multiplying it by the distance to account for the spherical divergence of the scattered field, the FE backscattering amplitude can be obtained [91]. This result is plotted as the red dots in Figure 3.2a, along with the prediction of the theoretical solution based on the Born approximation, shown as the blue curve, and that of the exact solution [90], shown as the purple curve. The $x-$axis shows the product of the wave number, denoted by k, and the radius of the inclusion, denoted by b (b is constant at 0.31 mm in Figure 3.2). Good agreement among the three predictions can be seen and this shows the validity of the FE approach in describing the scattering from a spherical isotropic inclusion.

As cubic single-crystal symmetry is considered in this study, it is of great importance to show the validity of the FE approach to accurately predict the scattering from an inclusion with this symmetry. So, next, we will consider the same spherical inclusion under the same excitation but with a cubic material, of which the Voigt averages are the host material properties given in the beginning of Section 3.2. The density and Poisson's ratio are the same as those of the isotropic inclusion, while the elastic constants C_{11}, C_{12} and C_{44} are 266.7 GPa, 134.1 GPa and 92.9 GPa respectively. 100 realisations with random crystallographic orientations of the inclusion are run and the RMS of the 100 backscattering amplitudes is shown as the red dots in Figure 3.2b, along with the error

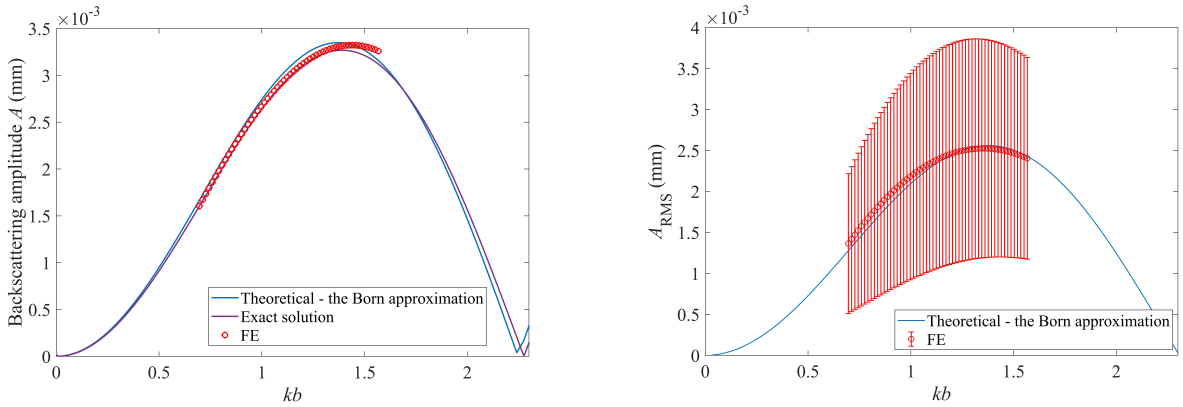


Figure 3.2: Comparison of FE and theoretical backscattering amplitudes of a spherical inclusion with (a) an isotropic material and (b) a cubic material with a Zener anisotropy factor ($A_z = 2C_{44}/(C_{11} - C_{12})$ [1]) of 1.4. One hundred random orientations for the cubic material are considered. The RMS of the 100 FE results are plotted as red dots in (b) and the error bars show their standard deviation.

bars showing their standard deviation.

The theoretical prediction of the RMS backscattering amplitude of the inclusion with random crystallographic orientations can be calculated using Equation 3.2, where $\triangle C_{33}$ is replaced by $\sqrt{< \triangle C_{33}^2 >}$, which is the RMS difference between the 3333 elastic constant of the inclusion, averaged over all grain orientations, and that of the medium. The expression of $< \triangle C_{33}^2 >$ for a cubic material is given by [83].

$$< \triangle C_{33}^2 > = \frac{16(C_{11} - C_{12} - 2C_{44})^2}{525} \tag{3.3}$$

The theoretically predicted RMS backscattering amplitude is plotted as the blue curve in Figure 3.2b, from which good agreement between the FE and theoretical predictions can be seen. A relatively large standard deviation can be seen in the FE results, which shows that the crystallographic orientation of a grain has significant influence on its backscattering amplitude.

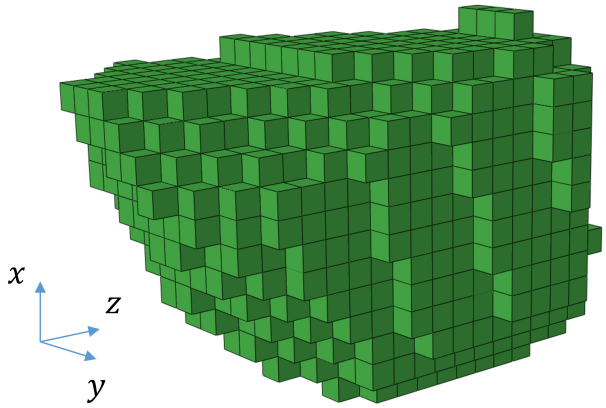


Figure 3.3: The irregular shaped inclusion modelled with uniform hexahedral elements with an edge length of 0.05 mm.

3.2.2 Irregular shaped inclusion

So far, the FE approach has been proved to be valid in predicting the scattering from a spherical inclusion. However, the shape of a real grain is usually far more irregular than a sphere. Therefore, we consider an inclusion with an irregular shape, which is more representative of a real grain.

In order to get an inclusion with a representative shape of a real grain, a FE model with an aggregate of grains, which will be referred to as a "multi-grain" model, is generated using 3D Voronoi tessellation, a mathematical method which uses 3D entities to fill a 3D space with no overlaps and no gaps [93]. This "multi-grain" model has the same size as the "single-grain" model and contains 28000 grains with an average linear dimension of 0.34 mm (the averaged grain volume is 0.125 mm^3). Structured meshes, which have been shown to perform well with sufficiently fine discretisation in modelling a grained material [16], are used here. The element size (element edge length) needs to meet two requirements, at least 10 elements per wavelength [94], and at least 10 elements per cubic root of the averaged grain volume [16]. From the model parameters given above, it can be seen that the element size adopted here is restricted by the latter requirement and therefore, it is set to be 0.05 mm. (As all the "multi-grain" models used in this paper have the same

mean grain size, the same element type and size will be adopted in their discretisations.) Using the same discretisation in the "multi-grain" model and the "single-grain" model enables a grain in the "multi-grain" model to be "moved" to the "single-grain" model to represent an inclusion.

Then a grain, of which the FE model is shown in Figure 3.3, is randomly picked from the "multi-grain" model. Its geometry is used to model the inclusion, replacing the spherical one, in the "single-grain" model. Similarly, we first consider the inclusion with an isotropic material and then a cubic material. The results are shown in Figure 3.4, where the $x-$axis shows the product of the wave number k and half of the average linear dimension of the grains in the "multi-grain" model, denoted by b (b is constant at 0.17 mm in Figure 3.4). A 4 MHz excitation is used in the FE simulations for the isotropic inclusion and two centre frequencies, 2 MHz and 4 MHz, are used in the FE simulations for the inclusion with cubic symmetry in order to cover a large range of kb. Good agreement between the FE and theoretical predictions can be seen for both the isotropic and cubic inclusions. Similar to Figure 3.2b, a large standard deviation can be seen in the FE results, showing the significant influence of the crystallographic orientation of a grain on its backscattering amplitude.

3.2.3 RMS backscattering amplitude of single random shaped inclusions

Up to now, it has been shown that the FE approach is valid for calculating the backscattering of a single grain with an isotropic or a cubic material. In this section, a further test will be carried out to assess whether it can give an accurate statistical prediction of the RMS backscattering amplitude of single random shaped inclusions.

The theoretical prediction of the RMS backscattering amplitude of single grains, which can be regarded as random shaped inclusions, can be written as [47, 48, 83]

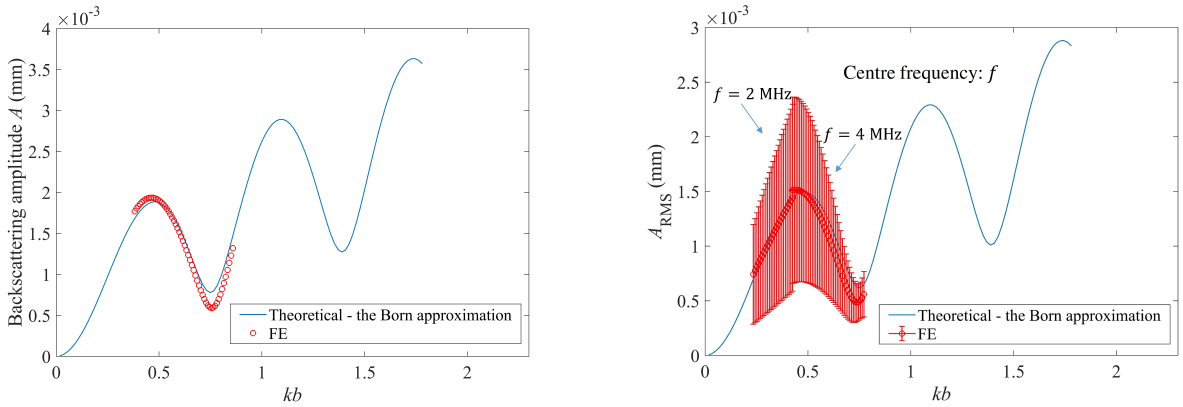


Figure 3.4: Comparison of FE and theoretical backscattering amplitudes of an irregular inclusion with (a) an isotropic material and (b) a cubic material with a Zener anisotropy factor of 1.4. One hundred random orientations for the cubic material are considered. The RMS of the 100 FE results are plotted as red dots in (b) and the error bars show their standard deviation. Two centre frequencies, 2 MHz and 4 MHz, are used in the FE simulations for the inclusion with cubic symmetry.

$$A_{\mathrm{RMS}} = \frac{\sqrt{\frac{\pi^2 f^3 <\Delta C_{33}^2>}{\rho^2 v^7} \int_0^\infty L\sin(\frac{4\pi f L}{v}) w(L)\mathrm{d}L}}{\sqrt{n_g}} \tag{3.4}$$

where n_{g} is the grain density; f is the frequency; ρ is the density; v is the Voigt averaged longitudinal velocity, for cubic symmetry which is given by

$$v = \sqrt{\frac{3C_{11} + 2C_{12} + 4C_{44}}{5\rho}} \tag{3.5}$$

$w(L)$ is the two-point correlation (TPC) function which shows the probability that two arbitrarily placed points a distance L apart in the specimen are located in the same grain. Here, $w(L)$ is obtained by fitting a 4-exponential series to the real correlation function obtained from the "multi-grain" model [42].

To predict the RMS backscattering amplitude with FE simulations, a number of inclusions which are representative of real grains are needed. The same "multi-grain" model, which is made from the same cubic material used in Section 3.2.1 and 3.2.2, with different

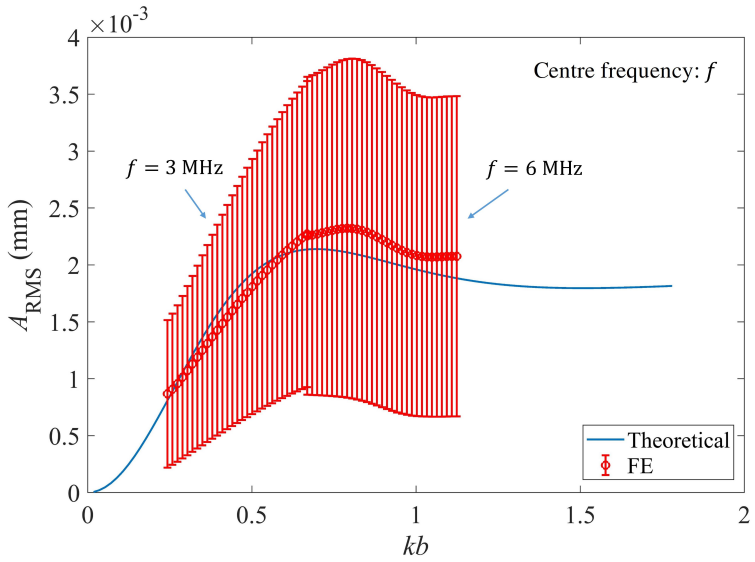


Figure 3.5: Comparison of FE and theoretical RMS backscattering amplitudes of single random shaped grains with a cubic material whose Zener anisotropy factor is 1.4. Five hundred random grains with random orientations for the cubic material are considered as the inclusion at the central axis in the "single-grain" model. The RMS of the 500 FE results are plotted as red dots and the error bars show their standard deviation. Two centre frequencies, 3 MHz and 6 MHz, are used in the FE simulations.

orientations to different grains, is used here to provide the geometry and material information for inclusion in the "single-grain" model. 500 grains are randomly picked from the "multi-grain" model. For each of them, the geometry and material information are used to define the inclusion, which is at the central axis in the "single-grain" model, as shown in Figure 3.1, and the backscattering amplitude from it is calculated.

Figure 3.5 shows the comparison of the FE and theoretical predictions, where the $x-$axis shows the product of the wave number k and half of the average linear dimension of the grains in the "multi-grain" model, denoted by b (b is constant at 0.17 mm in Figure 3.5). The FE predicted RMS backscattering amplitude is plotted as the red dots and their standard deviation is shown with the error bars. Two centre frequencies, 3 MHz and 6 MHz, are used in the FE simulations in order to cover a large range of kb, therefore there are two sections of the FE results. The theoretical prediction calculated using Equation 3.4 is plotted as the blue curve. Good agreement between the FE and theoretical predictions

shows the validity of the 3D FE approach in predicting the scattering response from single grains and therefore a strong potential to deal with the grain noise, which will be discussed in the following sections.

3.3 Prediction of grain noise measured with plane wave excitation and point receivers

In this section, the grain noise generated with plane wave excitation will be investigated. A theoretical model will be developed following the derivation of the ISM in [83] and the noise predicted by the model will be compared with that given by the 3D FE approach validated in the previous section.

We will start with the development of the theoretical model. The assumptions adopted during the derivation are:

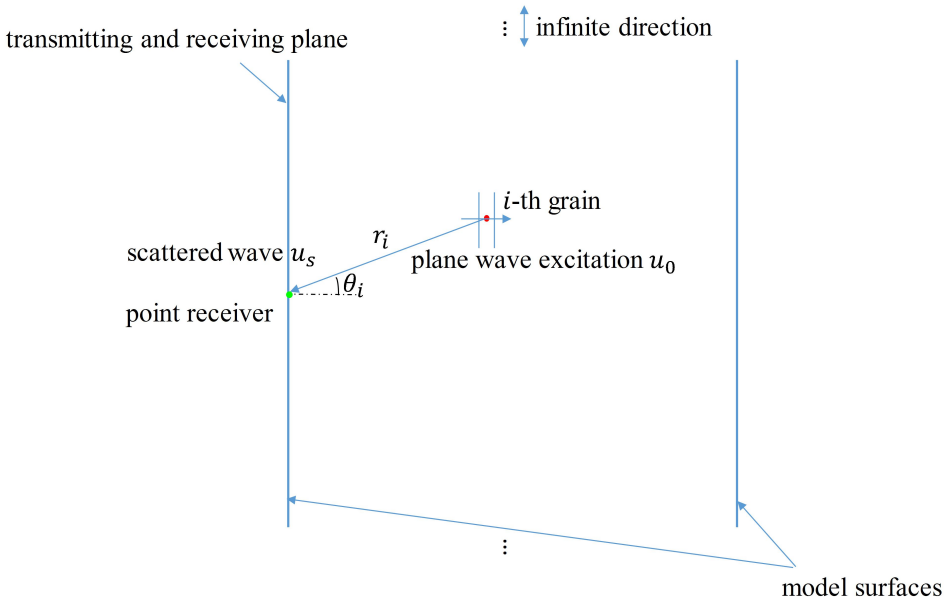


Figure 3.6: A schematic of a 2D section of the 3D theoretical model used for grain noise prediction with the plane wave configuration

1. Only longitudinal-to-longitudinal wave scattering is considered.

2. There is no multiple scattering phenomenon, i.e. the reflection from one grain is not affected by other grains.

3. Total grain noise is the incoherent sum of the reflections from single grains, i.e. the phases of the individual reflections are not correlated.

4. No attenuation is considered, which is a direct consequence of assumption 2 above that stipulates that the reflection from one grain is not affected by other grains. This is different from the ISM [83], which included attenuation in the derivation. However, in [83], a study on the effective attenuation was carried out and it was shown that the attenuation coefficient determined by the decay of grain noise is significantly less than that determined by coherent frontwall and backwall signals. This difference has also been reported in [95, 96], along with an idea that this difference is due to the sensitivity of the coherent wave echoes to deviations of the wavefronts from their initial simple shape. Therefore, it is not appropriate to use the coherent attenuation coefficient to describe the attenuation of the grain noise. Furthermore, in some cases shown in [83], the attenuation coefficients deduced by the depth dependence of the grain noise are close to zero, which indicates that it is reasonable to adopt this assumption in our theoretical model.

5. As the configuration with a plane wave excitation and point receivers is adopted, considering the duration of the excitation pulse, the reflections arriving at a given time instant are from the grains in between two paraboloid surfaces. Here for computational convenience, the surfaces are only approximated as hemispherical surfaces, i.e. the grains contributing to the grain noise at a given time instant are located in between two hemispherical surfaces. As a result of this approximation, the $N_{\mathrm{RMS}}(t)$ calculated in Equation 3.15 is actually independent of time t.

6. Only the normal component of the received displacement contributes to the received signal.

7. The directionality of the scattering from the grain is neglected.

Consider a 3D model with an infinite width. The points on one of the model surfaces, referred to as the transmitting and receiving plane in Figure 3.6, are used to transmit a plane wave excitation into the model (in the normal direction) and receive the reflected signals.

Assume all the transmitters are excited by a toneburst

$$u_0(t) = E(t)\mathrm{e}^{\mathrm{j}\omega t} \tag{3.6}$$

where $E(t)$ is the envelope function of the excitation signal, whose peak amplitude is unity, ω is the angular frequency and t is time.

Consider the reflection from a grain with an index of i. This grain is located at $(r_i, \theta_i, \varphi_i)$ in the spherical coordinate system. According to assumptions 6 and 7, the amplitude of the reflection from this grain received by one of the point receivers located at the origin can be written as

$$u_{\mathrm{s}}(t, r_i, \theta_i, \varphi_i) = \frac{A_i \cos(\theta_i) E(t - t_{0i})\mathrm{e}^{\mathrm{j}\omega(t-t_{0i})}}{r_i} \tag{3.7}$$

where $t_{0i} = 2r_i/v$, (according to assumption 5, where v is the longitudinal velocity), A_i is the L-L backscattering amplitude from the grain and the meanings of other symbols are shown in Figure 3.6. The cos function is introduced to account for the angle of incidence of the scattered wave at the location of the point receiver, as it is assumed that only the normal component of the received displacement contributes to the received signal.

For convenience, Equation 3.7 can be rewritten as

$$u_{\mathrm{s}}(t, r_i, \theta_i, \varphi_i) = B_i\mathrm{e}^{\mathrm{j}\omega(t-t_{0i})} \tag{3.8}$$

where

$$B_i = \frac{A_i \cos(\theta_i) E(t - t_{0i})}{r_i} \tag{3.9}$$

Under assumptions 2 and 3, the grain noise received by the point receiver at a given time instant is the sum of the reflections from individual grains arriving at the receiver at that time instant [83]:

$$u(t) = \sum_{i=1}^{m} u_{\mathrm{s}}(t, r_i, \theta_i, \varphi_i) \tag{3.10}$$

Compared with coherent averaging, incoherent averaging enables more information of the grain noise to be shown in the averaged signals, rather than cancelled out during the averaging. Therefore, here, instead of the mean of the received signals, the RMS of them will be used to quantify the grain noise level. As it is understood that the physical value of the reflection amplitude is the real part of its complex counterpart [83], the normalised RMS of the noise received by multiple point receivers is defined as:

$$N_{\mathrm{RMS}}(t) = \sqrt{< \mathrm{Re}^2(u(t)) >} \tag{3.11}$$

where <> denotes the average over all the point receivers on the transmitting and receiving plane.

According to [83]

$$< \mathrm{Re}^2(u(t)) >= \frac{1}{2} \sum_{i=1}^{m} < |B_i|^2 > \tag{3.12}$$

Substituting Equation 3.9 into 3.12 and replacing the sum over grains by an integral over the volume of the model,

$$< \mathrm{Re}^2(u(t)) >= \frac{1}{2} n_{\mathrm{g}} < |A_i|^2 > \int\int\int \frac{\cos^2(\theta) E^2(t - t_0)}{r^2} r^2 \sin(\theta) \mathrm{d}r \mathrm{d}\theta \mathrm{d}\varphi \tag{3.13}$$

where $t = 2r/v$.

According to assumption 5, the grains contributing to the grain noise at a given time

instant are located in between two hemispherical surfaces with radii of r_1 and r_2. This assumption is not accurate at a large reflection angle θ. However, due to assumption 6, the main contribution to the noise comes from the grains located at a relatively small reflection angle θ, which makes this simplification applicable. In this case, Equation 3.13 can be rewritten as

$$< \mathrm{Re}^2(u(t)) >= \frac{1}{2} n_\mathrm{g} < |A_i|^2 > \int_0^{2\pi} \mathrm{d}\varphi \int_0^{\frac{\pi}{2}} \cos^2(\theta)\sin(\theta)\mathrm{d}\theta \int_{r_1}^{r_2} E^2(t-t_0)\mathrm{d}r \tag{3.14}$$

Substituting Equation 3.14 into 3.11, $N_\mathrm{RMS}(t)$ can be expressed as

$$N_\mathrm{RMS}(t) = \sqrt{n_\mathrm{g}} A_\mathrm{RMS} \sqrt{\frac{\pi}{3} \int_{r_1}^{r_2} E^2(t-t_0)\mathrm{d}r} \tag{3.15}$$

where $A_\mathrm{RMS} = \sqrt{< |A_i|^2 >}$. The choice of time origin in Equation 3.15 is arbitrary. Here, it is chosen as the centre of the excitation signal, which means that $r_1 = v(t+\tau_1)/2$ and $r_2 = v(t+\tau_2)/2$, where τ is a time coordinate which is defined to be zero at the centre of the excitation signal and the envelope function of the excitation signal is non-zero between τ_1 and τ_2. In this case, Equation 3.15 can be expressed as

$$N_\mathrm{RMS}(t) = \sqrt{n_\mathrm{g}} A_\mathrm{RMS} \sqrt{\frac{v\pi}{6} \int_{\tau_1}^{\tau_2} E^2(\tau)\mathrm{d}\tau} \tag{3.16}$$

From Equation 3.16, it can be seen that without the attenuation, the noise RMS is independent of time. This is because, although the reflection from single grains at larger depth is smaller than their counterparts close to the receiver, the total number of grains increases with depth, which compensates for the decrease of the contribution from single grains.

Next, we will use the 3D FE approach to predict the normalised noise RMS and compare the results with the theoretical predictions. Another "multi-grain" model, which has dimensions of 13×13×50 mm^3 and contains 67600 grains (with an average linear dimension

of 0.34 mm), will be used in the FE simulations.

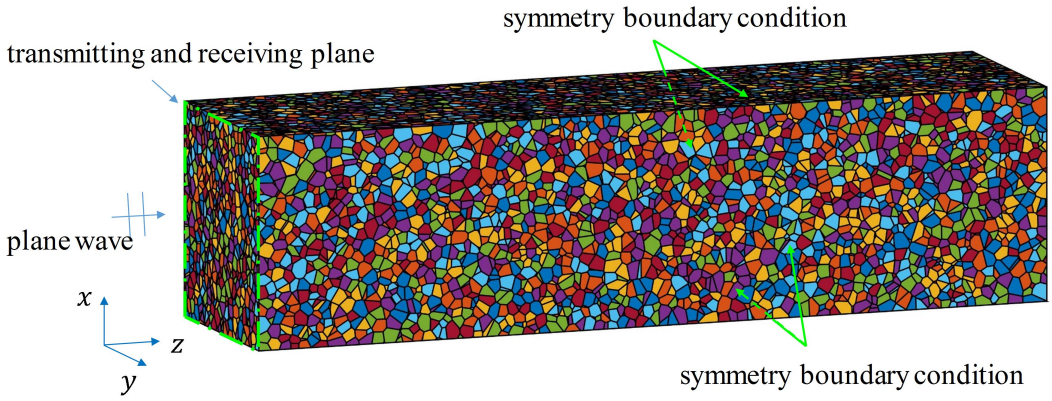


Figure 3.7: Multi-grain model ($13\times13\times50$ mm^3) with plane wave excitation. Point transmitters/receivers are uniformly distributed on the transmitting and receiving plane.

As shown in Figure 3.7, symmetry boundary conditions are used on all the model surfaces parallel to the z direction; one of the model surfaces on the $x-y$ plane is used as the transmitting plane where all the nodes are sending a 3-cycle Hann-windowed toneburst into the model (For a Hann window with the peak amplitude of 1, $\int_{\tau_1}^{\tau_2} E^2(\tau)\mathrm{d}\tau$ in Equation 3.16 is $3(\tau_2-\tau_1)/8$.), thereby producing a plane wave excitation propagating in the z direction; the same nodes are also used as receivers to measure the grain noise. For each case discussed in this section, 5 realisations with random crystallographic orientations of the model are run. In each realisation, an incoherent average (RMS) is taken over the signals received by all the receivers. Then the RMS of the 5 incoherently averaged signals will be used for discussion. This configuration represents a phase-insensitive measurement of the backscattered incoherent ultrasonic field [97].

Figure 3.8 shows the RMS signals under a 3 MHz excitation. Three cubic materials are used. They have the same density, Poisson's ratio and longitudinal wave speed calculated by the Voigt approximation, as 8000 kg/m^3, 0.3 and 6000 m/s respectively, but different degree of anisotropy, which is described by the Zener anisotropy factor A_z [1] here. The elastic constants of the materials are listed in Table 3.1, along with their Zener anisotropy

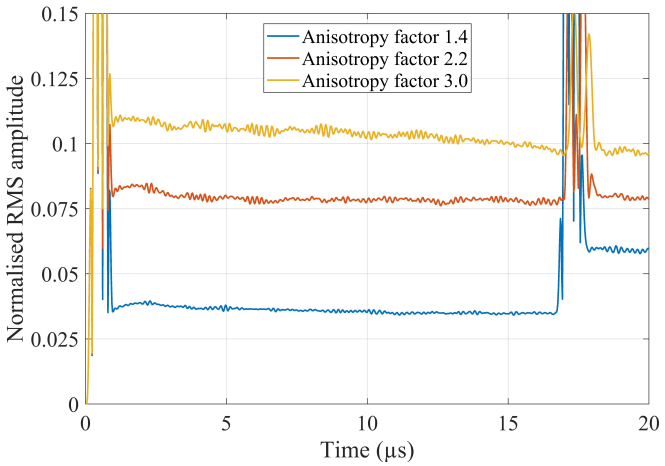


Figure 3.8: Spatial RMS of signals received by all the point receivers. The centre frequency of the excitation is 3 MHz. Three anisotropy factors, 1.4, 2.2 and 3.0, are discussed here. The frontwalls and backwalls are clipped where needed to highlight the grain noise.

factors, which will be used to refer to the materials. To highlight the grain noise, the frontwalls and backwalls are clipped in the figure. It can be seen that a higher noise level can be observed with a higher anisotropy factor. In addition, it is observed that with relatively low anisotropy factors, 1.4 and 2.2, the grain noise is independent of time, which is consistent with the theoretical solution, while with a relatively high anisotropy factor, 3.0, the noise decreases with time, which indicates that scattering induced attenuation occurs. The scattering induced attenuation is inherently a multiple scattering effect, as under the single scattering approximation, backscattering from any given scatterer is not affected by scattering from other scatterers. However, as mentioned earlier, the theoretical model ignores multiple scattering effects and predicts a noise level constant with time. Therefore, the FE results received in an early time range, 5 μs to 8 μs, which is less affected by the scattering induced attenuation, will be used later for comparison with the theoretical predictions.

Figure 3.9 shows the comparison of the FE and theoretically predicted noise RMS. The centre frequency used in the FE simulations is in the range of 0.6 MHz to 3 MHz. The blue, red and green curves show the predictions of cubic materials with anisotropy factors

Table 3.1: Elastic constants and anisotropy factors of the cubic materials discussed in this section

C_{11} (GPa)	C_{12} (GPa)	C_{44} (GPa)	$A_z = 2C_{44}/(C_{11} - C_{12})$ [1]
266.8	134.0	92.9	1.4
242.0	146.4	105.3	2.2
228.1	153.4	112.2	3.0

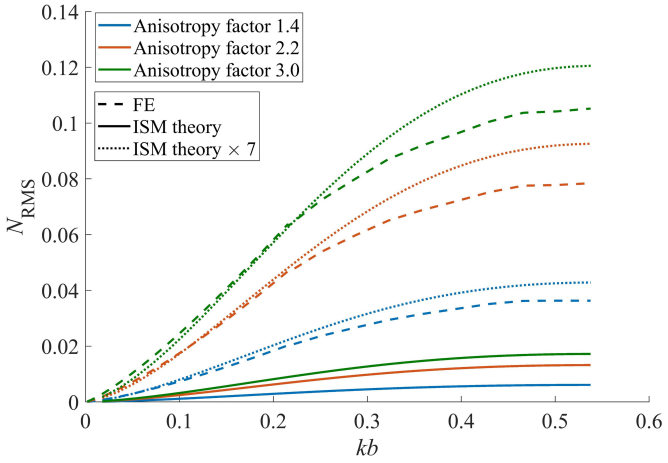


Figure 3.9: Comparison of FE, theoretical noise RMS and sevenfold theoretical noise RMS. The points on the dashed lines are the RMS noise (as shown in Figure 3.8) within a rectangular time window between 5 μs to 8 μs at different centre frequencies.

of 1.4, 2.2 and 3.0. The theoretical predictions are plotted as the solid curves and the FE results are shown as dashed curves. The points on the dashed lines are the RMS noise, as shown in Figure 3.8, within a rectangular time window between 5 μs to 8 μs (to reduce multiple scattering effects, as mentioned above) at different centre frequencies. From the figure, a big discrepancy between the two predictions can be seen and significantly higher backscattering is observed in the FE predictions. After multiplying the theoretical results by seven (the dotted curves), relatively good agreement can be seen, which shows that the FE results indicate a similar frequency dependence to the theoretical predictions.

A possible reason for this discrepancy is the contribution of shear waves, which is not accounted for in the theoretical model, but is implicitly captured in the FE simulations.

This contribution can be particularly strong when the shear wave reflection hits a point receiver at an oblique angle, as shown in Figure 3.10.

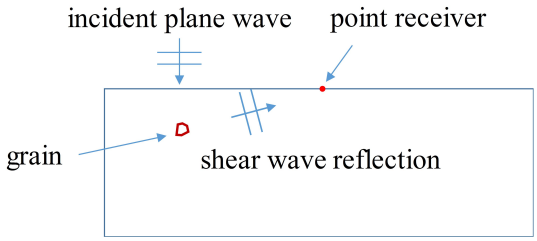


Figure 3.10: A schematic showing how a shear wave contributes to a signal received at a point receiver.

As can be inferred from Figure 3.10, the shear waves incident at oblique angles will be cancelled out quickly by taking a coherent average over the receiving plane, since the phase varies rapidly over the receiver face. Figure 3.11 shows the relationship between the noise RMS and the edge length of a square coherent averaging area (expressed in shear wavelengths and denoted by m). Each point on the blue curve is obtained in a similar way as that used to plot Figure 3.9, except that the spatial RMS is no longer taken over the signals received by the point receivers, but is taken over the signals obtained by coherently averaging the received signals on areas with dimensions of $m \times m$ wavelength square across the receiving plane. This simulates the signals received by a transducer with the same dimensions at different locations (i.e. different locations of a $m \times m$ wavelength square transducer are simulated and the RMS of the signals obtained at the different transducer locations is taken). It can be seen that the noise RMS drops rapidly after the edge length of the coherent averaging area reaches the shear wavelength. Some of this effect could be due to the cancellation of longitudinal waves. However, the oblique longitudinal waves are relatively weak as longitudinal scattering is stronger close to the normal direction, and the longitudinal waves are slower to cancel as their wavelength is longer than the shear wavelength. Therefore, the decrease of the noise RMS is mainly due to the cancellation of the shear waves, which indicates that oblique shear waves are a significant contributor to the noise seen by a point receiver and so explains the discrepancy between the FE results

and the analytical solution for L-L scattering with point receivers, shown in Figure 3.9. It can also be seen from Figure 3.11 that the noise RMS decreases with $1/m$, as indicated by the red line, rather than $1/\sqrt{m}$, which is because the coherent averaging is over a 2D surface rather than a line.

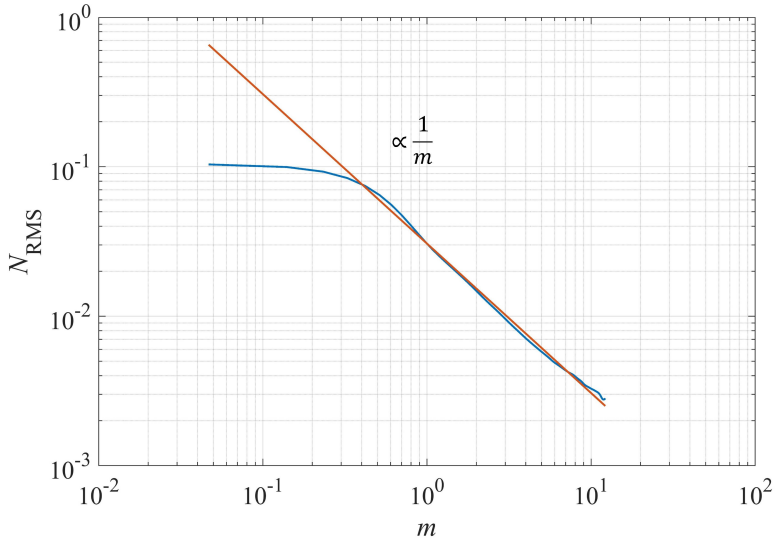


Figure 3.11: Noise RMS vs edge length of the square coherent averaging area (expressed in shear wavelengths and denoted by m). Each point on the blue curve is obtained in a similar way as that used to plot Figure 3.9, except that the spatial RMS is taken over the signals obtained by coherently averaging the signals on areas with dimensions of $m \times m$ wavelength square across the receiving plane. The red line is proportional to $1/m$.

To sum up, for a realistic transducer whose diameter is significantly larger than the shear wavelength, it is not expected to be a problem to predict the noise with a theoretical model ignoring the longitudinal-to-transverse (L-T) scattering, which will be cancelled out during the spatial averaging process over the transducer surface. This will be further discussed in the next section.

3.4 Prediction of grain noise measured with a finite transducer

Having discussed a basic configuration, in which the grain noise is excited by a plane wave and received by individual point receivers, in this section, we will investigate a more practical configuration with a finite contact transducer, and predict the grain noise generated and captured by it. This section will follow a similar procedure as that described in the last section. Firstly, a theoretical model predicting the grain noise level will be developed and then the result will be compared with that obtained by FE, where the contribution of shear waves and multiple scattering will be discussed.

We will start with a brief introduction of how to establish the theoretical model using a similar procedure to that used in [44]. During the derivation, all the assumptions mentioned in the last section, except assumption 5, are adopted and it is also assumed that the grains are small compared to the beam diameter, in which case, the excitation incident on each grain can be regarded as a quasi-plane wave.

In [44], Thompson and Gray's model [45], which was developed for rigid piston transducers, was used to calculate the reflection coefficients from single grains. According to [98], this model can be used without any modification for apodized transducers if the apodization is the same in transmission and reception, which is the case that we consider in this section. Therefore, the normalised change of the displacement received by an apodized transducer induced by a grain located at (x_i, y_i, z_i) can be expressed as

$$\delta\Gamma_s(\omega, x_i, y_i, z_i) = \frac{2V^2(\omega, x_i, y_i, z_i)}{V_0^2} \frac{A_i(\omega)}{\mathrm{j}k(\omega)a^2} \tag{3.17}$$

where a, ρ, v, A_i, k denote transducer radius, medium density, longitudinal wave speed, backscattering amplitude of the grain and wave number. V is the peak particle velocity at the location of the grain. V_0 is the peak velocity amplitude at the centre of the transducer.

Assume the transducer is excited by a toneburst $S_0(t) = E(t)e^{j\omega_0 t}$. The peak amplitude of $E(t)$ is unity and the Fourier transform of $S_0(t)$ is denoted by $U_0(\omega)$. The reflection signal in the frequency domain can be expressed as

$$\delta U_s(\omega, x_i, y_i, z_i) = \delta \Gamma_s(\omega, x_i, y_i, z_i) U_0(\omega) \tag{3.18}$$

In the time domain, it is denoted by $\delta S_s(t + t_{0i}, x_i, y_i, z_i)$, where $t_{0i} = 2z_i/v$. If we replace $t + t_{0i}$ with t and collect all the constants and functions which are slowly varying with ω into a term H and evaluated at $\omega = \omega_0$, δS_s can be written as

$$\delta S_s(t, x_i, y_i, z_i) = H(\omega_0, x_i, y_i, z_i)\frac{1}{2\pi}\int_{-\infty}^{\infty} U_0(\omega)e^{j\omega t}d\omega = H(\omega_0, x_i, y_i, z_i)E(t - t_{0i})e^{j\omega_0(t-t_{0i})} \tag{3.19}$$

where

$$H(\omega_0, x_i, y_i, z_i) = \frac{2V^2(\omega_0, x_i, y_i, z_i)}{V_0^2}\frac{A_i(\omega_0)}{jk(\omega_0)a^2} \tag{3.20}$$

It is assumed that the total noise, $W(t)$, is an incoherent sum of reflections from individual grains, expressed as

$$W(t) = \sum_{i=1}^{m} \delta S_s(t, x_i, y_i, z_i) \tag{3.21}$$

The normalised noise RMS over multiple transducer positions is defined in the same way as in the last section

$$N_{\mathrm{RMS}}(t) = \sqrt{< [\mathrm{Re}(W(t))]^2 >} \tag{3.22}$$

According to [83], the term in the square root sign in Equation 3.22 can be expressed as

$$< [\mathrm{Re}(W(t))]^2 >= \frac{1}{2}\sum_{i=1}^{m} < |B_i|^2 > \tag{3.23}$$

where

$$|B_i| = |H(\omega_0, x_i, y_i, z_i)E(t - t_{0i})| \tag{3.24}$$

Substituting equations 3.23 and 3.24 into Equation 3.22 and replacing the sum over grains by an integral over the volume containing the grains, the normalised RMS noise level is given by

$$N_{\mathrm{RMS}}(t) = \sqrt{2n_g}\frac{A_{\mathrm{RMS}}(\omega_0)}{V_0^2 k(\omega_0)a^2}\sqrt{\int\int\int |V^4(\omega_0, x, y, z)|E^2(t - t_0)\mathrm{d}x\mathrm{d}y\mathrm{d}z} \tag{3.25}$$

It is assumed that the grains contributing to the noise at a given time instant are located in between two depths z_1 and z_2. As mentioned in the last section, the time origin is chosen as the centre of the excitation signal, therefore, $z_1 = v(t + \tau_1)/2$ and $z_2 = v(t + \tau_2)/2$, where τ is a time coordinate which is zero at the centre of the excitation signal. Then Equation 3.25 can be rewritten as

$$N_{\mathrm{RMS}}(t) = \sqrt{n_g v}\frac{A_{\mathrm{RMS}}(\omega_0)}{V_0^2 k(\omega_0)a^2}\sqrt{\int_{\tau_1}^{\tau_2} G(\omega_0, \frac{v(t + \tau)}{2})E^2(\tau)\mathrm{d}\tau} \tag{3.26}$$

where

$$G(\omega_0, \frac{v(t + \tau)}{2}) = \int\int |V^4(\omega_0, x, y, \frac{v(t + \tau)}{2})|\mathrm{d}x\mathrm{d}y \tag{3.27}$$

The $V(\omega_0, x, y, z)$ required in Equation 3.27 can be approximated by a Gaussian model or a Gauss-Hermite model [83], or obtained by a FE simulation, as discussed in the following example.

Next, an example case will be given to predict the grain noise with the theoretical model developed above and the FE approach. A focused contact transducer, which has a radius of 5 mm and an actual focal length of 6 mm, is used, exciting the testpiece with a 3-cycle Hann-windowed toneburst, of which the centre frequency is 4 MHz. The amplitude distribution of the excitation across the transducer surface follows a 2D Hann-window.

The cubic materials listed in Table 3.1 will be used.

As a comparison of the theoretical and FE predictions will be carried out, the peak amplitude of the velocity excitation at the centre of the transducer (V_0 in Equation 3.26) and the velocity field ($V(\omega_0, x, y, z)$ in Equation 3.27) used for theoretical noise calculation will be measured with FE to ensure that the same excitation and wave field are considered.

The multi-grain model used in the FE simulations is shown in Figure 3.12. The white circle outlines the focused transducer, where focusing is achieved through adding time delays to the excitation and reception of individual nodes. Symmetry boundary conditions are used on all the surfaces normal to the transducer plane. For each case discussed in this section, 50 realisations with random crystallographic orientations of the model are run. For the sake of computational efficiency, the tessellation of the grain structure is kept the same. In each realisation, a coherent average over the transducer surface is taken, simulating a signal received by the transducer at one position. Then the RMS signal of the 50 averaged signals is used for comparison with the theoretical prediction.

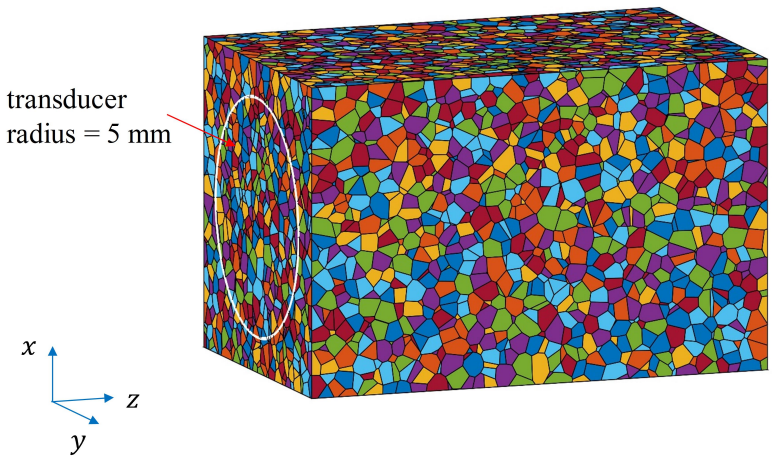


Figure 3.12: "Multi-grain" model ($13 \times 13 \times 20$ mm^3). A 5 mm radius focused transducer is outlined by the white circle. Focusing is achieved through adding time delays to the excitation and reception of individual nodes. A Hann-window is applied on the excitation amplitude over the plane of the transducer to remove surface waves.

The FE predicted grain noise is plotted as the blue curves in Figure 3.13, along with the theoretical predictions, shown as the red curves. Figure 3.13a, where the anisotropy factor is 1.4, shows very good agreement. However, relatively large discrepancies can be seen in Figures 3.13b and 3.13c with anisotropy factors of 2.2 and 3.0, where the peaks caused by focusing in the FE predictions appear at earlier times than those in the theoretical curves. This is because the peak of the noise predicted by FE shifts to an earlier time with a higher anisotropy factor, while that given by the ISM theory is independent of anisotropy factor. The discrepancies of noise levels are dependent on time (or depth), indicating that this is caused by the scattering induced attenuation, which is not accounted for in the theoretical model.

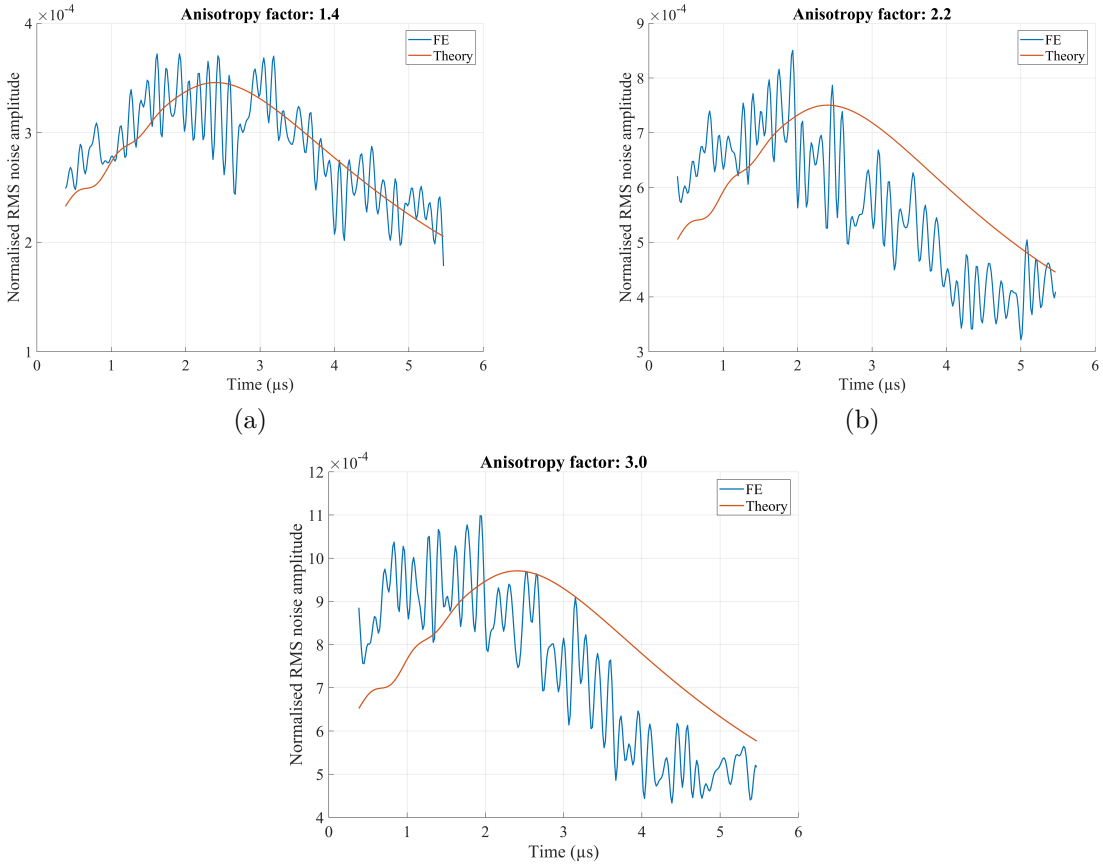


Figure 3.13: Comparison of FE and theoretical grain noise with anisotropy factors of (a) 1.4, (b) 2.2 and (c) 3.0. Attenuation of noise is not taken into account in the theoretical theory.

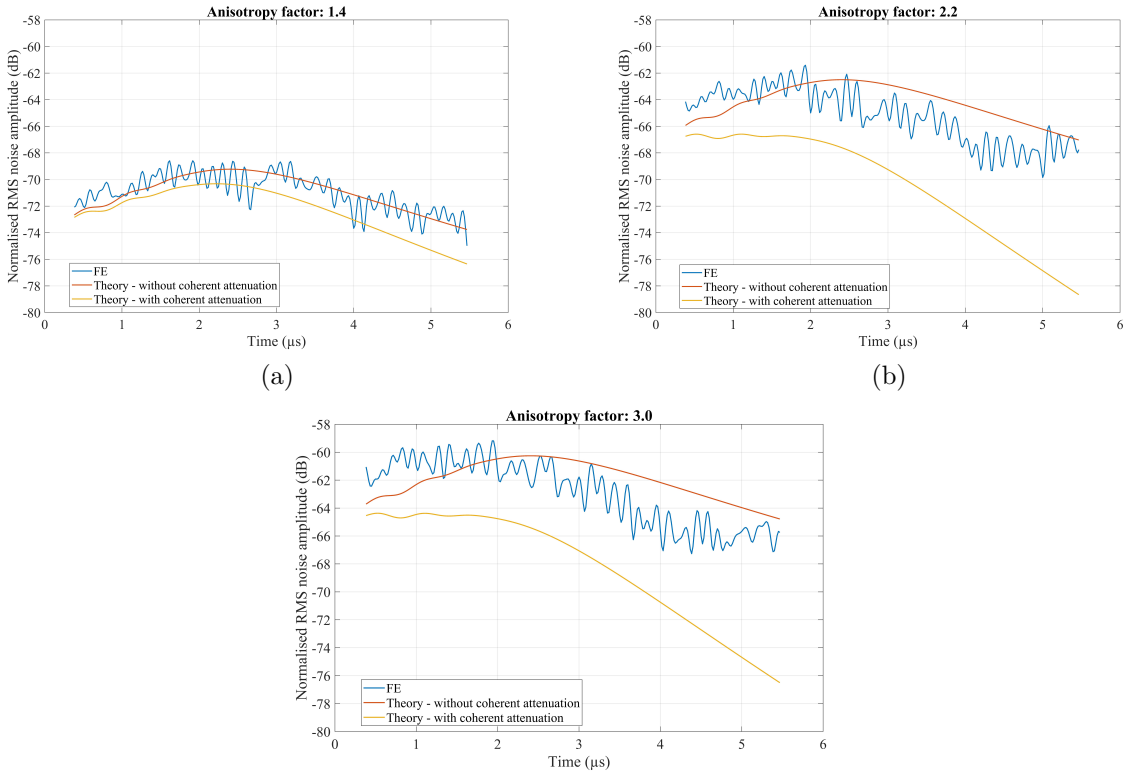


Figure 3.14: Comparison of theoretical grain noise with and without coherent attenuation and FE results. The anisotropy factors are (a) 1.4, (b) 2.2 and (c) 3.0 respectively.

To test if the scattering induced attenuation is the reason for the discrepancies, an attenuation term, which is deduced by comparing the amplitude of the average of the backwall reflection with that of the excitation obtained in the last section, will be added to the theoretical solution. The unattenuated and attenuated theoretical predictions are compared with the FE results in Figure 3.14. It can be seen that the attenuated theoretical predictions have more similar shapes to the FE results than the unattenuated solutions, which indicates the discrepancies could be due to the attenuation. However, it can also be seen that the attenuated theoretical solutions are significantly lower than the FE results. This means that the scattering induced attenuation has a more significant influence on the coherent waves than the grain noise, so the attenuation coefficient deduced using the coherent waves is much higher than that deduced by the incoherent noise, which has been

reported in [83, 95, 96].

In this section, the grain noise excited and captured by a finite contact transducer has been predicted with the adapted theoretical model and the FE approach, the contributions of shear waves and multiple scattering being included in the FE analysis but not in the analytical solution. From the results shown in Figure 3.13a, good agreement between the unattenuated theoretical prediction and the FE result can be seen, which implies that the contribution of shear waves is negligible, as expected due to the spatial averaging over the transducer surface, and the multiple scattering has little influence on the grain noise level, as the anisotropy factor is relatively low and the backscattering is weak. However, with relatively high anisotropy factors, discrepancies are observed in Figure 3.13b and 3.13c, indicating the occurrence of the multiple scattering, in which case the theoretical model cannot give an accurate noise prediction, but does still provide a rough estimate of the noise level. Therefore, when an accurate noise prediction is required in highly scattering regimes, the FE approach is more appropriate as it can solve the full-physics problem including multiple scattering. However, if only a rough estimation of the grain noise level is needed or if weakly scattering problems are to be solved, the theoretical model is more desirable as it can give a reasonable estimate very efficiently, as shown in Figure 3.13.

3.5 Summary of the chapter

Theories describing the grain noise behaviour have been widely researched. Most of them are based on a single scattering assumption and only consider longitudinal-to-longitudinal wave scattering, which limit their application. In this chapter, an alternative approach, the 3D FE method, has been presented to study the ultrasonic backscattering of polycrystalline materials. This method can solve the full-physics scattering problem including multiple scattering, which enables it to be used in both weakly and highly scattering regimes. In addition, it can implicitly capture the longitudinal-to-transverse scattering

which is ignored in the theories.

The validation of the 3D FE approach has been conducted with a "single-grain" model. By comparing the FE results with the theoretical predictions, it has been shown that the FE approach is capable of giving an accurate prediction of the scattering amplitude from a single grain.

The grain noise generated with a transmit-receive configuration of a plane wave excitation and point receivers has been discussed. When compared with the theoretical result, the FE predicted noise is significantly higher, which has been demonstrated to be largely due to the contribution of shear waves which is not accounted for in the theoretical model. As the shear wave components can be cancelled out quickly by taking a coherent average over the receiving plane, it is expected to be no problem to predict the grain noise captured by a finite transducer with a theoretical model ignoring the shear waves, as the transducer generates a spatial average.

The grain noise excited and received by a finite transducer has been predicted. Without considering the attenuation, good agreement between the theoretical and FE predictions can be seen with a relatively low anisotropy factor, 1.4, while discrepancies are observed with anisotropy factors 2.2 and 3.0, which indicates the occurrence of multiple scattering. When the coherent attenuation coefficient is applied to the theoretical model, the theoretical predictions have more similar shapes to the FE results, indicating that the discrepancies could be due to the scattering induced attenuation. However, significantly lower noise is observed in the attenuated theoretical predictions than that in the FE results for all the anisotropy factors, which implies the attenuation coefficient of the grain noise is much lower than that of the coherent waves.

To sum up, the FE approach has been validated to be a powerful tool to predict the grain noise. However, the high computational costs it requires (It takes around 12 minutes to run one realisation discussed in Section 3.4 using 8x Nvidia K80 dual cards.) can limit its application in practice. Furthermore, as shown in Figure 3.13, although there

are discrepancies between the unattenuated theoretical predictions and the FE results, the unattenuated theoretical model can give a rough estimation of the grain noise very efficiently. Therefore, when a high accuracy is not required, there is no doubt that the theoretical model is an efficient approach to investigate the ultrasound backscattering. Thus, in the following chapter which presents a broad approach to the development of an optimal monitoring system, the theoretical model ignoring the attenuation will be used to predict the grain noise.

Chapter 4 Optimal permanently installed monitoring system for polycrystalline materials

4.1 Introduction

As mentioned in the previous chapters, ultrasonic monitoring of coarse grained polycrystalline materials is often restricted by a low SNR due to grain boundary scattering. In Chapter 2, some widely researched signal processing techniques used to enhance the SNR have been reviewed and baseline subtraction, along with compensation methods, has been used to suppress the grain noise. By subtracting a compensated signal from the corresponding baseline, a relatively modest improvement in the SNR is achieved. However, this method is sensitive to the sample surface and grain structure changes and has a significant requirement of data storage, which limit its application in practice.

In addition to using post processing methods, there are other strategies which can be used in a monitoring system to enhance the SNR, such as the multizone technique [75–77]. Multizone uses multiple focused transducers focusing at different depths to scan a sample. This enables most of the material to be covered in the focal zone, so that good SNRs can be achieved throughout the sample. However, scanning is not practical for a permanently installed monitoring system, where transducers are located at fixed positions. In this case, focusing can only improve the SNR near the fixed focal zones, leaving low SNRs outside of the focal areas. As a high sensitivity is required throughout the monitored area, focusing is less effective for detection improvement. Furthermore, apart from the SNR,

the cost is also an important aspect that needs to be considered in a permanently installed monitoring system. This means that a transducer covering a larger depth or area is more desirable, so small area coverage from a single transducer position also makes focused transducers less desirable than unfocused transducers.

As the transducer frequency and diameter dependence of the signal and the grain noise differ, an opportunity exists to determine the frequency and diameter of the unfocused transducers by solving an optimisation problem. This optimisation problem usually gives a criterion related to the cost of the system as the target and requires a minimum value of SNR in the inspection volume of a single transducer. Another requirement often imposed is the maximum radial variation of signal in the inspection volume, because signals from defects along a radial line appear at similar times and it is desirable for a given sized defect at any radial location at a given depth to give a similar reflection amplitude. As noise is constant in the radial direction, this can be regarded as a requirement of the maximum radial variation of SNR. Axial variation of signal can be compensated with Distance Amplitude Correction (DAC) [99] which is typically applied, so it is acceptable. In this chapter, a procedure of solving this problem and finding the optimum frequency and diameter with a combined analytical-and-numerical method is presented.

This chapter begins by introducing an approach to produce a SNR map. The grain noise is predicted using the theoretical solution derived in Chapter 3. The signals from a flat-bottom hole, representing a calibration defect, at one position are computed using finite element simulations. Overall signal to noise maps for flat-bottom holes at different locations are produced by scaling the signals by squared particle velocity and scattering induced attenuation. This chapter then investigates how various factors affect the SNR value and distribution. Two possible optimisation criteria are given and two representative examples showing how to find the optimum transducer parameters and placement under each criterion are discussed at the end of this chapter.

4.2 SNR map generation

To solve the optimisation problem, it is essential to have a good knowledge of the SNR map produced by a single transducer. Each point in the SNR map shows the ratio of the peak amplitude of the reflection from a flat-bottom hole at that position to the RMS grain noise level received at the same time. A theoretical solution of SNR has been developed in [83], where the SNR is independent of attenuation, as it is assumed that the effective attenuation coefficients are identical for the signal and backscattering noise. In this section, we will introduce a combined analytical-and-numerical approach to generate a 3D SNR map, where the attenuation is ignored in the noise calculation but considered in the signal prediction, which is different from the theoretical model [83]. Next, we will introduce the procedure of generating a SNR map, including the prediction of signal reflection, particle velocity field, scattering induced attenuation and grain noise.

4.2.1 Signal reflection prediction

A flat-bottom hole is used as a calibration defect and the reflection from it is predicted with POGO [40]. A schematic of a 3D model with an on-axis flat-bottom hole is shown in Figure 4.1. The model is meshed with uniform hexahedral elements and the flat-bottom hole, shown as the long-dashed cylinder in the figure, is modelled by deleting the elements whose centre points are inside of the cylinder. This method significantly speeds up the modelling and meshing process at the cost of the arising staircase in the modelling of the hole. The error caused by the staircase effect can be suppressed or minimised by adopting a large ratio of the hole diameter to element size (element edge length) [92]. Therefore, with a given defect size, the element size should be small enough to minimise the staircase effect. However, the element size is also restricted by computational resources. This limits the minimum ratio of the hole diameter to element size in this study to be 8, in which case the error caused by the staircase effect still exists but is acceptable [92]. Details of

Table 4.1: Model and mesh sizes used for defect reflection prediction at different frequencies

Frequency (MHz)	0.1	0.45, 0.75	1.0 to 2.2
Model dimensions $x \times y \times z$ (mm^3)	$190 \times 190 \times 150$	$100 \times 100 \times 100$	$40 \times 40 \times 40$
Element edge length (mm)	0.25	0.20	0.10

the model and mesh sizes used to predict defect reflections can be found in Table 4.1.

The red dots in the solid circle in Figure 4.1 show the nodes which are used to transmit and receive signals in the $z-$direction, simulating a contact unfocused transducer in a pulse-echo configuration. The received signals are then averaged coherently to produce a predicted signal. Restricted by the model size, the defect reflection is often overlapped with boundary reflections. To remove the reflections unrelated to the defect, a reference signal collected in the absence of the defect is subtracted from the predicted signal and a clean reflection from the defect can be obtained.

The model is assigned an isotropic material whose properties are the Voigt averages of the elastic constants of a cubic material, so the reflection signal is unaffected by scattering. The scattering induced attenuation will be considered later in Section 4.2.3 by adding an attenuation term.

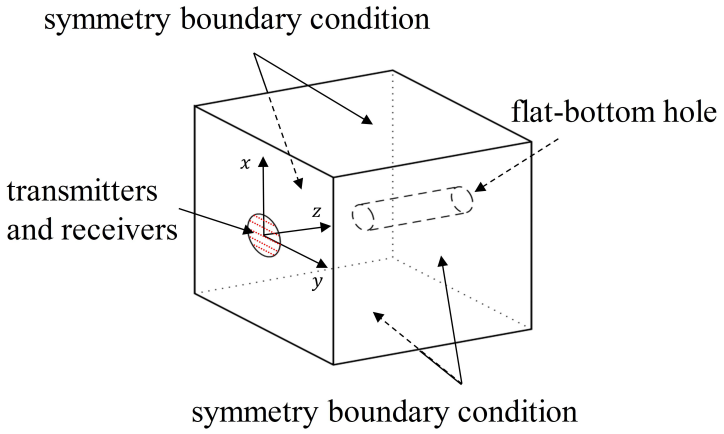


Figure 4.1: A schematic of a 3D isotropic model with an on-axis flat-bottom hole used for defect reflection prediction

To generate a SNR map, the reflection amplitudes from holes at all the positions are needed. It is too computationally expensive to predict every point in the map using FE. However, if the size of the hole is small compared to the wavelength, Equation 3.17 which shows the reflection from a small grain can also be used to give an approximation of the reflection from the hole. In this case, the reflection amplitude is proportional to the squared particle velocity at the defect location, i.e. $U(x_1, y_1, z_1) \propto V^2(x_1, y_1, z_1)$, where $U(x_1, y_1, z_1)$ is the reflection amplitude from a defect at (x_1, y_1, z_1) and $V(x_1, y_1, z_1)$ is the particle velocity at (x_1, y_1, z_1). Therefore, the reflection amplitude $U(x, y, z)$ from a hole with the same radius at any position (x, y, z) can be estimated as $U(x_1, y_1, z_1) \times \frac{V^2(x,y,z)}{V^2(x_1,y_1,z_1)}$, where $V(x, y, z)$ is the particle velocity at (x, y, z). This approximation will be adopted in this study for SNR map generation. As it will break down when the defect size is a significant fraction of the wavelength, the results obtained using the procedure should be regarded as first estimates to be refined later with a better defect response model.

4.2.2 Particle velocity field and Gaussian beam fitting

The particle velocity field can be obtained using the same 3D model but without the defect. However, because the transducer is axisymmetric, the velocity field produced by it can be predicted with an ABAQUS 2D axisymmetric model, shown in Figure 4.2. Compared to the 3D simulation, the 2D axisymmetric analysis enables a larger model with finer mesh to be solved in a shorter time, so it is adopted here.

The blue long-dashed line at the top edge shows the axis of symmetry. The red dots on the left edge represent the transmitters exciting the model in the $z-$direction. The receivers are uniformly distributed in the model to measure the displacement signals and by taking the derivative with respect to time, the velocity signals can be obtained. The velocity field is then generated by taking the peak amplitudes of the velocity signals.

Relatively large models are used to minimize the boundary effect on the velocity field. As the affected area is larger with a lower frequency, larger models are used in the lower

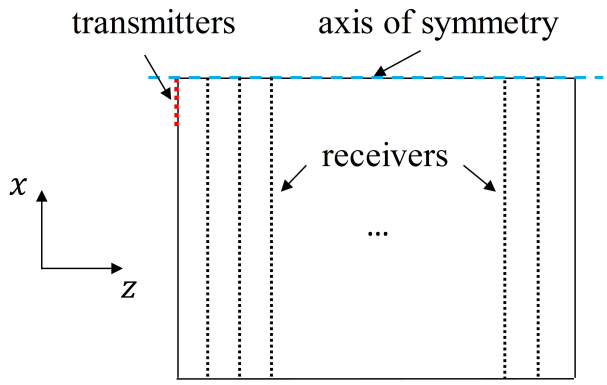


Figure 4.2: A schematic of an ABAQUS 2D axisymmetric model with uniformly distributed point receivers used to predict velocity field

Table 4.2: Model and mesh sizes used for velocity field prediction at different frequencies

Frequency (MHz)	0.1	0.45 to 2.2
Model dimensions $x \times z$ (mm^2)	500×600	100×120
Mesh edge length (mm)	0.25	0.05

frequency cases. Details of the model and mesh sizes (uniform quadrilateral element) used for velocity field prediction can be found in Table 4.2.

A 3D velocity field with uniformly distributed data points can be generated by either interpolating the obtained 2D field or using a 3D Gaussian beam model which gives the best fit to the 2D field. Compared to interpolating the 2D results, using a Gaussian beam enables a larger velocity field with higher resolution to be obtained with good accuracy. Therefore, the 3D velocity field is estimated by a Gaussian beam model obtained with a two-parameter (beam waist radius and position) fit and will be used in both the scaling process and noise calculation. It would also be possible to do a purely analytical solution, as discussed later.

4.2.3 Scattering induced attenuation

So far, attenuation has not been accounted for in the calculation. In this study, the attenuation due to viscous losses in the thermoplastic host is not considered. However, as

the scattering induced attenuation has a significant impact on coherent signals, it needs to be taken into account when generating a SNR map.

A 3D grained model, shown in Figure 4.3, is used to predict the coherent attenuation coefficient. The model with dimensions of $13 \times 13 \times 50$ mm^3 contains 204×10^6 degrees of freedom and 67600 grains with an average linear dimension of 0.34 mm. As in Chapter 3, uniform elements are used and the element size meets the requirements mentioned in Section 3.2.2.

The cubic material whose Voigt averages are used in Section 4.2.1 and 4.2.2 is assigned to the model, with different orientations to different grains. Symmetry boundary conditions are used on the model surfaces parallel to the $z-$axis. All the nodes on one of the model surfaces in the $x-y$ plane, shown as the red dots in Figure 4.3, are used as transmitters and receivers, with which a plane wave propagating in the $z-$direction is effectively generated. The coherent attenuation coefficient α can be obtained by comparing the amplitude of the average of the backwall reflection with that of the excitation. Since a significant number of grains are considered in this model, one realisation is expected to be enough to get an accurate prediction of the attenuation coefficient, although it is ideal to run multiple realisations to gather more statistics.

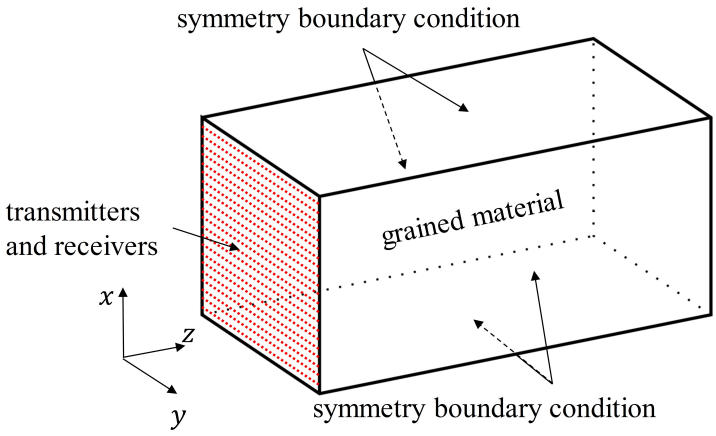


Figure 4.3: A schematic of the 3D grained model used for attenuation prediction

The attenuation coefficient is then used to estimate an attenuated reflection amplitude

received by a finite transducer. If we assume the modelled transducer is centred at the origin, the attenuated reflection amplitude $U_{\mathrm{a}}(x_1, y_1, z_1)$ from a defect at (x_1, y_1, z_1) is approximated by $U(x_1, y_1, z_1) \times \mathrm{e}^{-2\alpha z_1}$, where $U(x_1, y_1, z_1)$ is the unattenuated reflection amplitude from the defect. This approximation gives a good estimation when the defect is close to the centre line of the beam. In this study, due to the requirement of the maximum radial variation of the signal, the area of interest is relatively close to the central axis, so this approximation is applicable.

To sum up, the reflection amplitude from a defect at any position (x, y, z) can be estimated as:

$$U_{\mathrm{a}}(x, y, z) = U(x_1, y_1, z_1) \times \frac{V^2(x, y, z)}{V^2(x_1, y_1, z_1)} \times \mathrm{e}^{-2\alpha z} \tag{4.1}$$

where α is the coherent attenuation coefficient, $U(x_1, y_1, z_1)$ is the unattenuated reflection amplitude from a defect at (x_1, y_1, z_1), $V(x, y, z)$ and $V(x_1, y_1, z_1)$ are the particle velocities at (x, y, z) and (x_1, y_1, z_1) respectively. Using this equation, a 3D signal map can be produced.

4.2.4 Grain noise calculation and SNR map generation

Equation 3.25 gives a relationship between the RMS noise level and the depth where the grains contributing to the noise are located. Using this equation, a 1D noise map along the $z-$axis can be obtained, where the velocity field is generated by the fitted Gaussian beam. As mentioned in Chapter 3, the incoherent backscattering is much less affected by scattering induced attenuation than the coherent defect signal. Therefore, scattering induced attenuation is only considered in the defect reflection prediction, but not in the noise calculation, which is different from Margetan's model [44], as discussed in Chapter 3.

By dividing the signal map with the noise map, a SNR map is generated. This SNR map generation approach involves theoretical calculation, 2D ABAQUS axisymmetric

and 3D POGO simulations, which makes it less easy to use. Initially, we tried to solve this problem with a 3D FE analysis. However, during the study, it was found that a pure 3D FE approach is too computationally expensive, and the analytical solution of noise shows a good match with the FE result. Therefore, the analytical solution is used for noise calculation instead of the FE simulation and the signal map is estimated via a scaling process. Compared to a pure FE approach, this combined analytical-and-numerical approach can generate a valid SNR map with less computational cost, although the procedure is a little complicated. An opportunity exists to solve this optimisation problem analytically, which is beyond the scope of this thesis and can be pursued in the future.

4.3 Influence factors of SNR

The SNR is determined by a combination of factors, including defect characteristics, material properties, excitation and transducer parameters. More specifically, defect type and size strongly affect the signal amplitude; grain size and anisotropy factor significantly influence the noise and attenuation; excitation type and duration determine the grains and their weights contributing to the noise at a given time instant; transducer frequency and diameter both have a substantial impact on the signal and noise, and transducer frequency also affects the attenuation. As the SNR is a function of so many variables, it will be difficult to understand the result of the optimisation problem without a good understanding of how these factors affect the SNR.

In this section, taking a flat-bottom hole as a calibration defect, the SNR dependence on the various factors (except the defect type) will be investigated. It is desirable that SNR maps can be used to show the effects directly. However, limited by computational resources, the effects of excitation parameters, which can be easily explained by the theory introduced in Chapter 3, and the effects of grain size, the discussion of which requires

huge computational costs to generate SNR maps, will be investigated only with theories. It should be recalled that these maps are first estimates and are liable to be less accurate when the defect size to wavelength ratio increases beyond unity.

4.3.1 Effects of excitation parameters

Equation 3.25 shows that the noise can be regarded as a weighted sum of the reflections from grains. The envelope function of the excitation determines the number and weights of the grains contributing to the noise at a given time instant. If the excitation is longer, more grains are involved and if the excitation envelope is more like a square wave, the average weight of the grains is greater. In both cases, the noise increases, thereby decreasing the SNR. Therefore, in practice, to reduce the noise, a short excitation is usually desirable. In this chapter, a relatively short excitation, a 3-cycle Hann-windowed toneburst will be used.

4.3.2 Effects of grain size

Compared to the excitation parameters, the effects of grain size on SNR is more complicated, as it affects not only the noise, but also the scattering induced attenuation. In Chapter 3, to get an accurate noise prediction, a weighted sum of four exponentials is used to fit the TPC function of the model, which is more time consuming than a one-exponential fit. As the noise dependence on grain size is independent of the fit method of the TPC function, here it is fitted with one exponential, with which the FOM can be expressed as [83]:

$$\mathrm{FOM} = \left(\frac{8\pi^3 f^4 < (\triangle C_{33})^2 >}{\rho^2 v^8} \frac{b^3}{(1 + \frac{16\pi^2 f^2 b^2}{v^2})^2}\right)^{\frac{1}{2}} \tag{4.2}$$

where $v = (\frac{3C_{11}+2C_{12}+4C_{44}}{5\rho})^{\frac{1}{2}}$, $< (\triangle C_{33})^2 >= \frac{16(C_{11}-C_{12}-2C_{44})^2}{525}$, f is frequency, ρ is density, b is half of the average linear dimension of grains, C_{11}, C_{12}, C_{44} are elastic constants for a

cubic material.

From Equation 4.2, one can see that if kb is sufficiently small ($k = \frac{2\pi f}{v}$), FOM is proportional to $b^{\frac{3}{2}}$; if kb is sufficiently large, FOM is proportional to $b^{-\frac{1}{2}}$. The relationships between FOM and b at frequencies 1, 2 and 5 MHz are shown as the red, yellow and purple curves in Figure 4.4. It can be seen that at all the frequencies, the FOM increases when b is below 0.15 mm. After that, the FOM at 1 MHz starts to decrease, while the FOM curves at 2 and 5 MHz still increase but at slower rates, which shows that the transition region happens at a smaller b with a higher f (larger k), as expected. As grain size only affects the FOM term in the noise calculation, the noise has the same grain size dependence as the FOM.

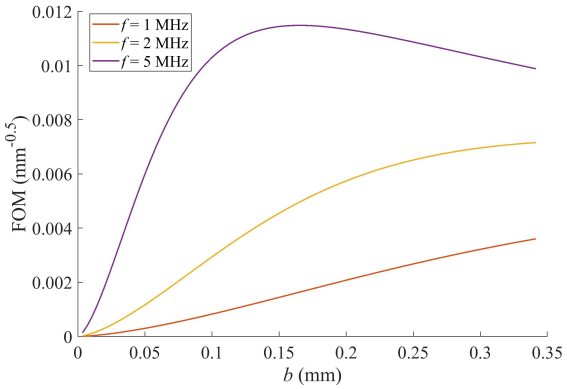


Figure 4.4: Typical FOM against half of grain size curves, plotted using Equation 4.2 at frequencies 1 MHz, 2 MHz and 5 MHz. ρ = 8000 kg/m^3, C_{11} = 246.8 GPa, C_{12} = 144.0 GPa, C_{44} = 102.9 GPa.

Grain size also has a significant impact on the attenuation. The grain size dependence of the attenuation has been discussed in [29]. It has been demonstrated that the attenuation coefficient is proportional to b^3 in the Rayleigh region, b in the stochastic region and b^{-1} in the geometric region. The relevance of the squared noise and the scattering induced attenuation can be found by comparing the grain size dependence of them. They both increase with b^3 at low kb and decrease with b^{-1} at high kb. This relevance can be explained by the law of energy conservation and indicates that the increase in noise is always along with the increase in attenuation. Therefore, in the Rayleigh or stochastic re-

gion, increasing the grain size increases both the noise and scattering induced attenuation, thereby decreasing the SNR. In this study, the grain size is defined as the average linear dimension of grains and it is constant at 0.34 mm, a typical grain size for creep-resistant materials.

4.3.3 Effect of defect size

In the following sections, examples will be given for discussion. SNR maps of the examples are generated using the procedure introduced in Section 4.2. As the inspection cylinder of a single transducer is always the target for an optimisation problem, the dependence of the cylinder parameters on various factors is of great interest and will be discussed here.

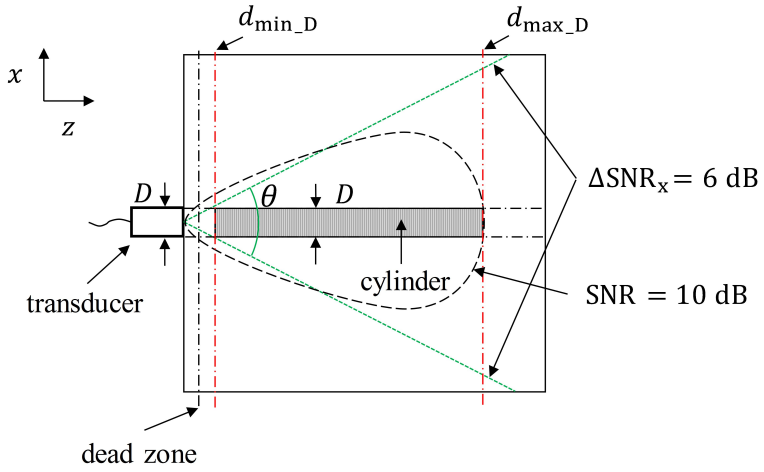


Figure 4.5: A schematic of a SNR map. θ represents the divergence angle of a -6 dB decrease in the echo field of the SNR. d_{min_D} and d_{max_D} are the minimum and maximum depths of a cylinder with the same diameter as the transducer, in which $\Delta SNR_x \leq 6$ dB and SNR$\geq$10 dB. It is also required that the cylinder is beyond the dead zone.

Figure 4.5 shows a schematic of a SNR map with an inspection cylinder of the same diameter as the transducer. The green lines show a -6 dB decrease in the echo field of the SNR with a divergence angle θ between them. The long-dashed curve shows where the SNR is equal to 10 dB. The end of the dead zone, the region in which the reflection from a reflector overlaps with the excitation signal and so cannot be identified, is shown

with a black dash-dotted line. The minimum and maximum depths $d_{\text{min\_D}}$ and $d_{\text{max\_D}}$ of the cylinder are determined by the example requirements:

1. the cylinder is beyond the dead zone ($d_{\text{min\_D}} \geq \frac{n\lambda}{2}$, where n is the number of cycles in the toneburst and λ is the wavelength);
2. in this cylinder, the SNR must be larger than 10 dB (inside the black long-dashed curve);
3. in this cylinder, the radial variation of the SNR must be less than 6 dB (in between the green lines).

Next, we will discuss how the divergence angle θ, minimum and maximum depths $d_{\text{min\_D}}$ and $d_{\text{max\_D}}$ of the cylinder change with the parameters. It is worth noting that the trends obtained with this cylinder are not restricted to the cylinder diameter but are expected to be seen for an inspection cylinder of any diameter.

Three defect diameters, 1, 2 and 5 mm, are considered for comparison. The anisotropy factor, transducer centre frequency and diameter are 2.0, 1.8 MHz and 3.4 mm respectively. The SNR maps are shown in Figure 4.6.

It can be seen that the divergence angle θ and the minimum depth of the cylinder $d_{\text{min\_D}}$ do not change with the defect diameter. This is obvious as the divergence angle θ is only affected by the transducer diameter to wavelength ratio [13] and $d_{\text{min\_D}}$ is determined by θ and D, which are the same in the three cases. It can also be seen that the maximum depth of the cylinder $d_{\text{max\_D}}$ rises with increasing defect size. This is also expected because the defect reflection from a small flat-bottom hole is proportional to the squared hole radius [100].

4.3.4 Effects of anisotropy factor

Next, we will discuss how anisotropy factor affects the SNR. Three fictitious materials, which have the same Voigt velocity, Poisson's ratio and density but have different

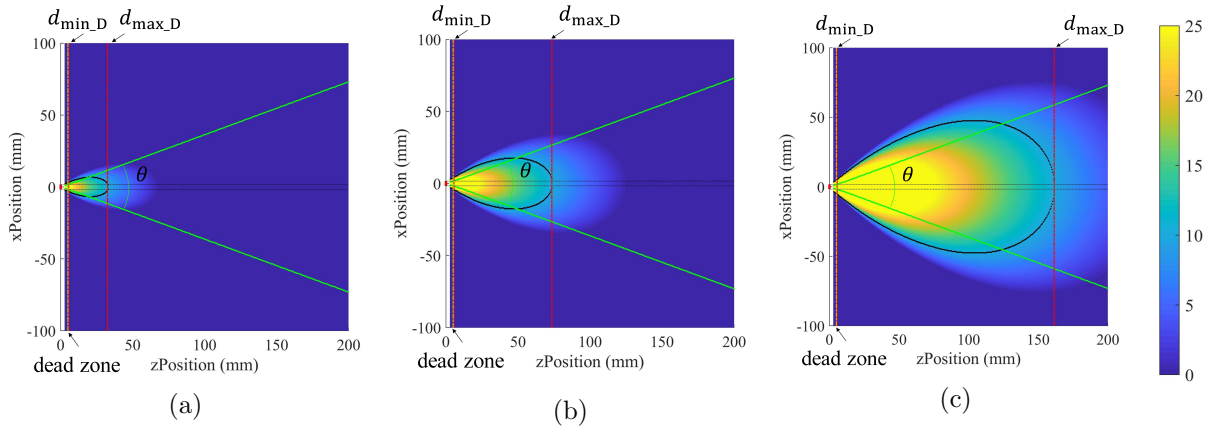


Figure 4.6: SNR maps (in dB) with defect diameters of (a) 1, (b) 2 and (c) 5 mm. θ represents the divergence angle of a −6 dB decrease in the SNR echo field. $d_{\text{min\_D}}$ and $d_{\text{max\_D}}$ are the minimum and maximum depths of a cylinder with the same diameter as the transducer, in which $\Delta\text{SNR}_x \leq 6$ dB (in between the green lines) and SNR≥10 dB (inside the black curve).

Table 4.3: Elastic constants for the fictitious cubic materials

Anisotropy factor	C_{11} (GPa)	C_{12} (GPa)	C_{44} (GPa)
1.2	276.2	129.3	88.2
2.0	246.8	144.0	102.9
2.8	231.0	151.9	110.8

anisotropy factors of 1.2, 2.0 and 2.8 are discussed here and their elastic constants are listed in Table 4.3. The defect diameter, transducer centre frequency and diameter are 5 mm, 1.8 MHz and 3.4 mm respectively. The SNR maps are shown in Figure 4.7.

It can be seen from Figure 4.7 that $d_{\text{min\_D}}$ and θ are not affected by the anisotropy factor, which is expected because the transducer diameter and wavelength are constant in the three cases. Figure 4.7 also shows that with increasing anisotropy factor, $d_{\text{max\_D}}$ decreases, which indicates a decrease of the SNR in the maps. To explain this trend, the relationships of FOM and anisotropy factor at different frequencies 1, 2, 5 and 10 MHz are obtained with Equation 4.2 and plotted in Figure 4.8. Each point in the figure shows the FOM calculated with the elastic constants which are obtained with the corresponding anisotropy factor. It can be seen that the FOM increases with the anisotropy factor

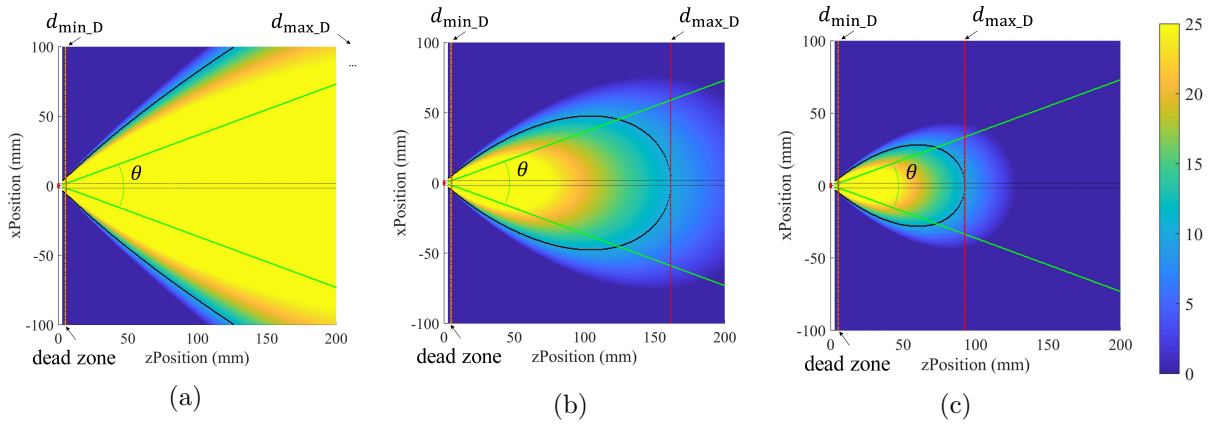


Figure 4.7: SNR maps (in dB) with anisotropy factors of (a) 1.2, (b) 2.0 and (c) 2.8. θ represents the divergence angle of a −6 dB decrease in the SNR echo field. $d_{\text{min\_D}}$ and $d_{\text{max\_D}}$ are the minimum and maximum depths of a cylinder with the same diameter as the transducer, in which $\Delta\text{SNR}_\text{x}$ ≤6 dB (in between the green lines) and SNR≥10 dB (inside the black curve).

at any frequency, which results in an increase in both the noise and scattering induced attenuation, causing the decrease of $d_{\text{max\_D}}$ shown in Figure 4.7. It is also noticed that the FOM does not always increase with frequency, which is consistent with the finding shown in Figure 3.5.

4.3.5 Effects of transducer parameters

As the transducer frequency and diameter to wavelength ratio are usually the solutions to the optimisation problems, it is of great importance to have a good understanding of their influence on SNR. Compared to the factors discussed in the previous sections, the transducer parameters have more complicated influence on SNR, as they affect the backscattering noise, scattering amplitude of the defect, scattering induced attenuation and beam divergence. Therefore, we will mainly use the SNR maps to show their influence. This section will begin with investigating the effects of the transducer frequency on SNR and then discuss those of the transducer diameter to wavelength ratio.

Three frequencies, 1.4, 1.8 and 2.2 MHz are considered here. To keep $\frac{D}{\lambda}$ constant, the transducer diameters are 6.4, 5 and 4.1 mm respectively. The transducer diameter to

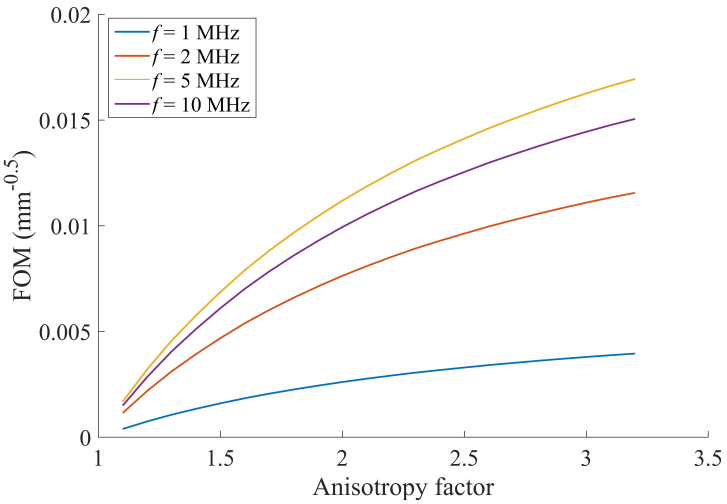


Figure 4.8: FOM versus anisotropy factor at frequencies 1, 2, 5 and 10 MHz obtained using Equation 4.2. Each point shows the FOM calculated with the elastic constants which are obtained with the corresponding anisotropy factor.

wavelength ratio, defect diameter and anisotropy factor are 1.5, 2 mm and 2.0. The SNR maps are shown in Figure 4.9.

It can be seen that the divergence angle θ does not change with the frequency as $\frac{D}{\lambda}$ is constant. $d_{\text{min\_D}}$ decreases with frequency, as θ is constant but D decreases. It is also shown that $d_{\text{max\_D}}$ decreases with frequency, which is dominated by the scattering induced attenuation, demonstrated by Figure 4.10 showing the SNR maps without attenuation.

Next, the effects of the transducer diameter to wavelength ratio on SNR will be investigated. Three ratios, 1, 1.5 and 2, are used here for discussion. The defect diameter, anisotropy factor and transducer centre frequency are 5 mm, 2.0 and 1.8 MHz respectively. The SNR maps are shown in Figure 4.11

Figure 4.11 shows that with increasing transducer diameter to wavelength ratio, the divergence angle θ decreases, as expected, and $d_{\text{min\_D}}$ increases as a result of the decrease of θ and increase of D. It is also shown that $d_{\text{max\_D}}$ increases with $\frac{D}{\lambda}$, as the energy is more concentrated.

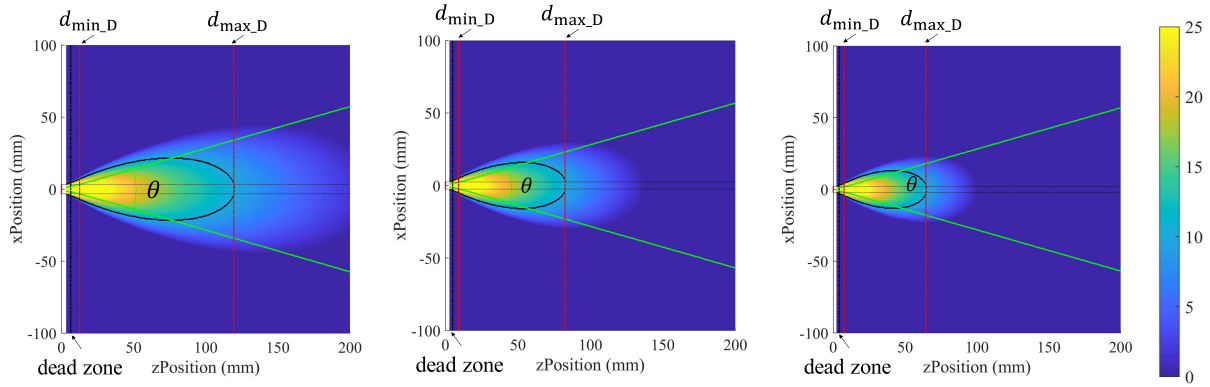


Figure 4.9: SNR maps (in dB) with transducer frequencies of (a) 1.4, (b) 1.8 and (c) 2.2 MHz with a constant $\frac{D}{\lambda}$. The attenuation term is applied in the signal computation but not in the noise calculation. θ represents the divergence angle of a −6 dB decrease in the SNR echo field. $d_{\text{min\_D}}$ and $d_{\text{max\_D}}$ are the minimum and maximum depths of a cylinder with the same diameter as the transducer, in which $\Delta\text{SNR}_x \leq 6$ dB (in between the green lines) and SNR≥10 dB (inside the black curve).

4.3.6 Summary

In this section, the influence of various factors on SNR has been investigated. It is shown that increasing the grain size (in the Rayleigh or stochastic region), anisotropy factor, excitation duration and decreasing the defect size reduce the SNR. The SNR also decreases with increasing frequency (at constant transducer diameter to wavelength ratio), dominated by the scattering induced attenuation. With an increasing transducer diameter to wavelength ratio (at constant frequency), the divergence angle decreases, which results in an increase in the SNR close to the centre line of the beam due to energy concentration.

The dependencies of the divergence angle θ, the minimum and maximum depths ($d_{\text{min\_D}}$ and $d_{\text{max\_D}}$) of an inspection cylinder with a diameter of D on the various factors are discussed. The results are summarised in Table 4.4, where the upward arrows, downward arrows and short-lines indicate that the quantities increase, decrease and are unaffected respectively with the corresponding factors. The effects of the grain size and excitation duration on the quantities are not obtained directly from SNR maps, but inferred from

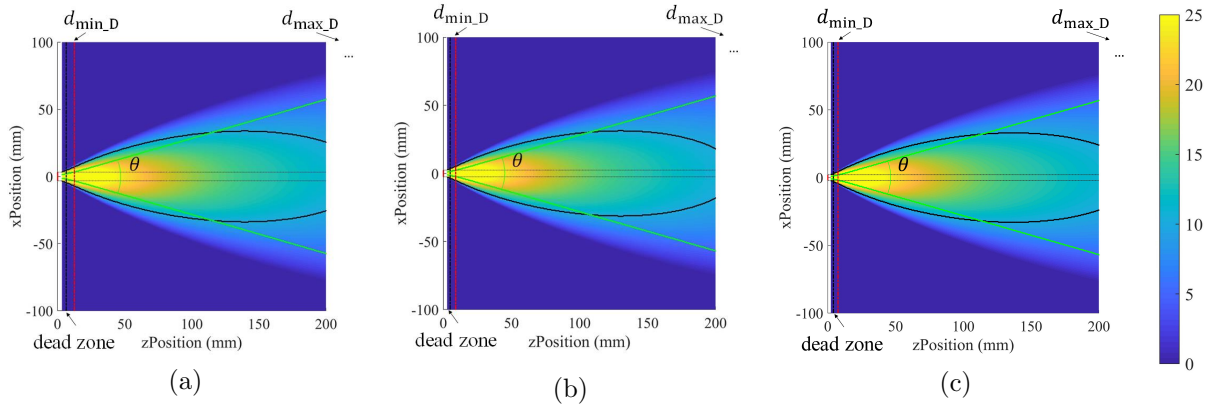


Figure 4.10: SNR maps (in dB) with transducer frequencies of (a) 1.4, (b) 1.8 and (c) 2.2 MHz with a constant $\frac{D}{\lambda}$. No attenuation term considered in the calculation. θ represents the divergence angle of a −6 dB decrease in the SNR echo field. d_{min_D} and d_{max_D} are the minimum and maximum depths of a cylinder with the same diameter as the transducer, in which ΔSNR_x ≤6 dB (in between the green lines) and SNR≥10 dB (inside the black curve).

Table 4.4: Summary of how d_{min_D}, d_{max_D} and θ change with various factors

Increasing	d_{min_D}	d_{max_D}	θ
Grain size (in the Rayleigh or stochastic region)	–	↓	–
Excitation duration	–	↓	–
Defect size	–	↑	–
Anisotropy factor	–	↓	–
Transducer frequency f (at constant $\frac{D}{\lambda}$)	↓	↓	–
Transducer diameter to wavelength ratio $\frac{D}{\lambda}$	↑	↑	↓

the changes predicted with the theories. It is worth noting that although an inspection cylinder with a diameter of D is used for discussion, the trends shown in Table 4.4 are expected to be seen for an inspection cylinder of any diameter and they will be used in the discussions of general cases later.

4.4 Case studies

In addition to the requirements of the minimum SNR value and maximum radial SNR variation in the inspection cylinder from a single transducer, mentioned in Section 4.1,

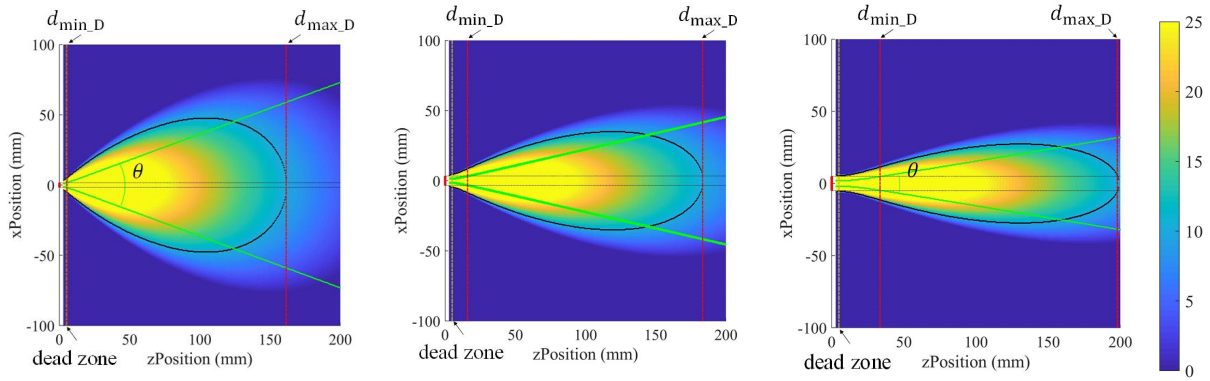


Figure 4.11: SNR maps (in dB) with transducer diameters of (a) 3.4, (b) 6.7 and (c) 10 mm. With a constant frequency of 1.8 MHz, the transducer diameter to wavelength ratios are 1, 1.5 and 2 respectively. θ represents the divergence angle of a −6 dB decrease in the SNR echo field. $d_{\text{min\_D}}$ and $d_{\text{max\_D}}$ are the minimum and maximum depths of a cylinder with the same diameter as the transducer, in which $\Delta\text{SNR}_{\text{x}} \leq 6$ dB (in between the green lines) and SNR≥10 dB (inside the black curve).

the optimisation problem also often requires:

- a minimum transducer diameter to ensure that it is practical to construct and deploy with the appropriate cables;
- a minimum transducer diameter to wavelength ratio to guarantee the efficiency of the radiation to the longitudinal wave [101];
- the inspection cylinder diameter to be greater than or equal to the transducer diameter to avoid the need to overlap transducers to obtain full coverage;
- the inspection cylinder to be beyond the dead zone to get a full depth coverage in the inspection volume.

All the requirements mentioned above are considered in this section as example requirements, of which the details are listed below:

1. the minimum SNR in the inspection cylinder is 10 dB;

2. the maximum radial SNR variation in the inspection cylinder is 6 dB;

3. the minimum transducer diameter $D_{\min}$ is 3 mm;

4. the minimum transducer diameter to wavelength ratio $(\frac{D}{\lambda})_{\min}$ is 0.5;

5. the inspection cylinder diameter D_c is greater than or equal to the transducer diameter D;

6. the inspection cylinder is beyond the dead zone.

Apart from the requirements, the optimisation problem also needs a criterion. In this section, two possible criteria are given, as discussed below.

In some applications, it is desirable to monitor the sample from a given depth, referred to as the minimum depth of interest, to a depth as deep as possible with non-overlapping transducers. For an optimisation problem like this, the optimal transducer gives the largest maximum depth ($d_{\text{max\_D}}$) of the inspection cylinder projected from the transducer with a given minimum depth of interest ($d_{\min}$). With this criterion, the whole surface is covered with transducers so the fractional surface area covered with transducers ($\frac{D^2}{{D_c}^2}$) is unity. A schematic of a SNR map under this criterion (referred to as Criterion 1) is shown in Figure 4.12a.

In some other applications, where there is a specified depth range of interest, a small transducer being able to cover a large area relative to the transducer surface in the given depth range is desirable. For an optimisation problem like this, the optimal transducer gives the smallest fractional surface area that has to be covered with transducers to monitor a specified depth range of interest ($d_{\min}$ to $d_{\max}$) over the whole testpiece. A schematic of a SNR map under this criterion (referred to as Criterion 2) is shown in Figure 4.12b.

In this study, the optimal transducer parameters and placement are determined via comparing the SNR maps generated with multiple transducer frequency and diameter

$(f - D)$ combinations.

Next, two representative example optimisation problems, under each criterion respectively, will be discussed and the results of the examples will be illustrated with the trends obtained in Section 4.3. Both of the examples consider a flat-bottom hole with a diameter of 2 mm in a fictitious cubic material of which the elastic constants (C_{11}, C_{12}, C_{44}) are (246.8 GPa, 144.0 GPa, 102.9 GPa), the anisotropy factor A_z is 2.0 and the Voigt longitudinal wave velocity is 6000 m/s.

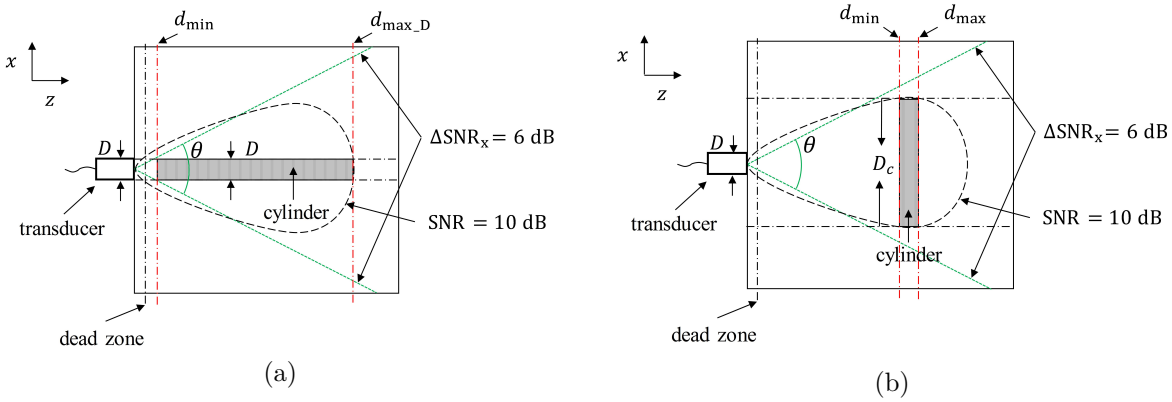


Figure 4.12: Schematics of SNR maps under Criteria (a) 1 and (b) 2. D and D_c show the diameters of the transducer and inspection cylinder respectively. $d_{\min}$ and $d_{\max}$ are the minimum and maximum depths of interest. $d_{\max\_D}$ is the maximum depth that can be covered by an inspection cylinder with a diameter of D, in which $\Delta\text{SNR}_x \leq 6$ dB (in between the green lines) and SNR$\geq$10 dB (inside the black curve).

4.4.1 Example 1

This section will show how to find the optimal $f - D$ combination under Criterion 1 with a minimum depth of interest $d_{\min}$ of 7.5 mm.

Firstly, the minimum frequency and diameter to wavelength ratio are determined by the requirements. As the inspection cylinder should be able to cover the minimum depth of interest $d_{\min}$, according to requirement 6, there should be no dead zone effect beyond $d_{\min}$, which means $\frac{3\lambda}{2} \leq d_{\min}$ (the excitation is a 3-cycle toneburst), where λ is wavelength.

From this inequality, it can be seen that if regions close to the top surface are to be monitored, a relatively high frequency is needed to limit the dead zone, while if the regions are far away from the transducer, a low frequency can be used. By solving the inequality, the minimum frequency is obtained as 1.2 MHz. According to requirement 4, the minimum diameter to wavelength ratio $(\frac{D}{\lambda})_{\min}$ is 0.5. Then, the frequency and ratio will be increased gradually from the minima and with each $f - D$ combination in which the transducer diameter meets requirement 3 ($D \geq 3$ mm), a SNR map will be generated. The process will stop when the optimal combination is found by comparing the SNR maps.

Figure 4.13 shows the maximum depths of the inspection cylinders (in mm) obtained with different $f - D$ combinations. The vertical axis shows the diameter to wavelength ratio and the horizontal axis shows the frequency. From the figure, two blank parts at the top-right and bottom-left corners can be seen. The SNR maps with the $f-D$ combinations in the top-right blank area are not generated as the transducer diameter is less than 3 mm. With the $f - D$ combinations in the bottom-left blank area, where $\frac{D}{\lambda}$ is relatively high, no inspection cylinder with a diameter equal to the transducer diameter can be obtained, due to the relatively small divergence angle and big transducer diameter.

From Figure 4.13, we can see that the optimal frequency and diameter to wavelength ratio are 1.2 MHz and 1 respectively, with which the maximum depth is 111 mm. The optimum is at a defect diameter to wavelength ratio of 0.4, so the approximation using the squared particle velocity is reasonable. From the parametric studies in the previous sections, we know that the maximum depth of an inspection cylinder decreases with frequency, dominated by the scattering induced attenuation, and increases with $\frac{D}{\lambda}$, due to energy concentration. Therefore, to get the largest $d_{\max\_D}$, the minimum f and maximum $\frac{D}{\lambda}$ should be used, which is consistent with the result.

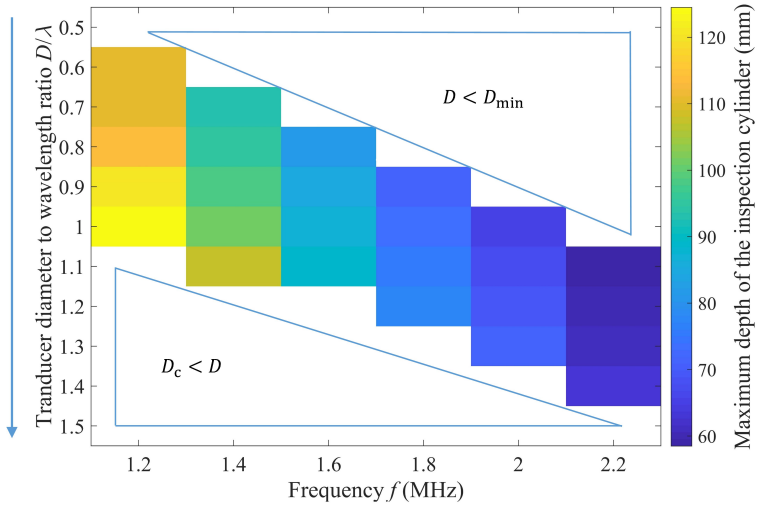


Figure 4.13: Maximum depths of the inspection cylinders at different $f-D$ combinations. D and $D_{\min}$ are the transducer diameter and its minimum requirement. D_c here shows the maximum inspection cylinder diameter determined by the requirements. The inequalities show the reasons for the blank areas. The $y-$axis scale increases downwards.

4.4.2 Example 2

Next, we will discuss another optimisation problem based on Criterion 2 with a depth range of interest from 95 mm to 105 mm. This example has potential application in weld monitoring, of which the geometry is shown schematically in Figure 4.14. It can be seen from the figure that the transmit-receive distances are similar over the whole fusion face, so it is equivalent to monitoring over a narrow depth range relatively far away from the transducer.

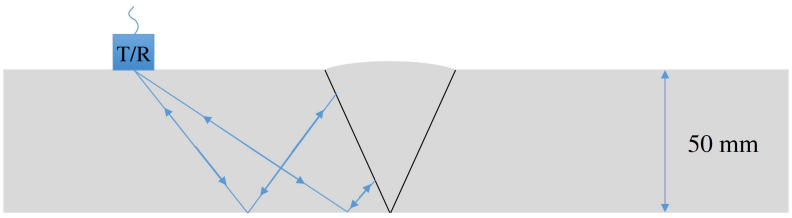


Figure 4.14: Weld monitoring geometry; T/R means transmitter/receiver.

With the same procedure described in example 1, the SNR maps with multiple $f-D$

combinations are generated, from which the fractional surface areas covered with transducers ($\frac{D^2}{{D_c}^2}$, in percentage) at different $f-D$ combinations are obtained and shown in Figure 4.15. The vertical axis shows the diameter to wavelength ratio and the horizontal axis shows the frequency. From the figure, three blank parts can be seen. Like example 1, the blank areas at the top-right corner (shown with a blue triangle) and the bottom-left corner (shown with a red rectangle) are because the transducer diameter is less than the minimum requirement and no inspection cylinder with a diameter greater than or equal to the transducer diameter can be obtained respectively. With the $f-D$ combinations in the orange polygon, the maximum depth of interest cannot be covered with any inspection cylinder with a diameter equal to the transducer diameter due to strong attenuation induced by scattering. As the value of $\frac{D^2}{{D_c}^2}$ varies in a large range, in order to show the minimum clearly, the colour bar is set with a relatively small range from 0 % to 4 %.

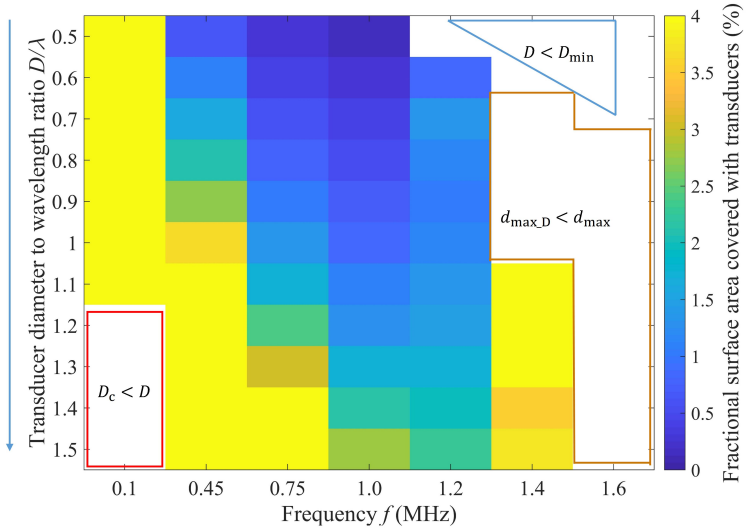


Figure 4.15: Fractional surface areas covered with transducers ($\frac{D^2}{{D_c}^2}$) at different $f-D$ combinations. D and D_c show the diameters of the transducer and inspection cylinder respectively. d_{max} is the maximum depth of interest. d_{max_D} is the maximum depth that can be covered by an inspection cylinder with a diameter of D. D_{min} is the minimum requirement of the transducer diameter. The inequalities show the reasons for the blank areas. The $y-$axis scale increases downwards.

From Figure 4.15, we can see that the optimal frequency is 1 MHz and the optimal

diameter to wavelength ratio is 0.5, with which $\frac{D^2}{{D_c}^2}$ is 0.17 %. The optimum is at a defect diameter to wavelength ratio of about 0.33, so the approximation using the squared particle velocity is reasonable. Compared to example 1, it is difficult to predict the result of this example by the trends obtained previously, because the relationship between $\frac{D^2}{{D_c}^2}$ and f and the relationship between $\frac{D^2}{{D_c}^2}$ and $\frac{D}{\lambda}$ are not monotonic. For example, if D_c is restricted by the divergence angle, which is not affected by f, $\frac{D^2}{{D_c}^2}$ will decrease with increasing f at a constant $\frac{D}{\lambda}$. However, if D_c is restricted by the contour line of the minimum SNR value (10 dB here), as shown in Figure 4.12b, D_c is affected by f, and in this case, no consistent trend of $\frac{D^2}{{D_c}^2}$ with increasing f can be predicted.

4.5 Summary of the chapter

In this chapter, a combined analytical-and-numerical method for SNR map generation has been introduced. The grain noise is predicted theoretically and the reflections from a flat-bottom hole, as a calibration defect, at one position are computed using FE. Overall SNR maps for holes at different locations are produced by scaling the reflection amplitudes by the squared particle velocity and the scattering induced attenuation.

The influence of various factors, including excitation type and duration, grain size and anisotropy factor, defect size, transducer frequency and diameter on SNR has been investigated. It is found that the SNR decreases with increasing grain size (in the Rayleigh or stochastic region), anisotropy factor, excitation duration and decreasing defect size. Increasing the frequency (at constant transducer diameter to wavelength ratio) reduces the SNR, dominated by the scattering induced attenuation. Increasing the transducer diameter to wavelength ratio (at constant frequency) decreases the divergence angle, which results in an increase in the SNR close to the centre line of the beam due to energy concentration. The dependencies of the θ, the minimum and maximum depths ($d_{\mathrm{min\_D}}$ and $d_{\mathrm{max\_D}}$) of an inspection cylinder with a diameter of D on the various factors are

summarised in Table 4.4, where the upward arrows, downward arrows and short-lines indicate that the quantities increase, decrease and are unaffected respectively with the corresponding factors.

A procedure of how to solve the optimisation problem and find the optimal transducer parameters and placement with SNR maps has been proposed. Two representative example optimisation problems, under two possible criteria respectively, have been discussed. In these examples the optimum is at a defect diameter to wavelength ratio of $0.3 \sim 0.4$, so it is reasonable to approximate the reflection from a defect at any position by scaling by the squared particle velocity. It is found that if regions close to the top surface are to be monitored, a relatively high frequency is needed to limit the dead zone. For highly scattering materials and large inspection depths, a low frequency is required to reduce the attenuation and the depth range can be increased by increasing $\frac{D}{\lambda}$ at a cost of increasing the fractional surface area that must be covered with transducers. For modest scattering, a narrow depth range far from the surface can be monitored with a small surface area covered with transducers, which has potential application in weld monitoring.

Chapter 5 Conclusions

5.1 Thesis review

This thesis aims at overcoming the low SNR problem caused by grain boundary scattering in monitoring of large grained materials. The potential of two techniques, a signal processing procedure based on baseline subtraction and optimising the transducers and their placement used in the monitoring system, to achieve the goal has been investigated. As there is a lack of an accurate noise prediction for 3D highly scattering problems, which is desirable in optimising the transducers, 3D FE modelling has been proposed as an approach to achieve it.

Chapter 2 has presented an experimental study investigating the feasibility and reliability of comparing repeat tests using a signal processing procedure based on baseline subtraction to suppress grain noise. The calibration methods used to set the transducer with the same stand-off and angle relative to the testpiece in repeat scans have been presented and the effect of transducer set-up errors has been discussed. An image alignment method has been used to register C-scan images to find the same location in different scans and the effect of errors in the registration has been investigated. Compensation methods for temperature variations and transducer frequency response changes, which are very likely to happen in practice, have been presented and their effectiveness has been tested. The main results obtained in Chapter 2 are listed below.

1. When there are no temperature and transducer frequency response changes, a SNR improvement of around 15 dB was achieved by baseline subtraction.

2. A SNR improvement of around 11 dB was obtained by subtracting a temperature

compensated baseline signal from a current signal with a temperature difference of 10 °C.

3. Using the proposed frequency compensation method, an improvement of around 10 dB was achieved when the transducer peak frequency response changed by as much as ±250 kHz from a baseline value of around 7 MHz.

To summarise, a modest noise reduction can be achieved by using baseline subtraction when there are relatively small temperature and transducer frequency response changes between the baseline and current signals and the dominant factors restricting the improvement are the temperature and transducer frequency response changes. However, it is also worth noting that this improvement was obtained in lab conditions without any change of the sample surface or grain structure and at significant cost in test complexity and data storage requirements.

Chapter 3 has presented an alternative approach to predict grain noise, 3D FE modelling. Unlike the established theories whose validities are often limited to weakly scattering regimes, the FE approach shows a strong potential in describing the noise behaviour in highly scattering regimes, as it solves the full physics problem including multiple scattering. This approach has been validated by comparing the FE predicted L-L scattering amplitudes from a single grain with the theoretical solutions. Two transmit-receive configurations, one with a plane wave excitation and incoherent averaging of the received signals and another one with a pulse-echo configuration with a finite transducer, have been considered. The RMS noise levels of the two configurations have been predicted by FE and the theoretical models which are developed in a similar way to that used to develop the Independent Scatterer Model that is the basis of most previous analytical predictions.

The main findings of Chapter 3 are listed below.

1. 3D FE modelling is a valid approach for grain noise prediction.

2. With a plane wave excitation and incoherent averaging of the received signals, significantly higher noise is observed in the FE results than the theoretical predictions. This has been demonstrated to be largely due to the shear wave component which is not considered in the theoretical model. As the contribution of shear waves can be cancelled out quickly by doing a spatial average over the transducer surface, a theoretical model ignoring shear waves is expected to give good estimations of grain noise when considering a realistic transducer which generates a spatial average.

3. With a pulse-echo configuration with a finite transducer, when neglecting the attenuation, good agreement between the FE and theoretical predictions can be seen when the anisotropy factor is relatively low, while discrepancies can be observed when the anisotropy factor gets higher, indicating the occurrence of multiple scattering. When adding the attenuation whose coefficient is deduced from the excitation and back-wall signals to the theoretical noise model, the predictions are significant lower than the FE results for all the anisotropy factors. This is because the incoherent noise is much less affected by the scattering induced attenuation than the coherent signals.

To sum up, it has been demonstrated that the FE approach is a powerful tool to predict the grain noise. However, it is very computationally expensive, which can limit its application in practice. Furthermore, the comparison of the FE and theoretical noise shows that the theoretical model can give a rough estimation of the grain noise level very efficiently, although there are some discrepancies. Therefore, the theoretical model can be used to give a first estimate of grain noise level, and the FE approach can be used to provide a more accurate prediction where required.

Chapter 4 has proposed a procedure of finding the optimal transducer parameters and placement for a permanently installed monitoring system. A combined analytical-and-numerical method to generate a SNR map has been introduced and the influence of various factors, including excitation type and duration, grain size and anisotropy factor,

defect size, transducer frequency and diameter, on SNR has been investigated. It has been found that:

1. the SNR decreases with increasing grain size (in the Rayleigh or stochastic region), anisotropy factor, excitation duration and decreasing defect size;

2. increasing the frequency (at constant transducer diameter to wavelength ratio) reduces the SNR, which is dominated by the scattering induced attenuation;

3. with increasing transducer diameter to wavelength ratio (at constant frequency), the divergence angle decreases, which causes an increase in the SNR near the centre line of the beam due to the concentration of energy.

Two possible criteria and two examples showing how to find the optimal transducer parameters under each criterion have been given. The main findings of Chapter 4 are:

1. a relatively high frequency is needed if regions close to the top surface are to be monitored to remove the dead zone effect in the monitored area;

2. a low frequency is required if highly scattering materials and large inspection depths are to be monitored to reduce the attenuation and by increasing $\frac{D}{\lambda}$, the monitoring depth can be increased at a cost of increasing the fractional surface area that must be covered with transducers;

3. for modest scattering, a narrow depth range far from the surface can be monitored with a small surface area covered with transducers, which has potential application in weld monitoring.

5.2 Suggestions for future work

Reviewing the aim of the project and the work having been done, it is clear that significant achievement has been made to address the goal. However, there are still some issues which

can be further pursued. Since each of the three main chapters considers rather different subjects, the suggestions for future work will be given for each chapter separately.

In Chapter 2, as the results show that the improvement of baseline subtraction is restricted by the temperature and transducer response changes, efforts can be made to develop other signal processing techniques to increase the similarity of the compensated baseline and current signals, thereby enhancing the improvement. As the change of the grain structure can significantly affect the validity of baseline subtraction, the effect of long-term exposure at high temperatures, like 700 °C, on grain structures also needs to be looked into. This can be done by heating the material to a high temperature for one or two months between two repeat scans and comparing the results.

In Chapter 3, it has been reviewed that most of the theoretical models are based on the single scattering assumption, which limits their application to weakly scattering problems. Hu and Turner have developed a model considering single and double scattering effects [58]. This shows potential for solving the full multiple scattering problem theoretically, which can be further pursued. On the other hand, although 3D FE modelling has been proved to be a powerful tool for noise prediction, the high computational costs can limit its application in practice. Therefore, how to reduce the computational costs of FE simulations is also worth investigating.

In Chapter 4, the optimisation problem of how to find the optimal transducer for a permanently installed monitoring system has been solved in an analytical-and-numerical way. It is also possible to solve this problem in a purely analytical way, where the analytical solution of SNR is required. Although it might be less accurate due to the assumptions introduced in the analytical model, it can significantly reduce the computational costs and provide first estimates very efficiently. Experimental validation of the proposed procedures of generating SNR maps and finding the optimal transducer parameters should also be pursued and will be before submitting a paper for journal publication.

Bibliography

[1] Lau K, McCurdy AK. Elastic anisotropy factors for orthorhombic, tetragonal, and hexagonal crystals. *Physical Review B* 1998; **58**:8980–8984.

[2] Bugge J, Kjaer S, Blum R. High-efficiency coal-fired power plants development and perspectives. *Energy* 2006; **31**:1437–1445.

[3] Langdon TG. Grain boundary sliding as a deformation mechanism during creep. *Philosophical Magazine* 1970; **22**:689–700.

[4] Dieter GE. *Mechanical Metallurgy*. New York: McGraw Hill, 1961.

[5] Lasalmonie A, Strudel JL. Influence of grain size on the mechanical behaviour of some high strength materials. *Journal of Materials Science* 1986; **21**:1837–1852.

[6] Webster GA, Ainsworth RA. *High Temperature Component Life Assessment*. Springer Science & Business Media, 2013.

[7] Viswanathan R. *Damage Mechanisms and Life Assessment of High Temperature Components*. ASM international, 1989.

[8] Allgaier MW, Ness S. *ASNT Nondestructive Testing Handbook: Visual and Optical Testing*. American Society of Nondestructive Testing, 1993.

[9] McMaster RC. *ASNT Nondestructive Testing Handbook: Liquid Penetrant Tests*. American Society of Nondestructive Testing, 1982.

[10] Schmidt JT, Skeie K. *ASNT Nondestructive Testing Handbook: Magnetic Particle Testing*. American Society of Nondestructive Testing, 1989.

[11] Halmshaw R. *Industrial Radiology: Theory and Practice*. Springer Science & Business Media, 2012.

[12] Bryant LE. *ASNT Nondestructive Testing Handbook: Radiography and Radiation Testing*. American Society of Nondestructive Testing, 1985.

[13] Krautkrämer J, Krautkrämer H. *Ultrasonic Testing of Materials*. Springer Science & Business Media, 2013.

[14] Schmerr LW. *Fundamentals of Ultrasonic Nondestructive Evaluation: A Modeling Approach*. Springer US, 1998.

[15] Cawley P. Non-destructive testing - current capabilities and future directions. *Proceedings of the Institution of Mechanical Engineers, Part L: Journal of Materials: Design and Applications* 2001; **215**:213–223.

[16] Van Pamel A. Ultrasonic inspection of highly scattering materials. PhD Thesis, Imperial College London 2015.

[17] Mech SJ, Michaels TE, Emmons JS, Sugiyama MM. Development of ultrasonic examination methods for austenitic stainless steel weld inspection. *Technical Report*, Hanford Engineering Development Lab., Richland, Wash.(USA) 1977.

[18] Mason WP, McSkimin HJ. Attenuation and scattering of high frequency sound waves in metals and glasses. *Journal of the Acoustical Society of America* 1947; **19**:464–473.

[19] Roth W. Scattering of ultrasonic radiation in polycrystalline metals. *Journal of Applied Physics* 1948; **19**:901–910.

[20] Mason WP, McSkimin HJ. Energy losses of sound waves in metals due to scattering and diffusion. *Journal of Applied Physics* 1948; **19**:940–946.

[21] Huntington HB. On ultrasonic scattering by polycrystals. *Journal of the Acoustical Society of America* 1950; **22**:362–364.

[22] Lifshits IM, Parkhomovski GD. On the theory of ultrasonic wave propagation in polycrystals. *Zh. Eksp. Teor. Fiz* 1950; **20**:175–182.

[23] Merkulov LG. Investigation of the scattering of ultrasound in metals. *Zh. Tekhn. Fiz* 1956; **26**.

[24] Bhatia AB. Scattering of high-frequency sound waves in polycrystalline materials. *Journal of the Acoustical Society of America* 1959; **31**:16–23.

[25] Bhatia AB, Moore RA. Scattering of high frequency sound waves in polycrystalline materials. ii. *Journal of the Acoustical Society of America* 1959; **31**:1140–1141.

[26] Hirsekorn S. The scattering of ultrasonic waves by multiphase polycrystals. *Journal of the Acoustical Society of America* 1988; **83**:1231–1242.

[27] Hirsekorn S. The scattering of ultrasonic waves by polycrystals. *Journal of the Acoustical Society of America* 1982; **72**:1021–1031.

[28] Hirsekorn S. The scattering of ultrasonic waves in polycrystalline materials with texture. *Journal of the Acoustical Society of America* 1985; **77**:832–843.

[29] Stanke FE, Kino GS. A unified theory for elastic wave propagation in polycrystalline materials. *Journal of the Acoustical Society of America* 1984; **75**:665–681.

[30] Karal Jr FC, Keller JB. Elastic, electromagnetic, and other waves in a random medium. *Journal of Mathematical Physics* 1964; **5**:537–547.

[31] Stanke FE. Inversion of attenuation measurements in terms of a parameterized autocorrelation function. *ASM Metals Congress*, 1984.

[32] Yang L, Rokhlin SI. On comparison of experiment and theory for ultrasonic attenuation in polycrystalline niobium. *Journal of Nondestructive Evaluation* 2012; **31**:77–79.

[33] Weaver RL. Diffusivity of ultrasound in polycrystals. *Journal of the Mechanics and Physics of Solids* 1990; **38**:55–86.

[34] Yang L, Lobkis OI, Rokhlin SI. Explicit model for ultrasonic attenuation in equiaxial hexagonal polycrystalline materials. *Ultrasonics* 2011; **51**:303–309.

[35] Ahmed S, Thompson RB. Propagation of elastic waves in equiaxed stainless-steel polycrystals with aligned [001] axes. *Journal of the Acoustical Society of America* 1996; **99**:2086–2096.

[36] Turner JA. Elastic wave propagation and scattering in heterogeneous, anisotropic media: Textured polycrystalline materials. *Journal of the Acoustical Society of America* 1999; **106**:541–552.

[37] Yang L, Rokhlin SI. Ultrasonic backscattering in cubic polycrystals with ellipsoidal grains and texture. *Journal of Nondestructive Evaluation* 2013; **32**:142–155.

[38] Chassignole B, Duwig V, Ploix MA, Guy P, El Guerjouma R. Modelling the attenuation in the athena finite elements code for the ultrasonic testing of austenitic stainless steel welds. *Ultrasonics* 2009; **49**:653–658.

[39] Feuilly N, Dupond O, Chassignole B, Moysan J, Comeloup G. Relation between ultrasonic backscattering and microstructure for polycrystalline materials. *AIP Conference Proceedings*, vol. 1096, 2009; 1216–1223.

[40] Huthwaite P. Accelerated finite element elastodynamic simulations using the gpu. *Journal of Computational Physics* 2014; **257**:687–707.

[41] Van Pamel A, Brett CR, Huthwaite P, Lowe MJS. Finite element modelling of elastic wave scattering within a polycrystalline material in two and three dimensions. *Journal of the Acoustical Society of America* 2015; **138**:2326–2336.

[42] Van Pamel A, Sha G, Lowe MJS, Rokhlin SI. Numerical and analytic modelling of elastodynamic scattering within polycrystalline materials. *Journal of the Acoustical Society of America* 2018; **143**:2394–2408.

[43] Margetan FJ, Gray TA, Thompson RB. A technique for quantitatively measuring microstructurally induced ultrasonic noise. *Review of Progress in Quantitative Nondestructive Evaluation*, vol. 10B. 1991; 1721–1728.

[44] Margetan FJ, Thompson RB, Yalda-Mooshabad I. Backscattered microstructural noise in ultrasonic toneburst inspections. *Journal of Nondestructive Evaluation* 1994; **13**:111–136.

[45] Thompson RB, Gray TA. A model relating ultrasonic scattering measurements through liquid–solid interfaces to unbounded medium scattering amplitudes. *Journal of the Acoustical Society of America* 1983; **74**:1279–1290.

[46] Rose JH. Ultrasonic backscattering from polycrystalline aggregates using time-domain linear response theory. *Review of Progress in Quantitative Nondestructive Evaluation*, vol. 10B. 1991; 1715–1720.

[47] Rose JH. Ultrasonic backscatter from microstructure. *Review of Progress in Quantitative Nondestructive Evaluation*, vol. 11B. 1992; 1677–1684.

[48] Rose JH. Theory of ultrasonic backscatter from multiphase polycrystalline solids. *Review of Progress in Quantitative Nondestructive Evaluation*, vol. 12. 1993; 1719–1726.

[49] Thompson R, Margetan F, Han Y, Paxson AJ, Shamblen C. Relationship of microstructure to backscattered ultrasonic noise. *Review of Progress in Quantitative Nondestructive Evaluation*, vol. 11, 1992; 1685–1691.

[50] Ghoshal G, Turner JA, Weaver RL. Wigner distribution of a transducer beam pattern within a multiple scattering formalism for heterogeneous solids. *Journal of the Acoustical Society of America* 2007; **122**:2009–2021.

[51] Ghoshal G, Turner JA. Diffuse ultrasonic backscatter at normal incidence through a curved interface. *Journal of the Acoustical Society of America* 2010; **128**:3449–3458.

[52] Hu P, Kube CM, Koester LW, Turner JA. Mode-converted diffuse ultrasonic backscatter. *Journal of the Acoustical Society of America* 2013; **134**:982–990.

[53] Hu P, Turner JA. Transverse-to-transverse diffuse ultrasonic scattering. *Journal of the Acoustical Society of America* 2017; **142**:1112–1120.

[54] Han YK, Thompson RB. Ultrasonic backscattering in duplex microstructures: theory and application to titanium alloys. *Metallurgical and Materials Transactions A* 1997; **28**:91–104.

[55] Lobkis O, Yang L, Li J, Rokhlin S. Ultrasonic backscattering in polycrystals with elongated single phase and duplex microstructures. *Ultrasonics* 2012; **52**:694–705.

[56] Arguelles AP, Kube CM, Hu P, Turner JA. Mode-converted ultrasonic scattering in polycrystals with elongated grains. *Journal of the Acoustical Society of America* 2016; **140**:1570–1580.

[57] Margetan FJ, Haldipur P, Yu L, Thompson RB. Looking for multiple scattering effects in backscattered ultrasonic grain noise from jet-engine nickel alloys. *AIP Conference Proceedings*, vol. 760, 2005; 75–82.

[58] Hu P, Turner JA. Contribution of double scattering in diffuse ultrasonic backscatter measurements. *Journal of the Acoustical Society of America* 2015; **137**:321–334.

[59] Ghoshal G, Turner JA. Diffuse ultrasonic backscatter in a two-dimensional domain. *Acta mechanica* 2009; **205**:35–49.

[60] Bai X, Tie B, Schmitt JH, Aubry D. Finite element modeling of grain size effects on the ultrasonicmicrostructural noise backscattering in polycrystalline materials. *Ultrasonics* 2018; **87**:182–202.

[61] Aghaie-Khafri M, Honarvar F, Zanganeh S. Characterization of grain size and yield strength in aisi 301 stainless steel using ultrasonic attenuation measurements. *Journal of Nondestructive Evaluation* 2012; **31**:191–196.

[62] Wydra A, Chertov AM, Maev RG, Kube CM, Du H, Turner JA. Grain size measurement of copper spot welding caps via ultrasonic attenuation and scattering experiments. *Research in Nondestructive Evaluation* 2015; **26**:225–243.

[63] Zhang C, Li X, Song Y, Han X, Han J. Evaluating the grain size in curved components using the ultrasonic attenuation method with diffraction correction. *NDT & E International* 2016; **84**:20–26.

[64] Li X, Song Y, Liu F, Hu H, Ni P. Evaluation of mean grain size using the multi-scale ultrasonic attenuation coefficient. *NDT & E International* 2015; **72**:25–32.

[65] Li X, Han X, Arguelles AP, Song Y, Hu H. Evaluating grain size in polycrystals with rough surfaces by corrected ultrasonic attenuation. *Ultrasonics* 2017; **78**:23–29.

[66] Lobkis OI, Rokhlin SI. Characterization of polycrystals with elongated duplex microstructure by inversion of ultrasonic backscattering data. *Applied Physics Letters* 2010; **96**:161 905.

[67] Hull JB, Langton CM, Barker S, Jones AR. Identification and characterisation of materials by broadband ultrasonic attenuation analysis. *Journal of Materials Processing Technology* 1996; **56**:148–157.

[68] Yang L, Turner JA, Li Z. Ultrasonic characterization of microstructure evolution during processing. *Journal of the Acoustical Society of America* 2007; **121**:50–59.

[69] Newhouse VL, Bilgutay NM, Saniie J, Furgason ES. Flaw-to-grain echo enhancement by split-spectrum processing. *Ultrasonics* 1982; **20**:59–68.

[70] Karpur P, Canelones OJ. Split spectrum processing: a new filtering approach for improved signal-to-noise ratio enhancement of ultrasonic signals. *Ultrasonics* 1992; **30**:351–357.

[71] Aussel JD. Split-spectrum processing with finite impulse response filters of constant frequency-to-bandwidth ratio. *Ultrasonics* 1990; **28**:229–240.

[72] Abbate A, Koay J, Frankel J, Schroeder SC, Das P. Signal detection and noise suppression using a wavelet transform signal processor: application to ultrasonic flaw detection. *IEEE Transactions on Ultrasonics, Ferroelectrics, and Frequency Control* 1997; **44**:14–26.

[73] Lazaro JC, San Emeterio JL, Ramos A, Fernandez-Marron JL. Influence of thresholding procedures in ultrasonic grain noise reduction using wavelets. *Ultrasonics* 2002; **40**:263–267.

[74] Sharma GK, Kumar A, Rao BP, Jayakumar T. Continuous wavelet transform analysis for the enhancement of signal-to-noise ratio in coarse grain austenitic stainless steel. *Materials Evaluation* 2014; **72**:1519–1529.

[75] Copley DC, Howard PJ. Operational performance of a multizone billet inspection

system. *Review of Progress in Quantitative Nondestructive Evaluation*, vol. 14A. 1995; 2145–2151.

[76] Nieters EJ, Gilmore RS, Trzaskos RC, Young JD, Copley DC, Howard PJ, Keller ME, Leach WJ. A multizone technique for billet inspection. *Review of Progress in Quantitative Nondestructive Evaluation*, vol. 14. 1995; 2137–2144.

[77] Margetan FJ, Yalda I, Thompson RB, Umbach J, Suh U, Howard PJ, Copley DC, Gilmore R. Ultrasonic grain noise modeling: recent applications to engine titanium inspections. *Review of Progress in Quantitative Nondestructive Evaluation*, vol. 16. 1997; 1555–1562.

[78] Shankar PM, Karpur P, Newhouse VL, Rose JL. Split-spectrum processing: analysis of polarity threshold algorithm for improvement of signal-to-noise ratio and detectability in ultrasonic signals. *IEEE Transactions on Ultrasonics, Ferroelectrics, and Frequency Control* 1989; **36**:101–108.

[79] Konstantinidis G, Wilcox PD, Drinkwater BW. An investigation into the temperature stability of a guided wave structural health monitoring system using permanently attached sensors. *IEEE Sensors Journal* 2007; **7**:905–912.

[80] Cawley P, Cegla F, Galvagni A. Guided waves for ndt and permanently installed monitoring. *Insight - Non-Destructive Testing and Condition Monitoring* 2012; **54**:594–601.

[81] Croxford AJ, Wilcox PD, Drinkwater BW, Konstantinidis G. Strategies for guided-wave structural health monitoring. *Proceedings of the Royal Society A: Mathematical, Physical and Engineering Sciences*, vol. 463, 2007; 2961–2981.

[82] Liu Y, Liu C, Van Pamel A, Cawley P. Feasibility and reliability of grain noise suppression in monitoring of highly scattering materials. *Journal of Nondestructive Evaluation* 2017; **36**:53.

[83] Margetan FJ, Thompson RB, Yalda-Mooshabad I, Han YK. Detectability of small flaws in advanced engine alloys. *Technical Report*, Center for Nondestructive Evaluation 1993.

[84] Herrmann J, Kim JY, Jacobs LJ, Qu J, Littles JW, Savage MF. Assessment of material damage in a nickel-base superalloy using nonlinear rayleigh surface waves. *Journal of Applied Physics* 2006; **99**:124 913.

[85] Harley JB, Moura JMF. Scale transform signal processing for optimal ultrasonic temperature compensation. *IEEE Transactions on Ultrasonics, Ferroelectrics and Frequency Control* 2012; **59**:2226–2236.

[86] Clarke T. Guided wave health monitoring of complex structures. PhD Thesis, Imperial College London 2009.

[87] Clarke T, Simonetti F, Cawley P. Guided wave health monitoring of complex structures by sparse array systems: influence of temperature changes on performance. *Journal of Sound and Vibration* 2010; **329**:2306–2322.

[88] Michaels JE, Michaels TE. Detection of structural damage from the local temporal coherence of diffuse ultrasonic signals. *IEEE Transactions on Ultrasonics, Ferroelectrics, and Frequency Control* 2005; **52**:1769–1782.

[89] Clarke T, Simonetti F, Rokhlin SI, Cawley P. Evaluation of the temperature stability of a low-frequency A0 mode transducer developed for shm applications. *AIP Conference Proceedings*, vol. 975, 2008; 910–917.

[90] Ying CF, Truell R. Scattering of a plane longitudinal wave by a spherical obstacle in an isotropically elastic solid. *Journal of Applied Physics* 1956; **27**:1086–1097.

[91] Schmerr Jr LW, Song JS. *Ultrasonic Nondestructive Evaluation Systems*. Springer, 2007.

[92] Drozdz MB. Efficient finite element modelling of ultrasound waves in elastic media. PhD Thesis, Imperial College London 2008.

[93] Quey R, Dawson PR, Barbe F. Large-scale 3d random polycrystals for the finite element method: Generation, meshing and remeshing. *Computer Methods in Applied Mechanics and Engineering* 2011; **200**:1729–1745.

[94] Smith WD. The application of finite element analysis to body wave propagation problems. *Geophysical Journal of the Royal Astronomical Society* 1975; **42**:747–768.

[95] Nagy PB, Rypien DV, Adler L. Ultrasonic attenuation measurement by backscattering analysis. *Review of Progress in Quantitative Nondestructive Evaluation*, vol. 6A. 1987; 1411–1418.

[96] Nagy PB, Adler L. Scattering induced attenuation of ultrasonic backscattering. *Review of Progress in Quantitative Nondestructive Evaluation*, vol. 7B. 1988; 1263–1271.

[97] Johnston PH, Miller JG. Phase-insensitive detection for measurement of backscattered ultrasound. *IEEE Transactions on Ultrasonics, Ferroelectrics, and Frequency Control* 1986; **33**:713–721.

[98] Schmerr LW, Sedov A. Mechanical reciprocity principles and ultrasonic measurement models. *Review of Progress in Quantitative Nondestructive Evaluation*, vol. 15A, 1996; 65–71.

[99] Halmshaw R. *Non-destructive Testing*. Arnold, 1991.

[100] Schmerr LW, Sedov A. The flat-bottom hole: an ultrasonic scattering model. *Research in Nondestructive Evaluation* 1989; **1**:181–196.

[101] Miller GF, Pursey H, Bullard EC. On the partition of energy between elastic waves in a semi-infinite solid. *Proceedings of the Royal Society A: Mathematical, Physical and Engineering Sciences* 1955; **233**:55–69.